DISSERTATION

Spaceborne Rotating Torsion-Bar Antenna for Low-Frequency Gravitational-Wave Observations

BY

WATARU KOKUYAMA

Department of Physics, School of Science,
The University of Tokyo

April 2012 (Revised in June 2012)

Declaration

I hereby declare that:

— This thesis is an account of the research undertaken between April 2006 and March 2012 at the Department of Physics, School of Science, The University of Tokyo, and other cooperating research institutions.

— The research was performed under the Code of Research Ethics (established September 15, 2010) at School of Science, University of Tokyo.

— This thesis was prepared in accordance with the Guidelines for Doctoral Dissertations (established November 27, 2003) at School of Science, University of Tokyo.

— Except where acknowledged in the customary manner, the material presented in this thesis is, to the best of my knowledge, original and has not been submitted in whole or in part as a Ph.D. thesis at any other university.

Wataru Kokuyama
June 2012

Abstract

Low-frequency gravitational waves (GWs) are important targets in GW astronomy. Those in the frequency range of $10^{-4} - 1$ Hz are expected to have many interesting sources. For example, the coalescence of intermediate-mass to supermassive black holes, testing of the theories of gravity, direct measurement of the acceleration of the expansion of the Universe, and inflationary stochastic GWs from the very early Universe are considered to be targets of future GW detectors. The torsion-bar antenna (TOBA) is a novel type of detector proposed for low-frequency GW observations (Ando *et al.* PRL 2010.). The rotational motion of a test mass is sensed to detect GWs, since the rotational degree of freedom has a small spring constant.

In this thesis, a novel methodology called the frequency-upconversion technique using a rotating TOBA is proposed. With this technique, very low frequency (< 20 mHz) GWs are upconverted to approximately twice the rotational frequency, enabling them to be observed at a (relatively) high frequency, at which there are generally smaller noises. In addition, we can separate two modes of the circular polarization of GWs.

We have developed a tiny spaceborne TOBA, called $\mathrm{SWIM}_{\mu\nu}$, as an experimental module on a small satellite. Since this satellite is spinning around its principal axis, $\mathrm{SWIM}_{\mu\nu}$ acts as a rotating TOBA. The satellite was successfully launched in January 2009 and $\mathrm{SWIM}_{\mu\nu}$ has been in operation for more than one and a half years, exceeding its nominal lifetime. Detector characterization and observational runs have been conducted carefully. Although some data errors have occurred, they were successfully corrected.

Using the data obtained from $\mathrm{SWIM}_{\mu\nu}$, we performed a search for the stochastic gravitational wave backgrounds (SGWBs) by the frequency-upconversion technique. We set 95% confidence upper limits for the energy density of the SGWB, Ω_{gw}, normalized by the closure density of the Universe. The upper limits were set for the two modes called the forward mode and the reverse mode, which are superpositions of the circular polarization of two incoming waves from the zenith and the nadir. The results were 1.7×10^{31} for the forward mode and 3.1×10^{30} for the reverse mode. We believe that the achievement is a first step toward low-frequency GW observations using spaceborne GW detectors.

要旨 (Abstract in Japanese)

低周波重力波によるサイエンス

重力波とは，時空の歪みが波となって伝わる現象である。重力を表現する理論として現在広く信じられている一般相対性理論から予想されている。重力相互作用の弱さのためその直接検出は非常に難しく，2012 年現在，直接検出がなされたとの報告はない。今後数年内には，現在世界で建設がすすむ大型レーザー干渉計型検出器によって，100 ~ 1000 Hz 帯の重力波が初検出されるだろうとの期待が高まっている。

一方，低周波数帯（$10^{-4} \sim 1$ Hz 程度）にも，とても興味深い科学観測対象があると予想されている。例えば中間質量から巨大ブラックホールの連星合体を観測することによる銀河の進化過程の解明，質量比が大きな連星合体の観測による重力理論の検証，宇宙加速膨張の重力波による（電磁波によらない）計測，宇宙背景重力波の直接検出によるインフレーションの物理モデルの決定，などといった電磁波では成しえない科学的成果が考えられている。しかし，残念ながらこの周波数帯では従来の地上レーザー干渉計重力波検出器では感度が十分でない。パルサーからの電波や宇宙マイクロ波背景放射を利用した低周波重力波観測も行われているが，周波数が 10^{-6} Hz 以下と，超低周波数帯しか観測できない。よってこの周波数帯での重力波探査はあまり進んでいないというのが現状である。

そのような，地上検出器では到達できない帯域の重力波へアプローチする方法として，三つの方向性が考えられる。一つは，宇宙空間に検出器を打ち上げるという方法である。宇宙空間は基線長を非常に長くできるため重力波に対する感度が向上し、大きな検出器雑音をもつ低周波帯の観測が可能となる。それとともに，地球上には地面の振動や重力場変動などといったノイズが存在するため，それらを避けられるという極めて大きな利点もある。実際に，レーザー干渉計スペースアンテナ（LISA）計画といった宇宙空間重力波望遠鏡が提案・検討されている。二つめは，地上検出器でも低周波数重力波に感度を持つように，検出法を工夫するという考え方である。後に述べるねじれ型アンテナ（TOBA）は，そのために提案された。三つめは，重力波の周波数変換である。低周波数の重力波を，一般に検出器ノイズの少ない高周波数帯での信号に変換することができれば，観測が容易になるというわけである。この方法は今回著者らが実現した回転 TOBA によって行われた，新規の手法である。

ねじれ型アンテナ：TOBA

ねじれ型アンテナ（Torsion-Bar Antenna, TOBA）とは，低周波重力波の探査を目的とし

た新しいタイプの重力波検出器である [Ando, *et al.* Physical Review Letters, 2010]。これはレーザー干渉計型や共振型の検出器とは異なり，重力波による潮汐力が剛体の回転変動として現れる効果を利用する。そのため，小型ながら低周波に感度のある検出器が実現できると期待されている。実際に実験室でのプロトタイプ検出器も開発されており，それを用いた 0.1 Hz 帯重力波の試験的観測も行われてきた [Ishidoshiro, *et al.* Physical Review Letters, 2011]。

回転 TOBA による周波数変換とその利点

TOBA は剛体の試験質量を用いているため，検出器全体を回転させることが可能である。このような装置を回転 TOBA と呼ぶ。著者らは，この回転 TOBA による重力波の周波数変換観測法を提案した。具体的には，検出器の回転によって重力波に見かけの周波数変調がかかり，非常に低い周波数の重力波が検出器にとっては回転周波数の二倍近くの周波数の信号として見えるというものである。周波数変換時の，信号に含まれる重力波の関係を示しているのが Figure 1 である。観測周波数は，検出器の回転周波数を $\omega_{\rm rot}$ とすると，その 2 倍の周辺となる。この時，観測中心周波数（$2\omega_{\rm rot}$）より少し低い側には，Figure 1 の左側のように，円偏光が検出器の回転と揃う場合（これをフォワードモードと呼んでいる）の重力波を受ける。一方少し高い側には，Figure 1 の右側のように，逆回転の円偏光の重力波（これをリバースモードと呼ぶ）が入ってくる。重力波は通常はプラス，クロスの二つのモードで表されることが多いが，それらを基底変換したものが円偏光モードである。

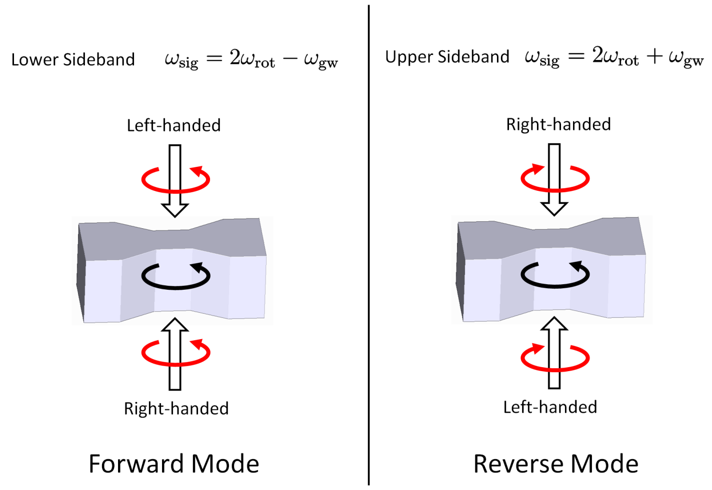

Figure 1: Separation of two polarization modes using a rotating TOBA

この回転 TOBA がもつ，通常の重力波検出器にはない新しい利点は，以下の三点である。まずひとつは，前述したように周波数変換観測が可能となることである。周波数が低くなるにしたがい，一般に検出器の電気系や外乱雑音などさまざまなノイズが急激に大きくなる。

さらに，支持系の共振周波数以下では検出器が重力波に応答しなくなる（自由質点系でなくなる）ため，重力波信号を高周波に変換できるというのは画期的な利点となる。加えて，回転周波数を変化させ観測信号帯域を自由に調整することで狭帯域ノイズを回避するという新たな手段も考えられる。

二つ目は，検出器から得られる重力波の情報が通常の検出器の二倍になるというものである。これは検出器信号のうち二つの周波数領域（フォワードモード，リバースモードに対応する）を同じ重力波の観測帯域とするためであり，一台の検出器が二台分の観測をしていることに相当する。ここで，通常の重力波検出器一台は，電磁波観測に例えると「一つの検出素子」でしかない。つまり，複数台の同時観測を行わなければ指向性を持たせることが難しく，波源の方向・強度・偏光を決められない。ところが，回転 TOBA の場合は，同じ情報量を得るために半分の台数で良くなるという利点を持つこととなる。

最後は，Figure. 1 で示されているように，直接円偏光重力波に対する感度をもっているという点である。これは，回転運動によって空間の回転対称性がやぶられているからであるともいえる。この性質を利用すれば，連星系からの重力波の円偏光を直接観測し，軌道パラメータ決定に用いることができるだろう。さらに，円偏光そのものの基礎物理的重要性も，理論的に予想されている。例えば，宇宙初期にパリティ対称性の破れが存在した場合，宇宙背景重力波の円偏光モードの一方にエネルギーが偏っていると予想されている。さらに，弦理論や量子重力理論などの効果で（現在の）重力相互作用がパリティ対称性を破っている場合，重力波の左右の円偏光に進行速度の違いがある可能性が指摘されている。

宇宙空間回転 TOBA による重力波観測

著者らは，SWIM$_{\mu\nu}$と呼ばれる小型の TOBA を製作し，宇宙航空研究開発機構（JAXA）の開発した小型人工衛星 SDS-1 に搭載した。 Figure 2 に SWIM$_{\mu\nu}$とその内部の試験質量を，Figure 3 に SDS-1 衛星の写真を示す。衛星がスピン安定状態の時に観測を行うことで，SWIM$_{\mu\nu}$が回転 TOBA を実現した。2009 年 1 月に打ち上げられた SWIM$_{\mu\nu}$は， 1 年半に及ぶ運用に成功し，動作確認，制御状態への移行，ノイズレベルの測定，キャリブレーションなどを順次行った。2010 年 6 月と 7 月には，地球を延べ 3 周回するほどの時間（延べ 360 分間）の観測運転を実施した。観測時は衛星をスピン安定（回転の周波数は 46.5 mHz）させ，その回転軸は天の川銀河中心方向に指向させた。その際，機器から得た実験データが一部破損するというトラブルが発生したが，データ転送を工夫し修復措置を施すことで解決した。

観測データの統計的解析によって，宇宙背景重力波の臨界エネルギー密度に対する比（$\Omega_{\rm gw}$）の，フォワード・リバース各モードについての上限値を算出した。解析にあたっては，頻度主義的上限値とベイズ的上限値の二種類の評価法を用いた。まず，統計誤差のみを考慮した 95 %有意水準上限値（観測周波数 18 mHz, 帯域幅 4.5 mHz）を求めた。さらにこれを踏まえ，検出器の系統誤差が 200 %であるとした保守的上限値を算出した。良好な結果を得た頻度主義的手法を選択したところ，最終的な結果を $\Omega_{\rm gw}^{\rm FW} < 1.7 \times 10^{31}$ （フォワードモード），

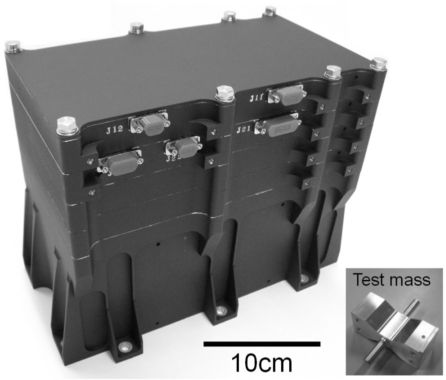

Figure 2: SWIM$_{\mu\nu}$ and the test mass

Figure 3: SDS-1 satellite

$\Omega_{\rm gw}^{\rm RE} < 3.1 \times 10^{30}$（リバースモード）と得た。SWIM$_{\mu\nu}$は小型軽量な実証機であるため，他の観測法と比較すると感度が良いわけではない。しかし，この結果は円偏光モードについての背景重力波の上限値を定めた初めての例である。ここで，二つのモードに上限値の違いが生じているが，これはモードごとに検出器信号周波数が異なりノイズレベルに差があるからであって，違う振幅の重力波を検出しているわけではないということに留意する必要がある。

意義と今後の展開

宇宙空間における回転 TOBA を実現したことで，先述した低周波重力波観測へ向けた 3 つのアプローチ（宇宙空間検出器，TOBA，周波数変換）をいずれも実施したといえる。また，技術的な側面からも，SWIM$_{\mu\nu}$によって単体として初めての軌道上重力波検出器を製作・運用することができたと同時に，リソースの少ない小型衛星を用いた成果をあげられたという重要性がある。将来の展開として，全長 4m 程度の宇宙空間回転 TOBA（H-IIA ロケットのフェアリングに収まるサイズである）でノイズを十分に低減したものが実現すれば，$10^4 \sim 10^7$ 太陽質量のブラックホール連星合体の観測などの科学的成果を得られると考えられる。このように，回転 TOBA が低周波重力波天文学の重要な手段の一つとなる可能性もある。今後 SWIM$_{\mu\nu}$の成果が，現在は困難である低周波重力波検出の最初の試みとして，発展していくことが期待される。

要約

「回転式ねじれ型アンテナ」という低周波重力波観測のための新しい手法を提案した。宇宙に小型装置を打ち上げ，その観測手法を適用した。これは，現在の検出器では困難な低周波重力波検出の試みの第一歩となったといえる。

Table of Contents

List of Figures

List of Tables

Preface

To meet the requirements of the Guidelines for Doctoral Dissertations at School of Science, the University of Tokyo, the author here clarifies his own contribution to the research presented in this thesis.

In Chapter 1, an introduction to our research is presented.

In Chapter 2, general, historical and well-known issues in the field of gravitational wave (GW) physics are reviewed. There are no results of original scientific research by the author.

In Chapter 3, the principles and characterization of the torsion-bar antenna (TOBA) are described. The TOBA is a novel type of GW detector proposed by the co-researchers of the author. The primary idea of the rotating TOBA was first presented in one of their papers, in which the current author was named as a coauthor. In this thesis, the author analyzes the characteristics of the rotating TOBA in detail. Specifically, the separation of polarization using a frequency-upconversion technique with the rotating TOBA is first proposed by the author.

In Chapter 4, a spaceborne torsion-bar antenna named SWIM$_{\mu\nu}$ is presented. The 22 coauthors of the publication on SWIM$_{\mu\nu}$ worked cooperatively in the project to develop SWIM$_{\mu\nu}$. The author also participated in the development process and was involved in its fabrication and functional tests. In particular, the author wrote all of the on-board software used to control the detector. However, the author did not contribute to the mission design or the initial detector design processes.

In Chapter 5, on-orbit experiments carried out on SWIM$_{\mu\nu}$ are presented. The operation of the satellite was conducted in cooperation with the Space Technology Demonstration Research Center of Japan Aerospace Exploration Agency. The author played a central role in the on-board detector operations such as command planning, detector monitoring and preliminary data analysis. In addition, the noise analysis described in this thesis is original research carried out by the author.

In Chapter 6, the recovery of data obtained from the detector in space is explained. The author discovered a flaw of the data. The author also proposed the recovery methods described in this chapter and conducted the recovery processes.

In Chapter 7, the data are analyzed to search for the stochastic gravitational wave background (SGWB). This data analysis is original work of the author. The results are original from the viewpoint of circular polarization modes directed to the Galactic center.

In Chapter 8 and 9, we discuss our experiments, summarize our research and gave a conclusion. These chapters are mainly the work of the author with the help and advice of co-researchers.

Glossary

Acronym	Definition
A/D	Analog-to-Digital
ADC	Analog-to-Digital Converter
BBN	Big Bang Nucreosysthesis
CCU	Central Control Unit
CMB	Cosmic Microwave Background
serial COM	Serial communication link between ECU and SpaceCube2
CRC	Cyclic Redundancy Check
D/A	Digital-to-Analog
DAC	Digital-to-Analog Converter
DAQ	Data Acquisition
DC	Direct Current
DECIGO	Deci-herz Interferometer Gravitational-wave Observatory
DoF	Degree of Freedom
DPF	DECIGO Pathfinder
ECU	Extend Control Unit
EM	Environmental Monitoring
EMRI	Extreme Mass Ratio Inspiral
EPTA	The European Pulsar Timing Array
ESA	The European Space Agency
ET	Einstein Telescope
FET	Field Effect Transistor
FIFO	First-In First-Out
FOGA	Fiber Optical Gyro Array
FPGA	Field-Programmable Gate Array
FS	Full Scale

Acronym	Definition
GPS	Global Positioning System
GR	General Relativity
GW	Gravitational Wave
IC	Integrated Circuit
pass ID	pass Identification Number
IGRF	International Geomagnetic Reference Field
IP core	Intelectual Property core
JAXA	Japan Aerospace Exploration Agency
LED	Light Emitting Diode
LIGO	Laser Interferometer Gravitational-wave Observatory
LISA	Laser Interferometer Space Antenna
LPF	LISA Pathfinder
LSB	Least Significant Bit
MEMS	Micro Electro Mechanical Systems
MSB	Most Significant Bit
NANOgrav	The North American Pulsar Timing Array
NASA	The National Aeronautics and Space Administration
Nd magnet	Neodymium magnet
PD	Photoelectric Diode
PDF	Properbility Distribution Function
PID filter	Proportional Integral Differential filter
PS	Photoreflective Sensor
PTAT	Proportional To Absolute Temperature
RMAP	Remote Memory Access Protocol
RMS	Root Mean Square
S5 run	Science-5 run
SAA	South Atrantic Anomary
SDRAM	Synchronous Dynamic Random Access Memory
SDS-1	Small Demonstration Satellite-1
SGWB	Stochastic Gravitational Wave Background
SMBH	Supermassive Black Hole
SQL	Standard Quantum Limit

Acronym	Definition
SRAM	Static Random Access Memory
TAM	Torsion-bar Antenna Module
TLE	Two Line Element
TOBA	Torsion-Bar Antenna
TRL	Technical Readiness Level
TX/RX	Transmitter/Receiver
UGF	Unity Gain Frequency
UTC	Coordinated Universal Time
VLBI	Very-Long Baseline Interferometry
WMAP	Wilkinson Microwave Anisotropy Probe

Chapter 1

Introduction

General Relativity and Gravitational Waves

General relativity (GR) [1], which is believed to be the theory of gravity, is one of the most exciting topics in modern physics. It is considered to be the key to revealing the remaining big questions in cosmology and particle physics such as those related to the accelerating Universe. By comparing the expansion rate of the Universe and its mass density, "dark energy", which is unseen energy of the vacuum called the cosmological constant, was found to be present in our Universe. Although many researchers are attempting to discover the origin of dark energy, no satisfactory explanations have been proposed. Another remaining problem is to develop a unified theory of the four interactions in nature: electromagnetic, strong, weak and gravitational forces. The theory of particle physics is expected to lead to a unified theory, i.e., one that explains all four forces at the same time with the minimum number of hypotheses and parameters. Many theoretical physicists believe that the most promising theory for such an explanation is superstring theory. Since the effects of this theory will only be apparent at very high energies, the validity of the theory cannot yet be experimentally proved.

Gravitational waves (GWs) are the phenomenon of a distortion of spacetime propagating as a wave at the speed of light [2]. Their existence was predicted by Einstein in 1916, about the same time that he discovered GR, by applying a linear field approximation to the fundamental equation of his theory, i.e., Einstein's equation, GWs were derived as propagating waves of spacetime. However, at that time it was thought to be impossible to detect GWs directly since the gravitational coupling constant is extremely small, and thus, GWs were considered to be too weak to detect. In the latter half of the twentieth century, it became expected that GWs could potentially be used as probes of very high density or dynamic phenomena such as stellar core collapse, binary mergers and the very early Universe [3, 4].

Efforts to Observe GWs

Considerable effort has been made to detect GWs over several decades. The first realistic detector was a resonant-type detector, which monitors the resonant vibration of an elastic body such as a metallic bar. An epoch-making "report of GW detection" was Weber's bar experiment in 1969 [5]. His group made the coincidence experiment of two signals of 1000-km-distant bar antennas and reported the detection of GWs. However, when it became known that the energy radiated from the source was much larger than the theoretical estimation, the research community agreed that Weber's detection was invalid. Despite this, scientists began to consider the detection of GWs seriously.

With the unexpectedly rapid advances in optical and electronic technologies, laser interferometers have become the most promising candidates for GW detectors. Compared with resonant-type detectors, they have a wider frequency band. In other words, they can measure the waveform of a GW, which is an important point in realizing astronomy based on GW observations. Recent advances in technology have resulted in the sensitivity of laser interferometers reaching a level close to that necessary to detect GWs with a sufficient event rate to carry out astronomical observations (typically several events per year). Some large-scale detectors such as the US-led Laser Interferometer Gravitational-Wave Observatory (LIGO), the joint Italy-French project Virgo, and KAGRA (formally named the Large-Scale Cryogenic Gravitational-Wave Telescope, LCGT) are expected to begin observations in the next several years. By using pulsar observations, the event rate of GWs for the Advanced LIGO-Virgo network is predicted to be 40 events per year, with range between 0.4 and 400 events with a 95% confidence level [6]. Thus, we are seeing the dawn of GW astronomy.

Low-frequency GW Observations

Similarly to electromagnetic waves, the phenomena that can be investigated through GW observations vary with the GW frequency. Here we define the low-frequency range as 10^{-4} Hz $< f <$ 1 Hz, which is used in Schutz's review [7] on scientific outcomes of the Laser Interferometer Space Antenna (LISA).

In the low-frequency region, it is predicted that the following phenomena can be investigated. Observation of the coalescence of binary intermediate-mass to supermassive black holes (SMBHs), which usually exist in ordinary galaxies, will provide information on their evolutionary process. It is considered that GWs from extreme mass ratio inspirals (EMRIs) can be used as a probe to determine the theory of gravitation. In other words, if

GR is violated, the signal from EMRIs will differ from that calculated by GR. The most sensational expectation of low-frequency GW science is the detection of the stochastic gravitational wave background (SGWB). In particular, in the frequency range of 0.1 - 1 Hz, it is considered that relic GWs from the inflationary phase of the Universe can be detected directly. If such observations are possible, the scalar-field potential causing the inflation can be determined directly, which will have significant impact in both particle physics and cosmology.

Spaceborne GW Detectors

Various spaceborne GW detector missions have been proposed. The most well-known project is LISA, which is a joint US-Europe space mission. Laser interferometers will be formed among three spacecraft at a distance of 5 million km from each other. As its precursor mission, the LISA Pathfinder (LPF) satellite has been developed and will be launched in 2012. Some essential technologies for LISA such as onboard interferometry and test mass charging control will be tested on LPF. Note that LISA has recently been redefined as a new Europe-led project called eLISA [8].

Another space-based GW detector is the Deci-Hertz Gravitational-Wave Observatory (DECIGO) proposed by Japanese researchers [9]. Other space programs such as ASTROD [10] and AGIS [11] are also being considered.

Spaceborne Rotating Torsion-Bar Antenna: SWIM$_{\mu\nu}$

To achieve GW astronomy from space, we should start with small, cheap and fast programs. We thus developed a spaceborne torsion-bar antenna (TOBA) called SWIM$_{\mu\nu}$ for use aboard a small satellite. SWIM$_{\mu\nu}$ can be used to demonstrate various core technologies such as the control system and data processing framework for future space missions.

We proposed the rotating TOBA as one of the operation modes of SWIM$_{\mu\nu}$. Since the satellite in which SWIM$_{\mu\nu}$ is installed rotates around its principal axis, it becomes a rotating TOBA. Thus, it enables the frequency-upconversion technique to be applied to low-frequency GWs to obtain a signal with sufficiently high frequency for detection. Our first aim to achieve low-frequency GW observation from space using this new detector technology and to perform satellite demonstrations using SWIM$_{\mu\nu}$.

Structure of This Thesis

This thesis is constructed as follows. Chapter 1 is an introduction. In Chapter 2, we derive and explain the characteristics of GWs. In addition, various past and present GW detectors are reviewed. In Chapter 3, the detection principles of the TOBA and the rotating TOBA are shown. We discuss the advantages of the detection method and its expected sensitivity. In Chapter 4, the design and structure of SWIM$_{\mu\nu}$, which is a compact spaceborne TOBA, are explained. In Chapter 5, on-orbit experiments are presented in detail. In Chapter 6, the data correction process is described in detail. This is important since the raw data were too dirty to be used in observation analysis owing to errors. Chapter 7 describes the analysis carried out to search for stochastic GW backgrounds at a frequency of 18 mHz, which has never been a target frequency of past GW detectors. We discuss future prospects for the spaceborne rotating TOBA in Chapter 8 and we summarize the thesis in Chapter 9.

Chapter 2

Gravitational Waves

In this chapter, we briefly introduce the theory of GWs. First, we derive GWs as a solution of a linear approximation of the wave equation. Some characteristics of GWs are examined. Second, various attempts to observe GWs, such as through the use of a laser interferometer, resonant-bar antenna and TOBA, are reviewed. At the end of this chapter, expected celestial GW sources are given.

2.1 General Relativity and Gravitational Waves

2.1.1 General Relativity and Einstein's Equation

In Einstein's general theory of relativity [1], the Universe is treated as four-dimensional spacetime. The geometry of the spacetime is expressed by the metric $g_{\mu\nu}$, that is, GR is a kind of metric theory. The fundamental equation (equation of motion) in GR is the Einstein equation

$$R_{\mu\nu} - \frac{1}{2}g_{\mu\nu}R = \frac{8\pi G}{c^4}T_{\mu\nu} \ , \tag{2.1}$$

where $R_{\mu\nu}$ and R are the Ricci tensor and the scalar curvature, respectively. The Ricci tensor is obtained by contracting the Riemann tensor $R^{\lambda}{}_{\mu\rho\nu}$, and the scalar curvature is derived from the Ricci tensor:

$$R_{\mu\nu} = R^{\lambda}{}_{\mu\lambda\nu} \ , \tag{2.2}$$

$$R = R^{\lambda}{}_{\lambda} \ . \tag{2.3}$$

$T_{\mu\nu}$ denotes the energy-momentum tensor, which expresses the amount of matter and energy in the spacetime. In other words, the Einstein equation (2.1) implies that the curvature of spacetime should be determined by matter and energy in the field.

2.1.2 Weak-Field Approximation and Gravitational Waves

Now we consider the weak-field approximation. Suppose the metric $g_{\mu\nu}$ can be expressed as the first-order approximation:

$$g_{\mu\nu} = \eta_{\mu\nu} + h_{\mu\nu} \ , \tag{2.4}$$

where $\eta_{\mu\nu}$ is the Minkowski (flat) metric,

$$\eta_{\mu\nu} = \begin{pmatrix} -1 & 0 & 0 & 0 \\ 0 & 1 & 0 & 0 \\ 0 & 0 & 1 & 0 \\ 0 & 0 & 0 & 1 \end{pmatrix} \ , \tag{2.5}$$

and $h_{\mu\nu}$ is its small perturbation, $|h_{\mu\nu}| \ll 1$. This assumption means that we consider a weak gravitational field with low energy density. Using the expansion (2.4) and the Einstein equation (2.1), we derive the following equation for $h_{\mu\nu}$, neglecting the $O(h^2)$ terms:

$$\frac{\partial^2 h_{\mu\nu}}{\partial x^a \partial x_a} = \Box h_{\mu\nu} = -\frac{16\pi G}{c^4} T_{\mu\nu} \ , \tag{2.6}$$

using the d'Alembertian $\Box$. Since the Einstein equation has 20 degrees of freedom, we can choose the Lorenz gauge,

$$\frac{\partial \bar{h}^{\mu}{}_{\nu}}{\partial x^{\mu}} = 0 \ . \tag{2.7}$$

Here we translate $h_{\mu\nu}$ into

$$\bar{h}_{\mu\nu} = h_{\mu\nu} - \frac{1}{2}\eta_{\mu\nu} h \ . \tag{2.8}$$

In the case of a vacuum, that is, $T_{\mu\nu} = 0$, the wave equation

$$\Box \bar{h}^{\mu}{}_{\nu} = 0 \tag{2.9}$$

is obtained. Thus, the perturbation of the metric can propagate as a wave. This is a GW.

2.1.3 Characteristics of Gravitational Waves

Here we briefly explain the characteristics of GWs. From the wave equation (2.9), we have

$$\bar{h}^{\mu}{}_{\nu} = A_{\mu\nu} e^{ik_\alpha x^\alpha} \ , \tag{2.10}$$

where the propagating direction of the GW is denoted as k_α. From the Lorenz gauge (2.7), we derive the transverse wave condition

$$A^{\mu\alpha}k_\alpha = 0 \ , \tag{2.11}$$

and show that GWs propagate at the speed of light:

$$k_\alpha k^\alpha = 0 \ . \tag{2.12}$$

Here we assume the transverse-traceless gauge, which is

$$A^\alpha{}_\alpha = 0, \quad A_{\mu\nu}\delta^\nu{}_0 = 0 \ , \tag{2.13}$$

to simplify the expression for the GW amplitude $A_{\mu\nu}$. Considering plane GWs travel along the Z-axis, $k_\alpha = (0,0,0,k)$, then $A_{\mu\nu}$ can be decomposed using two parameters h_+ and $h_\times$:

$$A_{\mu\nu} = \begin{pmatrix} 0 & 0 & 0 & 0 \\ 0 & h_+ & h_\times & 0 \\ 0 & h_\times & -h_+ & 0 \\ 0 & 0 & 0 & 0 \end{pmatrix} \ . \tag{2.14}$$

Thus, GWs have two degrees of freedom, namely, polarizations. We call h_+ the plus mode and $h_\times$ the cross mode.

Effect on Test Masses

Next we consider how a GW affects test masses. Here we assume the transverse-traceless gauge (2.13), so that $A_{0\nu}$ and $A_{\mu 0}$ are zero. That means that no acceleration exists in the local frame of the test mass. This is why GWs cannot be detected by only sensing motion of the individual test masses. Thus, it is natural that we have to construct large-scale detectors or distant arrays of detectors to achieve satisfactory sensitivity to GWs.

We examine the proper distance δl between two test masses. Considering one test mass to be at the origin and the other to be located at $(0,d,0,0)$ in four-dimensional coordinates as an example, then the proper distance between them is

$$l + \delta l_{\mathrm{gw}} = \int \left|\mathrm{d}s^2\right|^{1/2} = \int |g_{\mu\nu}\mathrm{d}x^\mu \mathrm{d}x^\nu|^{1/2} \tag{2.15}$$

$$= \int_0^d |g_{11}|^{1/2}\,\mathrm{d}x \sim \left(1 + \frac{1}{2}h_+\right) l \ . \tag{2.16}$$

Therefore, δl for two test masses aligned in the x-direction is proportional to the amplitude of the plus mode of the GW, h_+:

$$\frac{\delta l_{\rm gw}}{l} \simeq \frac{1}{2} h_+ \tag{2.17}$$

This is the principle of detection for laser-interferometric GW detectors.

2.1.4 Generation of Gravitational Waves

Here we briefly review the generation of GWs. A good textbook on the theory of relativity written by Mio [12] is used as a reference.

Quadrupole Formula

To discuss GWs emitted from a dynamic system, the wave equation, (2.9), is solved as:

$$\bar{h}_{ij} = \frac{4G}{c^4} \int \frac{T_{ij}(t - r/c, r')}{r} dV' \ . \tag{2.18}$$

Then, by extracting the transverse-traceless component of this equation and by integrating on a sphere of radius r, the total power emitted from the system W is expressed as:

$$W = \frac{G}{5c^5} \langle \dddot{Q}_{ij} \dddot{Q}^{ij} \rangle \ , \tag{2.19}$$

where Q is the (traceless) quadrupole moment of the mass distribution,

$$Q_{ij} = \int \left(x'_i x'_j - \frac{\delta_{ij} r'^2}{3} \right) \rho \ {\rm d}V' \ . \tag{2.20}$$

Equation (2.19) is called the quadrupole formula of generation of GWs.

Emission of GWs from Rotating Mass

Consider a mass like a dumbbell rotating around its center. Suppose two point-like masses with the mass m are connected mechanically, or bound gravitationally, to each other. Their distance is $2l$. Rotating angular frequency is assumed to be Ω. Then, by applying the quadrupole formula, the total power of GWs generated from this system will be

$$W = \frac{128G}{5c^5} \Omega^6 m^2 l^4 \ . \tag{2.21}$$

By substituting the typical values in laboratory experiment, we can estimate the power of GWs that can generate artificially

$$W_{\rm Lab} = 4.3 \times 10^{-29} \ {\rm W} \ , \tag{2.22}$$

where Ω, m and l are assumed to be $2\pi \times 100$ rad/s, 1000 kg and 1 m, respectively.

In contrast, when the neutron-star binary is considered, the energy emitted from the binary is estimated as:

$$W_{\text{NS-NS}} = \frac{2G^2M^5}{5l^5} \ . \tag{2.23}$$

Here the relation of the gravitationally-bound two-body system, $l\Omega = GM/4l^2$, is used.

Applying the typical parameters of the binary neutron stars that has been discovered in the Milky Way galaxy, i.e., $M = 1.4M_\odot \simeq 3 \times 10^{30}$ kg and $l = 1000$ km,

$$W_{\text{NS-NS}} = 6 \times 10^{38} \text{ W} \ . \tag{2.24}$$

If the binary is 10 kpc away from the Earth, the energy flux of the GW is approximately

$$L_{\text{NS-NS}} = 5 \times 10^{-4} \text{ W/m}^2 \ . \tag{2.25}$$

By comparing (2.22) and (2.25), it is apparent that celestial GWs are much stronger than that from laboratory experiments.

2.2 Gravitational Wave Observations

More than 40 years have passed since the first attempt by Weber [5] to directly observe GWs. Various kinds of observational techniques have since been developed. Here we briefly introduce their status and recent progress.

2.2.1 Laser-Interferometric Detector

The most promising and successful type of GW detector is the laser interferometer. In particular, the LIGO [13, 14] project in the US and the Italy-France project Virgo have achieved their design sensitivity. Some results for GW search have been published. For example, a prompt search for the electromagnetic counterparts of GW emissions has been reported [15].

Toward the first detection of GWs, several second-generation GW detectors are under construction. Advanced LIGO is an upgrade of the LIGO project, and Advanced Virgo is an upgrade of the Virgo. KAGRA, formerly named LCGT, is a Japanese large-scale laser interferometer, which will start its observation in 2018. There is also a third-generation GW detector project underway named the Einstein Telescope (ET) [16]. The results expected from the GW detectors are discussed in [17].

The planned spaceborne GW detectors, such as LISA, DECIGO and ASTROD are also laser interferometers. This is because a laser can propagate over a long distance and ultra precise measurement can be realized using stabilized lasers.

2.2.2 Resonant-Type Detector

The “first detection” reported by Weber [18] with a resonant antenna developed at the University of Maryland in 1969. Recent resonant-bar detector projects have been ALLEGRO at Louisiana State University, EXPLORER at CERN and NAUTILUS at INFN in Italy. At the same time, a torsion-type resonant antenna was proposed [19] by Hirakawa’s group at the University of Tokyo. They also developed an antenna operating at 145 Hz [20], and conducted a search for continuous GWs from the Crab pulsar at 60.2 Hz [21].

2.2.3 Pulsar Timing

Pulsar timing is the method of using pulsars as precise reference clocks to detect the distortion of spacetime induced by GWs. The method is reviewed in [22] and a detailed analysis is given in [23]. In brief, the arrival times of observed pulsars are compared with the predicted arrival times using a model involving of the spin, orbit and other astrometric parameters of the pulsar system. Since the fluctuation of the pulsar timing is observed, the lower bound of the detection frequency band, $f > 10^{-9}$ Hz, is constrained by the observation time. The upper bound, $\sim 10^{-7}$ Hz, is limited by the observational sampling period since the measurements only have satisfactory precision after observation for a few months. The current constraint on the sensitivity originates from the uncertainty of the time of arrival of the signals.

There are three major future projects planned. One is the Parkes pulsar timing array project [24] in Australia. The North American pulsar timing array (NANOGrav) [25] at Arecibo and Green Bank Telescope in the US is another project. The European pulsar timing array (EPTA) [26] is a joint European project. These projects are starting to collaborate with each other to form an international pulsar timing array [27]. Some applications based on the use of advanced pulsar timing arrays, such as probe to polarization properties of millisecond pulsars, the solar-system ephemeris and the development of a global time standard, are being considered [28].

2.3 Celestial Source of Gravitational Waves

As shown above, the artificial generation of GWs with detectable amplitude is not promising. However, astrophysical objects such as neutron stars and black holes have a large mass, and thus generate strong GWs. Here we briefly review the celestial GW sources being considered for current and future GW detectors. The parameters used to characterize GWs from celestial sources are the waveform, frequency and amplitude. The relations between sources and waveforms are summarized in Table 2.1.

Classification with Waveform of GW

In Table 2.1, the following classifications of GW waveform are used. Continuous GW is the wave, of which frequency remains constant in observation period. Chirp signal is the wave that the bandwidth of the signal is narrow and the frequency of the signal slowly increases. In case of binary coalescence, the amplitude of the signal also increases gradually and we call such a type of signal a chirp signal. Ringdown is an oscillating signal with dumping. Note that the word ringdown is also used for dumped oscillation of the vibration mode itself. Burst signal is not sinusoidal, and its duration is shorter than the characteristic frequency which is a central frequency of its spectra.

Various Celestial Sources of GWs

Possible sources shown in Table 2.1 are the follows. Stable binary system produces, as shown in Section 2.1.4, monochromatic GWs. GWs propagating in the plane of the binary system are full-polarized to either mode (depending on the coordinates of the observer). In contrast, superposition of such GWs from many binary systems can be stochastic waves, since the phase, and directions are randomly distributed. For example, white dwarf binaries in the Milky Way galaxy generate stochastic GWs in the frequency of $10^{-4} - 10^{-1}$ Hz [29]. This stochastic waves are called a confusion noise when we consider low-frequency GW detectors such as LISA, DECIGO and BBO, since the waves may be a foreground noise for the GWs from the inflation era of the Universe. Another kind of confusion noises for DECIGO and BBO is superposition of indistinguishable GWs from neutron star binaries. The identification of the signal from individual binary and subtraction from detector signals are being considered [30, 31].

GWs from pulsars have continuous waveform and are the important targets of resonant type GW detectors. The frequency of the waves are typically order of 100Hz, corresponding twice the rotation frequency of the pulsars. Since the asymmetry of the mass distribution of the pulsar generate GWs, thus the GWs can be a probe to the state of neutron stars.

Binary merger, especially neutron star-neutron star pair is a main target of current terrestrial GW detectors. Its frequency range is $10^2 - 10^4$ Hz. It is predicted that the binary merger produces chirp GWs before the collision. At the time the two stars collide with each other, burst wave is produced. When a black hole is created after the collision, the black hole is expected to radiate its energy of quasi-normal vibration mode as a ringdown GWs.

Stellar core collapse in a supernova is also a possible target for ground-based GW detectors. In contrast to binary merger and pulsar, GW from supernovae is expected to be a burst wave. Although the waveform is being calculated by using numerical relativity, the expected amplitude strongly depends on the physical models for the supernovae.

Magnetar is a neutron star that has very strong magnetic field and that emit X-rays and gamma rays. GWs from magnetars are also considered to be a target of advanced ground-based GW detectors [32]. In addition, neutrino-driven gamma ray bursts are also consider to emit GWs, and random superposition of the GWs can be an origin of SGWB [33].

GWs radiated from the supernovae in the era of the first stars in the Universe, i.e., at time time of the redshift $z \sim O(1)$, can be a possible source of future low-frequency GW detectors [34]. The origin of such type of supernovae is called POP-III Stars. The mass of the stars are very large; it may exceed several ten times of the solar-mass. The spectrum is expected to be wide, since the radiated GWs from the supernovae is like a pulse. A random superposition of such GWs is considered to be a serious foreground of the inflationary SGWB.

When primordial density fluctuations have a large amplitude, primordial black holes were created and they can be the origins of the intermediate-mass black holes. In this case, stochastic GWs produced by (second-order effects of) the density fluctuation is observable by low-frequency GW detectors [35, 36]. The predicted spectrum of stochastic GWs is narrow, i.e., the energy density in the peak frequency is much larger than that in the other frequency. Such narrow band stochastic GW should be a target of rotating TOBA proposed in this thesis.

Besides, GWs from cosmic string [37], electroweak phase transition of the vacuum [38], preheating at the end of inflation [39] and other cosmological origins are predicted.

Table 2.1: Celestial GWs classified with source and waveform. A circle in a box means that GWs with the corresponding waveform and sources are expected to exist.

	Continuous	Chirp	Ringdown	Burst	Stochastic
Stable binary system	○				
Pulsar rotation	○				
Binary merger		○	○	○	
Stellar core collapse				○	
Many binary systems					○
Supernova (POP-III Stars)					○
Cosmic string					○
Vacuum phase transition					○
Inflation					○

Chapter 3

Torsion-Bar Antenna

A TOBA is a novel type of GW detector for low-frequency GW observations that has been proposed recently [40]. In this chapter, the TOBA and the rotating TOBA are described. First, we explain the detection principles of TOBA. The differences between the TOBA and conventional detectors such as laser interferometers and resonant detectors are then presented. Various noise sources are also considered and roughly estimated for a TOBA. Second, the frequency-upconversion technique using the rotating TOBA is presented. We show its advantages over conventional detectors, particularly from the viewpoint of spaceborne detectors.

3.1 Principles of Detection

A TOBA consists of a test mass which receive GWs and readout system that sense the rotational motion of the test mass. The effect of GWs on a TOBA is to apply a rotational force (torque) to a rigid body. In this section, the detection principles of a TOBA and rotating TOBA are described.

3.1.1 GW-induced Forces on Elastic Body

Here we examine how incoming GWs affect a TOBA. To acquire a generalized equation of motion for a test mass, we study the effect of GW-induced forces on elastic bodies, which are expressed using the vibrational mode eigenfunction as described in [41].

Consider a certain eigenmode of an elastic body. The displacement at a certain point $\boldsymbol{x}$

is expressed using the mode function $\boldsymbol{w}(\boldsymbol{x})$:

$$\boldsymbol{u}(t,\boldsymbol{x}) = \xi_{\boldsymbol{w}}(t)\boldsymbol{w}(\boldsymbol{x}) \ . \tag{3.1}$$

Here, the scalar value $\xi(t)$ is the generalized amplitude of the mode. The generalized force induced by GWs can be expressed as follows [41]:

$$f_{\mathrm{gw}}(t) = \frac{1}{4}\ddot{h}_{ij}(t) \cdot q^{ij}_{\boldsymbol{w}} \ , \tag{3.2}$$

where $q^{ij}_{\boldsymbol{w}}$ is called the dynamic quadrupole moment tensor for this eigenmode $\boldsymbol{w}$, defined as

$$q^{ij}_{\boldsymbol{w}} \equiv \int \rho \left(x^i w^j + w^i x^j - \frac{2}{3}\delta^{ij} x_k w^k \right) \mathrm{d}V \ . \tag{3.3}$$

Equation (3.2) is derived from a more fundamental equation of motion in Hirakawa's book [41].

Thus, the equation of motion for the eigenmode is given in terms of the Q value and the resonant frequency ω_0 as

$$\mu \left(\ddot{\xi} + \frac{\omega_0}{Q}\dot{\xi} + \omega_0^2 \xi \right) = f_{\mathrm{gw}}(t) \ . \tag{3.4}$$

3.1.2 Response Function to GWs

Assume that the test mass in a TOBA satisfies the following assumptions:

- The test mass is aligned along the X-axis.
- The shape of the test mass is symmetric. In fact, the density distribution $\rho(\boldsymbol{x})$ is symmetric in all three axes: $\rho(x,y,z) = \rho(-x,y,z) = \rho(x,-y,z) = \rho(x,y-z)$.

Here the mode function $\boldsymbol{w}(\boldsymbol{x})$ of the rotation is given as

$$\boldsymbol{w}(\boldsymbol{x}) = \frac{1}{\sqrt{2}} \begin{pmatrix} -y \\ x \\ 0 \end{pmatrix} \ . \tag{3.5}$$

Then, using equation (3.3), we find that the diagonal elements vanish:

$$q^{11} = \int \rho(-\sqrt{2}xy)\mathrm{d}V = 0 \tag{3.6}$$

$$q^{22} = \int \rho(\sqrt{2}xy)\mathrm{d}V = 0 \ , \tag{3.7}$$

whereas the non diagonal elements do not vanish owing to the rectangular shape of the test mass:

$$q^{12} = q^{21} = \int \frac{1}{\sqrt{2}} \rho(x^2 - y^2) \mathrm{d}V \equiv q_\times \neq 0 \ . \tag{3.8}$$

We call $q_\times$ the cross component here. Assuming that plane GWs arrive from the +Z-direction,

$$h_{ij}(t) = \begin{pmatrix} h_+(t) & h_\times(t) & 0 \\ h_\times(t) & -h_+(t) & 0 \\ 0 & 0 & 0 \end{pmatrix} \ . \tag{3.9}$$

From equation (3.2) we find that the GW-induced force is

$$f_{\mathrm{gw}}(t) = \frac{1}{2} q_\times \ddot{h}_\times(t) \ . \tag{3.10}$$

Therefore, the equation of motion for the rotational angle displacement $\theta(t)$ is

$$\mu \left(\ddot{\theta}(t) + \frac{\omega_0}{Q} \dot{\theta}(t) + \omega_0^2 \theta(t) \right) = \frac{1}{2} q_\times \ddot{h}_\times(t) \ . \tag{3.11}$$

Here μ is the reduced mass corresponding to this rotational mode:

$$\mu \equiv \int \rho(\boldsymbol{x}) \left| \boldsymbol{w}(\boldsymbol{x}) \right|^2 \mathrm{d}V \tag{3.12}$$

$$= \int \rho(\boldsymbol{x})(x^2 + y^2) \mathrm{d}V \ , \tag{3.13}$$

where $\rho(\boldsymbol{x})$ and V are the density and volume of the test mass, respectively.

Applying a Fourier transformation to the equation of motion (3.11), we obtain

$$\tilde{\theta}(\omega) = \frac{q_\times \omega^2}{2} H(\omega) \tilde{h}_\times(\omega) \ . \tag{3.14}$$

Here $H(\omega)$ is the mass transfer function,

$$H(\omega) \equiv \frac{1}{\mu \omega^2} \left(1 + \frac{i\omega_0}{Q\omega} - \frac{\omega_0^2}{\omega^2} \right)^{-1} \ . \tag{3.15}$$

Most interferometric GW detectors are operated at a frequency above the resonant frequency of the suspension to achieve high sensitivity. When the observation frequency ω is much higher than the resonant frequency of the rotational suspension system, i.e., $\omega \gg \omega_0$, $H(\omega)$ can be assumed to be $\frac{1}{\mu\omega^2}$. Thus,

$$\tilde{\theta}(\omega) = \frac{q_\times}{2\mu} \tilde{h}_\times(\omega) \ . \tag{3.16}$$

This equation means that the cross component of the incoming GWs is coupled to the dynamic quadrature of the test mass in the TOBA.

3.1.3 Differences from Conventional Detectors

Analogously, a TOBA can be regarded as a rigid-body-type detector. On the other hand, a laser-interferometric detector can be regarded as a free-mass detector, and a resonant-type detector can be regarded as two masses bound with a spring. This explanation is shown graphically in Figure 3.1. In addition, the differences among the three types of detector are shown in Table 3.1. Since a TOBA utilizes rotational sensing to detect GWs, it has high sensitivity to low-frequency GWs while employing (relatively) compact antennae. Another advantage is its wide-band sensitivity, which is crucial for extracting astronomical information from the obtained signals.

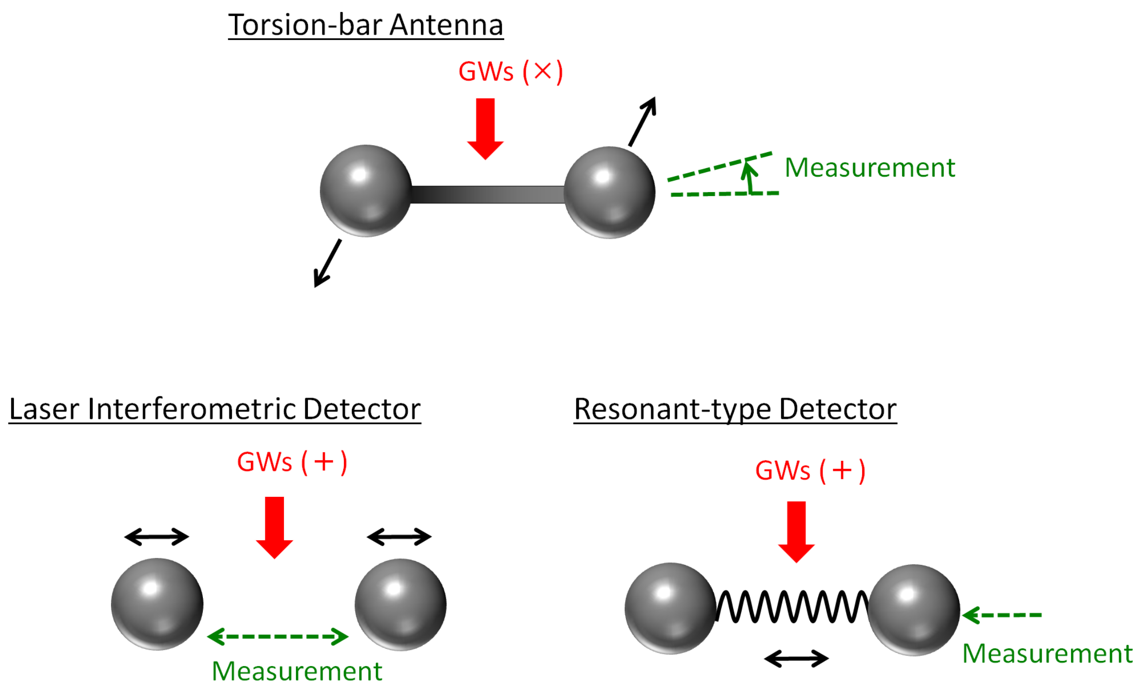

Figure 3.1: Detector response to GWs compared with that of convensional detectors. The body of the detector, the incoming GWs and the measurand are shown for each detector.

An antenna pattern function is the response function to the incoming GWs of the

Table 3.1: Characteristics of TOBA and conventional detectors.

	TOBA	Laser Interferometer	Resonant Detector
Measurand	Rotation	Parallel Motion	Vibration Mode
Baseline Length	$\sim$ O(10m)	O(km)	O(10m)
Obs. Frequency	10 mHz -	10 Hz - 10 kHz	O(100 Hz)
Obs. Bandwidth	Wide	Wide	Narrow

detector. The pattern function of a TOBA, shown in Figure 3.3, is almost the same as that of a laser interferometer. The only difference is that the pattern function to plus-mode GWs of a TOBA is the same as that to cross-mode GWs of a laser interferometer. Note that the test mass of the TOBA is assumed to be aligned to x-axis, so that the TOBA has sensitivity to cross-mode GWs.

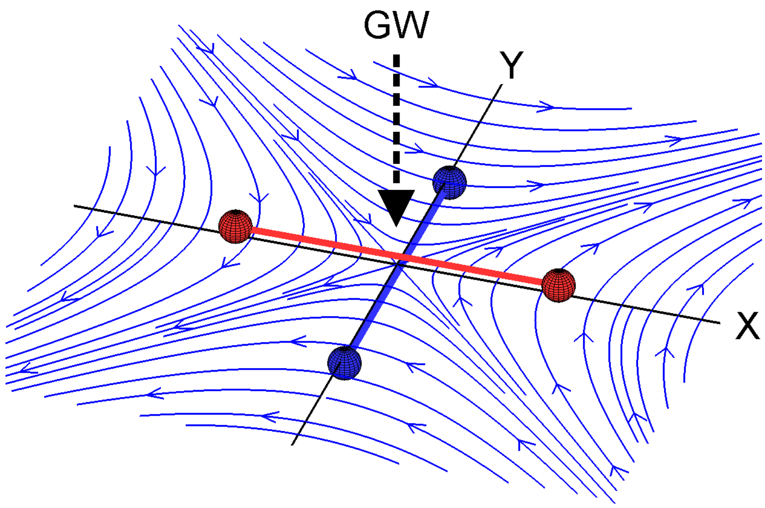

Figure 3.2: Force line to the test masses induced by Z-propagating cross-mode GWs. Two dumbells in the X-Y plane show test masses for a TOBA.

3.1.4 Noise Sources and Sensitivity of TOBA

To consider the sensitivity of a TOBA, we have to estimate various noise sources in the detector. The noise sources are divided into three categories: intrinsic noise, readout noise and external disturbances. External disturbances are a practical noise that can be reduced or attenuated by various measures. Here we estimate approximate noise level for

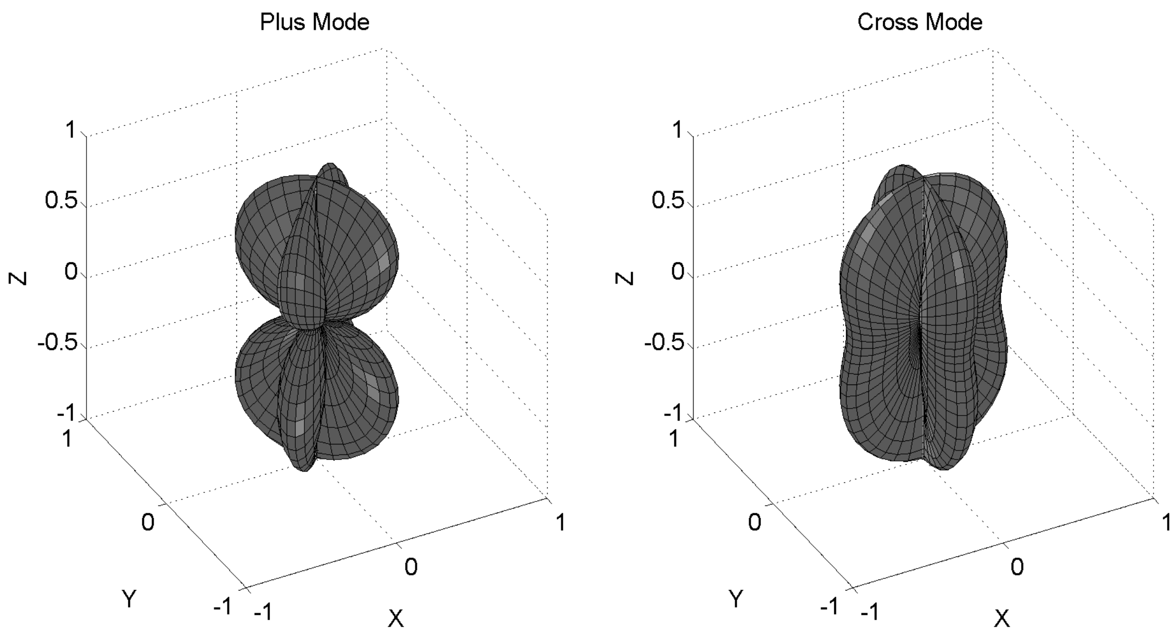

Figure 3.3: Antenna pattern function of static TOBA with one test mass. The test mass is aligned to the X-axis.

each noise source, in accordance with the estimation in [40], and estimate the sensitivity of a TOBA to GWs with realizable parameters as an example.

We show the notation of the parameters used in the analysis in Table 3.2. Here we assume a large-scale TOBA, which has a 10 m cooled aluminum torsion bar with a low-loss suspension system. This system will be discussed later in Chapter 8, in which the future prospects of the TOBA are explained.

3.1.4.1 Intrinsic Noise

Intrinsic noise is an inevitable thermal noise induced by the mechanical loss of the mass itself or the suspension system. It can be reduced in only two ways: by decreasing the mechanical loss (i.e., improving the Q factor) or cooling the system to a low temperature (typically, $T < 20$ K). In the system considered here, the two torsion bars in the TOBA are supported by a suspension system. Thus, both the bar itself and the suspension system have intrinsic thermal noise.

Bar Thermal Noise

Table 3.2: Description of parameters and assumed values for large-scale TOBA.

Notation	Description
λ	Wavelength of laser
P_{in}	Input power of laser interferometer
N	Round trip number of Fabry-Perot cavity
L	Length of torsion-bar
M	Mass of torsion-bar
I	Moment of inertia of torsion-bar
γ	Loss factor of suspension system
ϕ_{mass}	Loss angle of vibration mode of torsion-bar
T	Temperature of detector

The inevitable bar thermal noise is due to the internal mechanical loss of the torsion bar in a TOBA. Concretely, the bar oscillates in accordance with its mechanical eigenmodes owing to the thermal noise. Then the induced displacements at the sensing point may generate fake signals indicating rotational motion since the bar thermal noise is mixed with the GW-induced rotation of the TOBA. According to the analysis in [40], the bar thermal noise of a cylindrical bar will generate noise with spectral density equivalent to rotational displacement of:

$$\delta\theta_{\mathrm{BarTh}} \simeq \frac{8}{L}\sqrt{\frac{\phi_{\mathrm{Bar}} k_{\mathrm{B}} T}{M\omega_{\mathrm{Bar}}^2 \omega}} \,. \tag{3.17}$$

Suspension Thermal Noise

Another intrinsic noise is generated by the loss in the suspension system. For TOBAs in space, the test mass should be suspended by a wire or magnetic bearing. In a conventional TOBA, a torsion pendulum or superconducting pinning effect is used to support the test mass, since the rotational confinement should be loose, i.e., the rotational spring constant can be small owing to its symmetric shape. The noise spectrum density of this thermal noise has been found to depend on the loss factor of the suspension system:

$$\delta\theta_{\mathrm{SusTh}} \simeq \frac{\sqrt{4\gamma k_{\mathrm{B}} T}}{I\omega^2} \,. \tag{3.18}$$

3.1.4.2 Readout Noise

Readout noise is an intrinsic noise in the readout system, which is usually a laser interferometer. Note that two types of noises, shot noise and radiation pressure noise, are fundamental noise: they are inevitable in precise measurement using optical devices such as laser interferometers. In addition to the fundamental noises, laser intensity noise and frequency noise exist.

Shot Noise

The fundamental phase uncertainty of the laser beam itself induces a position readout error in the measured system. This is called shot noise, which is the main noise source limiting the sensitivity of ground-based laser-interferometric detectors. In the case of a TOBA, we use a laser-interferometric readout for the rotational motion of the torsion bar, thus, the position uncertainty on the edge of the test mass owing to shot noise becomes a noise in GW detection. The spectral density of shot noise is estimated as

$$\delta\tilde{\theta}_{\mathrm{shot}} = \frac{1}{2LN}\sqrt{\frac{\hbar c\lambda}{\pi P_{in}}} \ . \tag{3.19}$$

Note that the spectral density is proportional to $P_{\mathrm{in}}^{-1/2}$.

Radiation Pressure Noise

The back action of the measurement causes uncertainty of the position of the system. In this case, this effect can be regarded as a noise originating from the fluctuation of the laser light pressure, therefore it is called radiation pressure noise and is given by

$$\delta\tilde{\theta}_{\mathrm{rad}} = \frac{2LN}{I\omega^2}\sqrt{\frac{\pi\hbar P_{in}}{c\lambda}} \ . \tag{3.20}$$

Here the noise spectral density is proportional to $P_{\mathrm{in}}^{1/2}$, i.e., its dependence on the laser power is inverse to that for shot noise.

Standard Quantum Limit

Shot noise and radiation pressure noise are physically conjugate noises. Thus, as long as a "normal" quantum state is used in laser interferometry, there is a limit to the displacement sensitivity. More specifically, considering the combined noise level of the two noises,

$$\sqrt{(\delta\tilde{\theta}_{\mathrm{shot}})^2 + (\delta\tilde{\theta}_{\mathrm{rad}})^2} \ , \tag{3.21}$$

using the Cauchy-Schwarz inequality, it is easily shown that the combined noise level has a minimum value when

$$\delta\tilde{\theta}_{\mathrm{shot}} = \delta\tilde{\theta}_{\mathrm{rad}} \ . \tag{3.22}$$

This is called the standard quantum limit (SQL). Here we substitute both side of equation (3.22) by equation (3.19) and (3.20), i.e.,

$$\frac{1}{2LN}\sqrt{\frac{\hbar c\lambda}{\pi P_{in}}} = \frac{2LN}{I\omega^2}\sqrt{\frac{\pi\hbar P_{in}}{c\lambda}} \ . \tag{3.23}$$

We solve this equation to derive the SQL frequency ω_{SQL} as

$$\omega_{SQL} = 2LN\sqrt{\frac{\pi P_{in}}{cI\lambda}} \ . \tag{3.24}$$

Thus the sum of the shot noise and radiation pressure noise is simplified to

$$\sqrt{\left(\delta\tilde{\theta}_{\rm shot}(\omega_{SQL})\right)^2 + \left(\delta\tilde{\theta}_{\rm rad}(\omega_{SQL})\right)^2} \quad = \quad \sqrt{\frac{2\hbar}{I\omega^2}} \ . \tag{3.25}$$

To overcome this limit, various techniques have been proposed. For example, inputting squeezed light at the output port of the interferometer is expected to reduce the shot noise, without increasing the radiation pressure noise. Note that the SQL given by equation (3.25) is equal to the Planck constant $\hbar$ divided by the energy of a quantum for the test mass at a frequency, $I\omega^2$.

Other Noises

The other sources of readout noise are the intensity noise, the frequency noise, and the beam jitter in the laser used in the interferometric displacement sensor. These are practical noises, however, and the sensitivity is limited by these noises in the most cases. Laser intensity noise usually couples with the optical modulation and is mixed with the displacement-induced phase shift and the interference of the light. On the other hand, laser frequency noise usually disturbs the phase of the laser directly or is coupled with the asymmetry of the length of the light path. Beam jitter degrades the interference of the beam. All these noises can be reduced using a laser stabilization technique, which is commonly applied in ground-based large-scale laser-interferometric GW detectors.

3.1.4.3 External Disturbances

The third category of noise sources is external disturbances. These include seismic noise, gravity gradient noise (Newtonian noise), residual gas noise and other noises induced by an exterior origin. In contrast to intrinsic noise and readout noise, some external disturbances can be attenuated or avoided using feedback control. In spite of the suppression system, the sensitivity of conventional detectors is normally limited by these noises in the low-frequency band, since the disturbances are much larger than the fundamental noises.

Seismic Noise

Even when an earthquake is not occurring, the ground is continuously vibrating. Its root-mean-square (RMS) amplitude is typically about several micrometers, thus the motion is unperceivable. This random motion can be a disturbance in the GW detector and in other precise measurements and is called seismic noise.

The spectrum of seismic noise is known to obey the empirical power-law approximately above frequency of 1 Hz:

$$\tilde{x}_{\rm seismic}(f) \simeq 10^{-6} \left(\frac{f}{1{\rm Hz}}\right)^{-2} \left[{\rm m}/\sqrt{\rm Hz}\right] \tag{3.26}$$

On the other hand, a broadband study at much lower frequencies has been conducted using a laser-interferometric strain meter [42] to search for quiet environments for future GW detectors. In this study, the seismic environment of some underground mines was investigated using observation frequencies of low as 10^{-7} Hz. It was found that seismic activity obeys the f^{-1} law in the low-frequency band. More specifically, the measured strain level was on the order of $10^{-3}/\sqrt{\rm Hz}$ at 10^{-6} Hz and $10^{-9} - 10^{-10}/\sqrt{\rm Hz}$ at 10^{-3} Hz.

Other Disturbances

There are other types of external disturbances which depend on the environment of the detector. For example, the following sources of noise must be considered for on-orbit TOBAs such as SWIM$_{\mu\nu}$: Magnetic coupling to the Earth's magnetic field, cosmic rays, the inhomogeneity of the Earth's gravity field, vibration of the carrying satellite and fluctuation of the rotation rate of the satellite. It can be a difficulty in optimizing the detector with the existence of these disturbances, since various effects of the disturbances can appear on the signal of the detector. For example, if there is practical mechanical imperfection (regarded as mechanical asymmetry), external vibration can be confused to rotational displacement signal which is searched for GWs.

3.2 Rotating TOBA

A TOBA utilizes a torsion bar as a test mass: thus, the TOBA can be rotated at a constant rate around its center. We refer to this as a rotating TOBA. The rotating TOBA has three novel characteristics that a conventional GW detector does not have: (i) frequency-upconversion of low-frequency GWs, (ii) doubling of the information provided by the detector and (iii) direct sensitivity to the circular polarization of GWs.

The idea for frequency conversion of GWs with a rotational rigid-body antenna was first proposed in early 1970's by Braginsky [2, 43], who focused on frequency-downconversion. He proposed a technique for accumulating GW signals of twice the rotational frequency to achieve a better S/N. In contrast, we focus on frequency-upconversion technique of GWs, as mentioned in [40]. This technique enables us to search for low-frequency GWs using signals in twice the rotation frequency.

In this section, we consider the detector response of a rotating TOBA. Note that some trivial dimensions such as x_0 and x_3 may be omitted in the following calculations.

3.2.1 Frequency Modulation of Gravitational Waves

We now set a local reference frame, i.e., the test mass of a TOBA rotates around its center in the reference frame. We can simplify the coordinate transformation in the GR framework so that the local reference frame has Lorentz coordinates.

Equation of Motion of Rotating TOBA

Let us consider an inertial reference frame, that is, we fix the incoming GWs. Then the metric of the GWs is expressed as

$$h_{ij} = \begin{pmatrix} h_+ & h_\times & 0 \\ h_\times & -h_+ & 0 \\ 0 & 0 & 0 \end{pmatrix} . \tag{3.27}$$

We assume that a TOBA is placed on the x-y plane ($z = 0$) and that the test mass is rotating around it center, i.e., z-axis. When the detector is rotated by angle ϕ, its quadrupole moment should be subjected to the rotational transformation law of a tensor:

$$R_i{}^j(\phi) = \begin{pmatrix} \cos\phi & \sin\phi & 0 \\ -\sin\phi & \cos\phi & 0 \\ 0 & 0 & 1 \end{pmatrix} . \tag{3.28}$$

Then the rotated quadrupole moment of the test mass q'_{ij} should be

$$q'_{ij} = R_i{}^l(\phi) R_j{}^m(\phi) q_{lm} \tag{3.29}$$

$$= q_\times \begin{pmatrix} \sin(2\phi) & \cos(2\phi) & 0 \\ \cos(2\phi) & -\sin(2\phi) & 0 \\ 0 & 0 & 1 \end{pmatrix} . \tag{3.30}$$

Using equations (3.27), (3.28) and (3.30) and applying the constant-rate rotation $\phi = \omega_{\mathrm{rot}} t$, we obtain

$$f_\theta(t) = \frac{1}{4}(q')^{ij}\ddot{h}_{ij}(t) \tag{3.31}$$

$$= \frac{1}{2} q_\times \left[\ddot{h}_\times(t)\cos(2\omega_{\mathrm{rot}} t) + \ddot{h}_+(t)\sin(2\omega_{\mathrm{rot}} t)\right] . \tag{3.32}$$

Equation (3.32) implies that the test mass senses the plus mode and cross mode simultaneously. From equation (3.32), we obtain the equation of motion for the rotational degree of freedom of the test mass as

$$I\ddot{\theta}(t) + \gamma\dot{\theta}(t) + \kappa\theta(t) = \frac{q_\times}{2}\left[\ddot{h}_\times(t)\cos(2\omega_{\mathrm{rot}} t) + \ddot{h}_+(t)\sin(2\omega_{\mathrm{rot}} t)\right] , \tag{3.33}$$

where I, γ and κ are the moment of inertia, damping coefficient and spring constant, respectively, and $\theta(t)$ is the rotational displacement.

Frequency Response of Rotating TOBA

Here $\tilde{g}(\omega) = \mathcal{F}[g(t)]$ denotes the Fourier transformation of the function $g(t)$. Here we give some relations involving the Fourier transformation. The Fourier transformation of a product is the convolution

$$\mathcal{F}[g(t)\cdot h(t)](\omega) = \int d\omega' \tilde{g}(\omega')\tilde{h}(\omega - \omega') . \tag{3.34}$$

using the expression for the inverse Fourier transformation of a sinusoidal signal,

$$\mathcal{F}[\cos(\nu t)](\omega) = \frac{1}{2}(\delta(\omega - \nu) + \delta(\omega + \nu)) \tag{3.35}$$

$$\mathcal{F}[\sin(\nu t)](\omega) = \frac{1}{2i}(\delta(\omega - \nu) - \delta(\omega + \nu)) , \tag{3.36}$$

we obtain

$$\mathcal{F}[u(t)\sin(\nu t)](\omega) = \int d\omega' \tilde{u}(\omega') \frac{1}{2i}(\delta(\omega-\omega'-\nu)-\delta(\omega-\omega'+\nu)) \quad (3.37)$$

$$= \frac{1}{2i}\left(\tilde{u}(\omega-\nu)-\tilde{u}(\omega+\nu)\right) , \quad (3.38)$$

and

$$\mathcal{F}[u(t)\cos(\nu t)](\omega) = \frac{1}{2}\left(\tilde{u}(\omega-\nu)+\tilde{u}(\omega+\nu)\right) . \quad (3.39)$$

Then we apply equations (3.38) and (3.39) to the Fourier transformation of the equation of motion (3.33):

$$\mathcal{F}[\text{right-hand side of (3.33)}] = -\frac{q_\times}{4}\Big[(\omega_{\rm L})^2\left(\tilde{h}_\times(\omega_{\rm L})-i\tilde{h}_+(\omega_{\rm L})\right) + (\omega_{\rm U})^2\left(\tilde{h}_\times(\omega_{\rm U})+i\tilde{h}_+(\omega_{\rm U})\right)\Big] \quad (3.40)$$

$$\mathcal{F}[\text{left-hand side of (3.33)}] = \left(-I\omega^2-i\gamma\omega+\kappa\right)\tilde{\theta}(\omega) \quad (3.41)$$

$$= H^{-1}(\omega)\tilde{\theta}(\omega) , \quad (3.42)$$

where

$$H(\omega) \equiv \left(-I\omega^2-i\gamma\omega+\kappa\right)^{-1} \quad (3.43)$$

$$\omega_{\rm L} \equiv \omega - 2\omega_{\rm rot} \quad (3.44)$$

$$\omega_{\rm U} \equiv \omega + 2\omega_{\rm rot} . \quad (3.45)$$

Thus, the equation of motion is transformed to

$$\tilde{\theta}(\omega) = \frac{\alpha H(\omega)}{\sqrt{2}}\Big[(\omega_{\rm L})^2\tilde{h}_{\rm LHS}(\omega_{\rm L}) + (\omega_{\rm U})^2\tilde{h}_{\rm RHS}(\omega_{\rm U})\Big] , \quad (3.46)$$

where $\alpha = -iq_\times/2$ is the shape factor. We consider that the signal frequency is higher than the resonant frequency of the suspension system; thus, $H(\omega)$ can be considered as $H(\omega) = -\frac{1}{I\omega^2}$. In addition, the polarization of the plane GWs is converted to circular polarization coordinates, i.e.,

$$\tilde{h}^{+z}_{\rm LHS} = \frac{1}{\sqrt{2}}(\tilde{h}_+ + i\tilde{h}_\times) \quad (3.47)$$

$$\tilde{h}^{+z}_{\rm RHS} = \frac{1}{\sqrt{2}}(\tilde{h}_+ - i\tilde{h}_\times) , \quad (3.48)$$

where $\tilde{h}^{+z}_{\rm LHS}$ and $\tilde{h}^{+z}_{\rm RHS}$ denote left-hand side and right-hand side circular polarization of

GWs from direction of $+z$, respectively. Then, equation (3.46) is also expressed as

$$\tilde{\theta}(\omega) = \frac{-\alpha}{\sqrt{2}I}\left[\left(\frac{\omega_{\mathrm{L}}}{\omega}\right)^2 \tilde{h}^{+z}_{\mathrm{LHS}}(\omega_{\mathrm{L}}) + \left(\frac{\omega_{\mathrm{U}}}{\omega}\right)^2 \tilde{h}^{+z}_{\mathrm{RHS}}(\omega_{\mathrm{U}})\right] . \tag{3.49}$$

Frequency Upconversion and Downconversion

Equation (3.49) denotes signal in the detector from the frequency-converted GWs by the rotating TOBA. Here we assume that the signal frequency for observation, ω_{sig}, is selected to be around the twice of the rotation frequency of the rotating TOBA, i.e.,

$$\omega_{\mathrm{sig}} = 2\omega_{\mathrm{rot}} + \omega_{\mathrm{L}} \ , \tag{3.50}$$

$$\omega_{\mathrm{L}} \ll 2\omega_{\mathrm{rot}} \ . \tag{3.51}$$

By definition, $\omega_{\mathrm{U}} = \omega_{\mathrm{sig}} + 2\omega_{\mathrm{rot}} \simeq 4\omega_{\mathrm{rot}}$. Thus, the amplitude of the signal of the detector $\tilde{\theta}(\omega_{\mathrm{sig}})$ is expressed as

$$\begin{aligned} \tilde{\theta}(\omega_{\mathrm{sig}}) &= \frac{-\alpha}{I}\left[\frac{1}{\sqrt{2}}\left(\frac{\omega_{\mathrm{L}}}{\omega_{\mathrm{L}}+2\omega_{\mathrm{rot}}}\right)^2 \tilde{h}^{+z}_{\mathrm{LHS}}(\omega_{\mathrm{L}}) + \frac{1}{\sqrt{2}}\left(\frac{\omega_{\mathrm{U}}}{\omega_{\mathrm{U}}-2\omega_{\mathrm{rot}}}\right)^2 \tilde{h}^{+z}_{\mathrm{RHS}}(\omega_{\mathrm{U}})\right] \\ &\simeq \frac{-\alpha}{I}\left[\frac{1}{\sqrt{2}}\left(\frac{\omega_{\mathrm{L}}}{2\omega_{\mathrm{rot}}}\right)^2 \tilde{h}^{+z}_{\mathrm{LHS}}(\omega_{\mathrm{L}}) + \sqrt{2}\tilde{h}^{+z}_{\mathrm{RHS}}(\omega_{\mathrm{U}})\right] . \end{aligned} \tag{3.52}$$

By comparing equation (3.16) for the static TOBA and equation (3.52) for the rotating TOBA, it is shown that the upconverted GWs are suppressed by the upconversion gain:

$$G_{\mathrm{up}}(\omega_{\mathrm{L}}, \omega_{\mathrm{rot}}) = \frac{1}{\sqrt{2}}\left(\frac{\omega_{\mathrm{L}}}{2\omega_{\mathrm{rot}}}\right)^2 \ , \tag{3.53}$$

and that the downconverted GWs are boosted by the downconversion gain:

$$G_{\mathrm{down}} = \sqrt{2} \ , \tag{3.54}$$

Effect of Uncertainty of Rotation Frequency on Observations

In the above calculation we assume constant rotation. Here we roughly estimate the effect of the uncertainty on the rotation frequency. Applying the variation of the rotational frequency, ω_{rot}, to the equation of motion, equation (3.33), we obtain

$$\tilde{\theta}(\omega) = \beta\frac{\omega_{\mathrm{gw}} - 2\delta\omega}{2(\omega_{\mathrm{rot}} + \delta\omega)}\left[\tilde{h}_{\times}\cos((\omega_{\mathrm{gw}} - 2\delta\omega)\,t) + \tilde{h}_{+}\sin((\omega_{\mathrm{gw}} - 2\delta\omega)\,t)\right] \ , \tag{3.55}$$

where β is a factor depending on the shape of the test mass and the transfer function of the mechanical system. This relation means that the variation of the signal frequency,

$\delta\omega_{\rm sig}$, is expressed as

$$\delta\omega_{\rm sig} = -2\delta\omega \ , \tag{3.56}$$

and the variation of the signal amplitude, δA, is expressed as

$$\frac{\delta A}{A} = 2\frac{\delta\omega}{\omega_{\rm gw}} + 2\frac{\delta\omega}{\omega_{\rm rot}} \ . \tag{3.57}$$

Using these relations, the requirements for rotational stability are derived. To avoid confusion with the frequency due to fluctuation of the rate of rotation, $\delta\omega$ should be within the following observational frequency bins:

$$\delta\omega < \frac{1}{2} \times 2\pi f_{\rm bin} \tag{3.58}$$

$$= \pi T_{\rm obs}^{-1} \ , \tag{3.59}$$

where $T_{\rm obs}$ is the observation time. At the same time, the amplitude fluctuation should be sufficiently small, i.e., the conditions

$$\delta\omega \ll \omega_{\rm gw} \tag{3.60}$$

$$\delta\omega \ll \omega_{\rm rot} \tag{3.61}$$

are required.

3.2.2 Advantages of Frequency Upconversion Technique

As mentioned before, the rotating TOBA has three characteristics that conventional GW detectors do not have. Each of them makes it advantageous to use a GW detector in astronomical observations.

3.2.2.1 Frequency Upconversion

According to equation (3.52), low-frequency GWs, $\tilde{h}_{\rm LHS}(\omega_{\rm gw})$, appear as the signal in the rotating TOBA, $\tilde{\theta}(\omega)$. In this case, we assume that the downconversion component of GWs, i.e., $h(\omega_{\rm U})$, is negligible compared with the upconversion component. This is justified when we search for a narrow-band SGWB such as a probe to primordial black holes predicted by [35]. In addition, this assumption is also valid in the observation of low-frequency continuous GW sources such as intermediate-mass to supermassive black-hole binaries.

In spite of this condition, the advantages of this frequency-upconversion technique are significant in terms of a novel methodology for GW observations. One of the advantages is that we can expand the observation frequency band to low-frequency range. In general, the noise in a lower frequency band is larger than that of a higher frequency band. Thus a lot of experimental technique has been developed to keep away the low-frequency noises from GW detectors. The frequency-upconversion technique provides a new way of avoiding these large noises. Note that this technique is only useful when the low-frequency noise spectrum of the detector has steep frequency dependence than $S_{\rm noise}(f) \propto f^{-2}$. This is because the signal of upconverted GWs is suppressed by the suppression factor, which decreases as the inverse square of the rotation frequency of the rotating TOBA, i.e., $G_{\rm up} \propto \omega_{\rm rot}^{-2}$ as shown in equation (3.53).

With the frequency-upconversion technique, observation frequency can be lower than the resonant frequency of the suspension. Test masses in a ground-based GW detectors are needed to be suspended by a pendulum or a similar mechanical system, and thus, the GW detector does not react to GWs in the frequency below the resonant frequency of the suspension. In other words, suspension system, which is inevitable in ground-based GW detectors, is also a hurdle of observations of low-frequency GWs. By using the frequency-upconversion technique, signals from low-frequency GWs are appeared to be (nearly) in twice the rotation frequency, which can be above the resonant frequency of the suspension system.

Another advantage is that we can choose observation frequency to avoid a narrow-band (high Q value) noise in a frequency of a GW. The target frequency of GWs cannot be modulated in an ordinary way, thus, the narrow-band GWs cannot be observed when the narrow-band noise exists at exactly the same frequency in the GW detector. Nevertheless, we can adjust the rotation frequency so that the signal frequency should be in the quieter observation band of the detector.

3.2.2.2 Multiplication of Detector Information

Another property of the rotating TOBA is that we can extract twice the amount of information from GWs as that obtained by the conventional detectors. This is because two frequency regions, $2\omega_{\rm rot} \pm \omega_{\rm gw}$, can be used for the observation. The conceptual diagram showing this phenomenon of the rotating TOBA is Figure 3.4. This can be also understood from equation (3.33), which implies that rotational displacement is induced by both plus and cross modes of GWs. This "heterodyne" operation is in contrast to conventional detectors, which can detect only either plus or cross GW polarization.

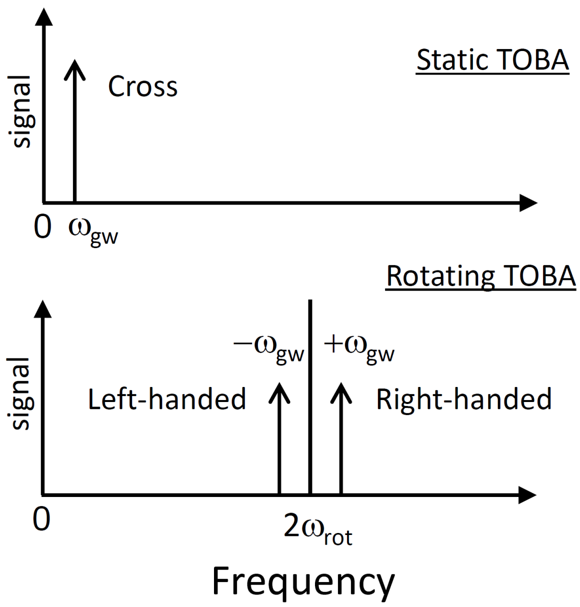

Figure 3.4: Conceptual diagram of the frequency-upconversion technique. The arrows denote the signal induced by GWs.

In an analogical view, a GW detector can be regarded as a single element of the telescope. This means that simultaneous observation with multiple detectors is necessary for GW astronomy. Thus, this property of doubling the amount of information is expected to be very useful from an astronomical viewpoint.

The two signals obtained from the two sidebands in rotating TOBA can be used in a correlation analysis for polarized GWs. The two GW signals corresponding to the two sidebands for perfectly-polarized GWs should be correlated. On the other hand, the noises in the signals are not correlated if the noise in a detector has a preferable characteristic, i.e., there is no correlations between the two signals in various frequencies. This method can be utilized to search for periodic GWs from pulsars. Note that the correlation analysis for SGWB cannot be conducted, since the two signals of SGWB do not have correlation.

3.2.2.3 Direct Sensitivity to Circular Polarization of GWs

The rotating TOBA has direct sensitivity to circular polarization of GWs. Although the array of a laser interferometer can be used to observe circular polarization, the rotating TOBA can be oriented in any chosen direction. This property is also advantageous for astronomy.

In Chapter 7, we use data obtained from the rotating TOBA, SWIM$_{\mu\nu}$, to search for and set an upper limit for these two modes of stochastic GW backgrounds. Thus, we should consider the response of the rotating TOBA to the GWs from all over the sky. We neglect downconverted GWs. Equation (3.47) and (3.48) are derived from the wave coming from $+z$, i.e., from zenith. In addition, considering the incoming wave from nadir, definitions of the left-hand side and the right-hand side wave are exchanged to each other, i.e.,

$$\tilde{h}^{-z}_{\rm LHS} = \frac{1}{\sqrt{2}}(\tilde{h}_+ - i\tilde{h}_\times) \tag{3.62}$$

$$\tilde{h}^{-z}_{\rm RHS} = \frac{1}{\sqrt{2}}(\tilde{h}_+ + i\tilde{h}_\times) \ . \tag{3.63}$$

We also apply them to equation (3.49), and utilize the relation that negative frequency should be treated as same as the positive frequency, from the aspect of the one-sided spectral density picture. Then, the following results of the response of the rotating TOBA, summarized in Figure 3.5 are derived.

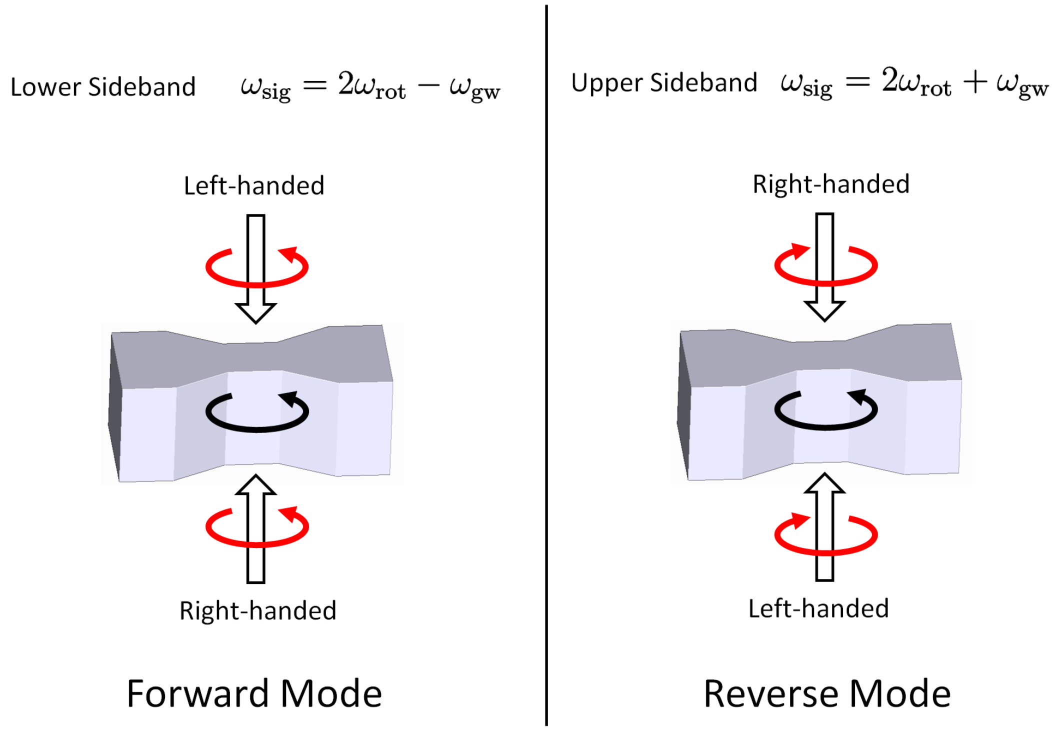

Figure 3.5: Two separation modes of the rotating TOBA.

The lower sideband induced by the GWs, whose signal frequency satisfies

$$\omega_{\rm sig} = 2\omega_{\rm rot} - \omega_{\rm gw} \ , \tag{3.64}$$

contains information on the sum of the left-hand-side circular polarization from the zenith and the right-hand-side polarization from the nadir. We call this superposition of the two incoming GWs with circular polarization the "forward mode". In contrast, the upper sideband induced by GWs, whose signal frequency satisfies,

$$\omega_{\rm sig} = 2\omega_{\rm rot} + \omega_{\rm gw} \ , \tag{3.65}$$

contains information on the opposite superposition of circularly polarized GWs. We name this the "reverse mode".

3.2.3 Disadvantages

The frequency-upconversion technique has disadvantages at the same time. The most significant disadvantages are the following two points. First, the amplitude of low-frequency GWs decreases due to the conversion gain. As shown in equation (3.53), the upconversion gain is inversely proportional to the square of the rotating frequency, i.e., observation frequency. Thus, when we utilize this technique to avoid the noise in the low-frequency, the floor level of the noise should decrease rapidly than f^{-2} as the frequency increases. Second, disturbances which affect the test mass of the TOBA in the same way as the GWs do, are also frequency-converted. An example is the Newtonian noise. A method to avoid the noises from this type of confusion should be considered in the future work.

3.3 Summary

A TOBA is a novel type of GW detector for low-frequency GW observations that has been proposed recently [40]. It is based on a property of GWs that the tidal force induced by GWs causes the rotational motion of a test mass suspended in the TOBA. In contrast to ordinary laser interferometers, a test mass in a TOBA can be suspended by a "soft" system, namely, it has a lower resonant frequency; thus, the TOBA has higher sensitivity to low-frequency GWs. Prototype detectors have been developed, and observations of 0.1-Hz-band stochastic GW backgrounds have been conducted.

The entire TOBA system can be rotated around its center. We named a TOBA with this type of operation the rotating TOBA. We proposed a frequency-upconversion technique for low-frequency GWs using a rotating TOBA. A rotating TOBA has three advantages over an ordinary detector. First, the frequency-upconversion of low-frequency GWs can be realized. Second, twice as much information is extracted from the detector as from conventional detectors. That is because two frequency regions can be used for the observation. Finally, the rotating TOBA has direct sensitivity to circular polarization (more precisely, its anisotropy). It is pointed out that the rotating TOBA can be used as a new tool in spaceborne missions to detect low-frequency GWs.

Chapter 4

Spaceborne Torsion-Bar Antenna: $\mathrm{SWIM}_{\mu\nu}$

A means of observing low-frequency GWs is to place the detector in space. This has some advantages over ground-based observations including long baseline, stable environment and no need for a suspension system. We developed a module consisting of a tiny spaceborne TOBA called $\mathrm{SWIM}_{\mu\nu}$ and demonstrated its technologies' feasibility for use in next-generation space missions [44].

In this chapter, structure and function of $\mathrm{SWIM}_{\mu\nu}$ are presented in detail. First, the advantages of spaceborne detectors and the expected role of $\mathrm{SWIM}_{\mu\nu}$ in development of next-generation missions are described. Second, the detector components such as the torsion-bar antenna module, feedback control system and data acquisition system are described. Details of the satellite carrying the detector, called SDS-1, are then explained.

4.1 Spaceborne Detectors

Generally, the cost of spaceborne detectors is very high. However, they provide valuable scientific results that only space instruments can reveal. Here we highlight nine reasons justifying the research in space.

1. Space exploration: the fact that the targets of the research exist in space. Planetary science and plasma science are examples of fields that can benefit from research with spaceborne instruments.

2. Observations of Earth: observation from space is essential when the whole surface

of the Earth needs to be in visual contact. Communications, spy satellites and navigation are applications of such observations.

3. Cosmic radiation from outer space: observation from space enables the barrier of the atmosphere to be avoided. When we wish to observe what cannot be seen from the ground, satellite experiments are needed. X-ray, infrared and radio astronomy require satellite equipments.

4. To avoid noises on Earth: the Earth itself generates noises that may hinder observations such as seismic and Newtonian noises.

5. Large vacuum: space provides large vacuum environment. Pumps, long tubes and other vacuum instruments on the ground are very expensive.

6. Large area: space provides a very large area that cannot be allocated on Earth. For example, solar power plants require such a large area to generate sufficient electricity.

7. Long distance: when a long distance that cannot be achieved on Earth is vital for observations, space can be used. For example, GW telescopes and very long baseline interferometry (VLBI) both requires long distances.

8. Long-duration microgravity: space can provide a microgravity environment for the study of space biology and advanced materials sciences.

9. Physical characteristics of satellite orbit: space can be used for experiments that require a very high speed and large gravitational potential differences. Atomic clocks and testing of the theory of relativity such as by using Gravity Probe B are included in this category.

Among the above, laser interferometric GW telescopes in space have the following four requirements. (1) A long distance in space is required for the detector to reach the low-frequency band. (2) Noises from the Earth such as seismic noise and Newtonian noise must be avoided to enable observation of the low-frequency GWs. (3) Microgravity is required to allow a free mass without suspension to be used, extending the range of observation frequency to lower than the resonant frequency of the suspension system. (4) A large vacuum is required to replace the long tube used in ground-based laser interferometers. Note that the tubes in large interferometers are a significant part of their cost.

In terms of a spaceborne TOBA, (2) and (3) mentioned above are the important reasons why a spaceborne detector have a better sensitivity. In addition, microgravity in space enables the TOBA to rotate easily. This is also an significant advantage of space environment for a rotating TOBA.

4.2 SWIM$_{\mu\nu}$: Overall System Configuration

To realize a spaceborne TOBA for the first time and to demonstrate key technologies needed by future spaceborne GW detectors, a tiny spaceborne TOBA named SWIM$_{\mu\nu}$ has been developed.

Hardware

A schematic view of the hardware system of SWIM$_{\mu\nu}$ is shown in Figure 4.2, and picture of SWIM$_{\mu\nu}$ is shown in Figure 4.1. Figure 4.2 illustrates connections between the two torsion-bar antenna modules (TAMs) and the four electronics boards. From SpaceCube2, which is a space-qualified computer equipped with SpaceWire interface, two lines of SpaceWire are connected to SWIM$_{\mu\nu}$. One of them goes to the digital board, which has an field programmable gate array (FPGA) for digital filtering, packet generation and data storage. The other line goes to the SpaceWire test board, the aim of which is to demonstrate new SpaceWire electronic devices for space. The SpaceWire test board and the digital board are also linked with SpaceWire; thus, they form a triangular setup connected by SpaceWire. Normally mission data packets generated by the digital board are transferred to SpaceCube2 directly via SpaceWire. In the case of a problem, such as a failure of the direct connection, the data can avoid the direct connection by using a bypass route around the SpaceWire test board.

SWIM$_{\mu\nu}$ has two TAMs at its bottom. The four electronics boards are attached above them. The two TAMs have exactly the same design and structure (except for the model of the environmental sensors). They are set with their bottom panels attached to each other. This configuration enables the interior test masses to be perpendicular to one another. This layout is needed for the TOBA with two test masses as described in Figure 4.2.

The four electrical boards shown in Figure 4.2 are called SpaceWire test board, digital board, digital-to-analog converter (DAC) board and analog-to-digital converter (ADC) board from top to bottom. The ADC board has four analog-to-digital integrated circuits (ICs) for converting analog signals from the two TAMs. The DAC board has eight digital-to-analog ICs to drive the coil currents for the coil-magnet actuators in the TAMs. Digital board has an FPGA. The FPGA includes digital proportional-integral-derivative (PID) filters for positional control of the test masses. In addition, the logic circuits in the FPGA contain a SpaceWire intellectual property (IP) core, which realizes SpaceWire

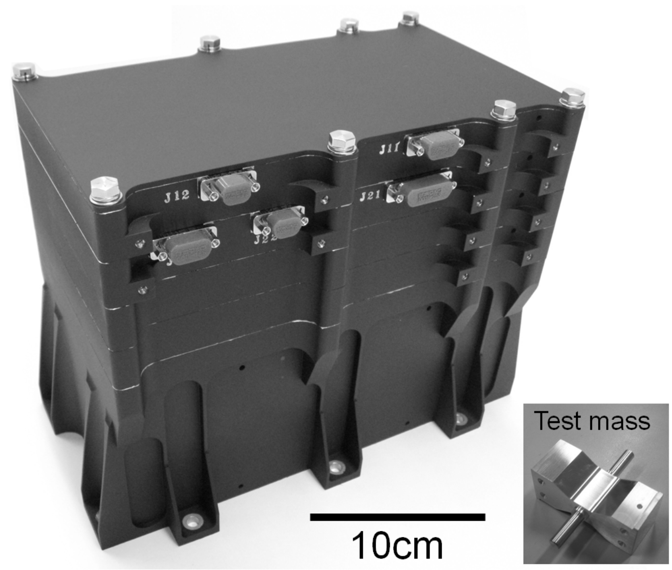

Figure 4.1: SWIM$_{\mu\nu}$ and the test mass.

communication with SpaceCube2. The SpaceWire test board at the top of the figure has no relation with the GW detector. It was launched to demonstrate various space-qualified devices. Some parameters of SWIM$_{\mu\nu}$ are shown in Table 4.1.

Table 4.1: Parameters of SWIM$_{\mu\nu}$.

Parameter	Value	Unit
Weight	3.67	kg
Size	$224 \times 124 \times 102$	mm^3
Power consumption (Idle)	2.4 ± 0.3	W
Power consumption (Observation)	7.0 ± 0.3	W
Temperature range (OFF)	-30 — 60	°C
Temperature range (ON)	0 — 40	°C

Power Supply

The electrical power provided by the satellite bus system is 28 V direct current (DC). The direct current to direct current (DC/DC) converter on a panel in SpaceCube2 converts it to voltages of +5 V and ±15 V for SWIM$_{\mu\nu}$. These three DC, i.e., +5 V and ±15 V power are sent to the digital board. There are semiconductor field-effect transistor (FET) switches on the board, and we can switch the rest of the system on and off by sending

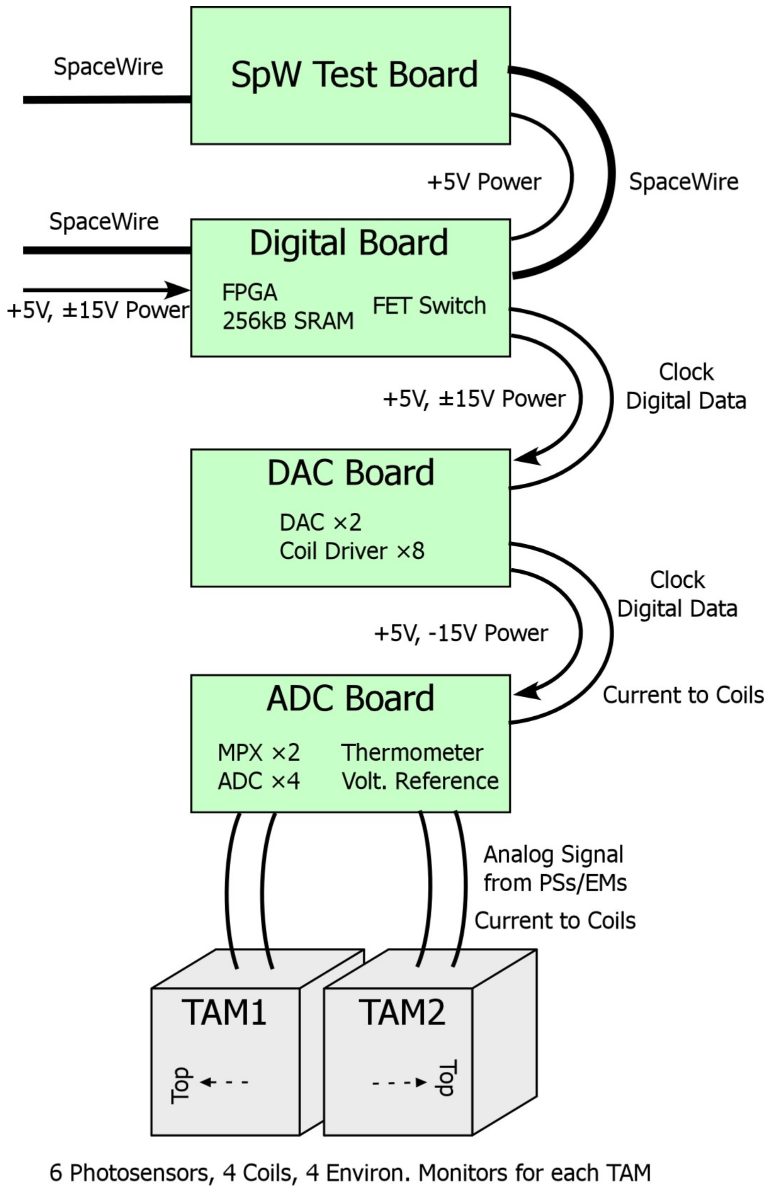

Figure 4.2: Schematic view of hardware configuration of SWIM$_{\mu\nu}$.

commands through the SpaceWire.

The configuration of the power supply system to SWIM$_{\mu\nu}$ is shown in Figure 4.3.

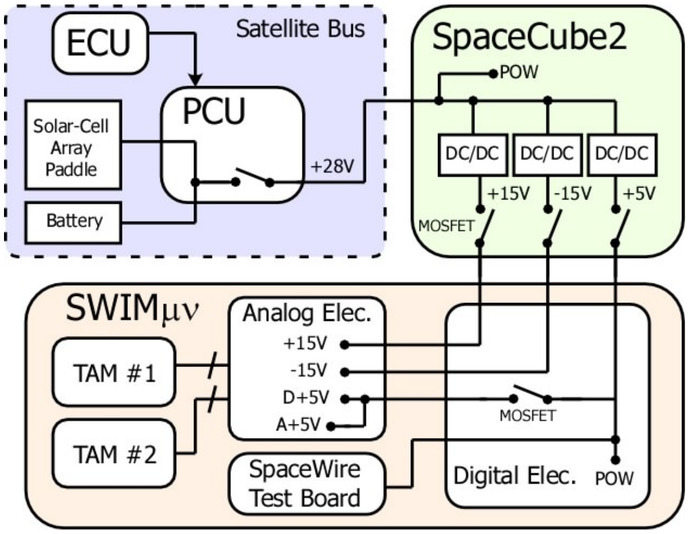

Figure 4.3: Block diagram of power supply system to SWIM$_{\mu\nu}$. SpaceCube2 and SWIM$_{\mu\nu}$ are shown in solid boxes, while the satellite bus is shown in the box with the dotted line. In SWIM$_{\mu\nu}$, the ADC board and the DAC board are described together in terms of analog electronics. "D+5V" and "A+5V" denotes the 5 V power lines for the digital and analog systems, respectively. "DC/DC" stands for the DC/DC converter IC. The power supply of each component is shown as "POW". The grounding configuration is not presented in this figure.

4.3 Detector

In this section, we explain the structure and function of the module of the GW detector called TAM. Figure 4.4 shows the internal structure of the TAM. Its external shape is a cube of size 80 mm. It has a test mass made of aluminum, six infrared photoreflective sensors, four coils for actuators, and sensor modules for environmental monitoring.

4.3.1 Test Mass

The most important part of the detector is the test mass. Figure 4.5 displays the configuration of components around the test mass. The test mass is made of aluminum with a mass of 50 g and is controlled to avoid contact with the frame. The moment of inertia of the test mass around its axis, I is 1.2×10^{-5} kg m^2.

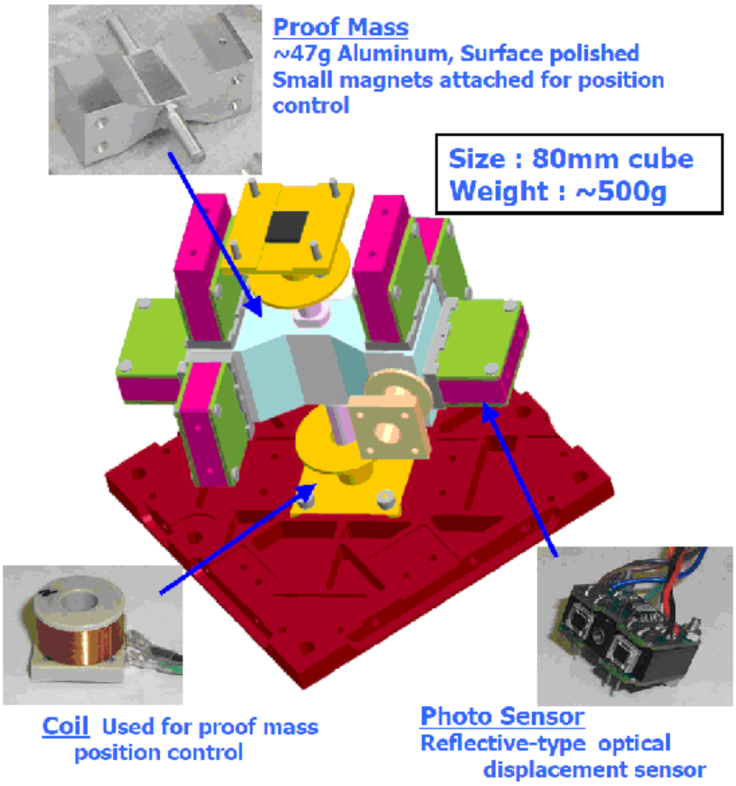

Figure 4.4: Structural view of TAM. All panels except for that at the bottom are removed in this figure. The test mass is located at the center. The six photoreflective position sensors surrounding the test mass are represented as boxes. Coil bobbins are also shown. The position sensors and coils are attached to the aluminum frame, which is removed in this picture. Sensors modules for environmental monitoring are set in the TAM but are not shown in this figure.

Its length is 50 mm and distance between the two sensing point for the displacement sensors is 40 mm. The test mass is cut out in its center, so that its weight should be reduced and its response to incoming GWs should be increased at the same time. The surface of the test mass is polished, so that the infrared light emitted from the LED in the photoreflective sensor is reflected on the surface.

Four magnets are attached to the test mass to form the coil-magnet actuator with the coils on the frame for feedback controls of the position. Two magnets are contained in the axle of the test mass and are for the feedback control of vertical motion. The other two magnets are attached directly to the surface of the test mass, and are for the rotational feedback control system.

The test mass has six degrees of freedom (DoFs). The coordinates is also shown in

Figure 4.5. The three translational motion is called as same as the axis; x, y and z, and the three rotational DoFs, *yaw*, *pitch* and *roll* are defined as the revolution around z, x and y axes, respectively. The motion of the test mass in these six DoFs are treated as follows. The feedback control system is used for the unstable DoF, z. The *yaw* DoF, which is used in the observation of GWs is also controlled to the locking point to conduct a measurement of the disturbance. While, the other four DoFs, x, y, *pitch* and *roll* are not actively stabilized. This is because the magnets in the axle of the test mass and the iron cores attached to the frame attract each other, and thus the four DoFs do not need feedback control owing to the magnetic potential.

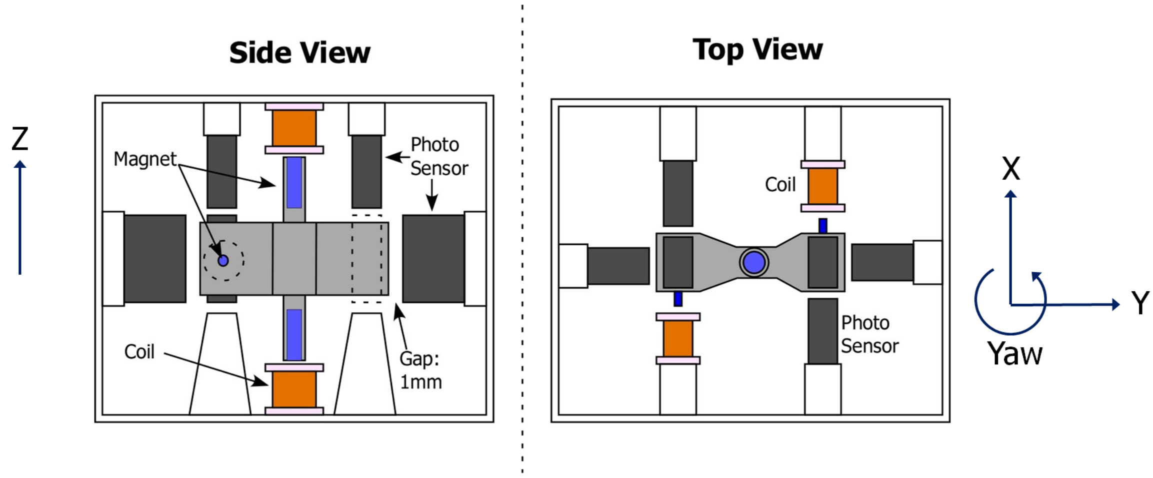

Figure 4.5: Cutaway view of the test mass and surrounding sensors and actuators. The detector coordinate system is also shown. The left figure shows a side view, while the right figure shows a top view. All components and gaps are displayed at the same magnification. Structure of the aluminum frame and environment monitoring sensors are not presented here.

4.3.2 Photoreflective Displacement Sensors

To sense the displacement between the proof mass and the frame, the six photoreflective sensors are placed around the test mass. Because of the insufficient room and electrical power in a small satellite, we chose photoreflective sensors instead of laser-interferometric displacement sensors.

Infrared light about 900 nm is used in the sensors. An light emitting diode (LED) of model L3458 by Hamamatsu [45] emits infrared light. Photodiodes (PDs) of model S2833 by Hamamatsu [46] detect the light reflected from the surface of the test mass.

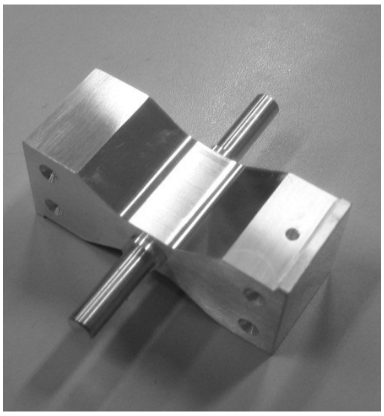

Figure 4.6: Test mass in TAM. The magnets for *yaw* control are removed in this picture.

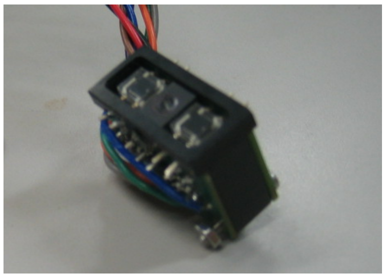

Figure 4.7: Photoreflective displacement sensor.

The parameters of the LED and the PD are shown in Table 4.2 and 4.3, respectively. The intensity of the light, which depends on the distance between the proof mass and the photoreflective sensors, is read out by the pair of the PDs shown in Figure 4.7. In addition, two PDs are mounted within the frame of the sensor to monitor the intensity of the emitting light from the LED.

To save the electricity, the duty cycle of each LED is a sixth; The six LEDs in the sensors surrounding the test mass turn on alternately and the timing of the data acquisition of the displacement signal is synchronized to the timing of the lighting of the LEDs. The sequence is controlled by the FPGA.

Table 4.2: Parameters of the LED used in the photoreflective sensor.

Parameter	Value
Model number	L3458
Manufacturer	Hamamatsu
Peak emission wavelength	890 nm (typical)
Half bandwidth of emission	50 nm
Emitting power	13 mW
Cutoff frequency	1 MHz

Sensitivity and Radiation Test

The noise level of the sensor is shown in Figure 4.8. The displacement noise level of

Table 4.3: Parameters of the PD used in the photoreflective sensor.

Parameter	Value
Model number	S2833-01
Manufacturer	Hamamatsu
Size of acceptance surface	2.4 mm × 2.8 mm
Sensitive wavelength range	320 — 1100 nm
Wavelength at maximum sensitivity	960 nm
Quantum efficiency	0.58 A/W
Transition time	2.5 μs
Dark current	10 pA (max.)
Junction capacitance	700 pF
Shunt resistance	100 GΩ

the sensor is about 10^{-9} m/$\sqrt{\text{Hz}}$ at frequencies up to 1 Hz. The sensitivity is limited by the noise of the op-amp of the first stage amplifier, which converts photocurrent from PDs into voltages.

The measurement was also conducted after the sensor had been radiated by 662 keV gamma ray of 10 krad from ^{137}Cs. The total dose of 10 krad is equivalent to the expected radiation in four years of operation in orbit. It is confirmed that the radiation of gamma-ray does not affect the sensitivity of the sensors.

The calibration factor of the sensor is also measured. The results of this measurement is shown in Figure 4.9. The output of the sensor varies as the distance between the surface of the sensor and a mirror increases. The operation point of the sensor is the position that the distance is around 1 mm, thus, the calibration factor is approximately 1 V/mm. Note that the signal of the intensity monitor is insensitive to the variation of the distance.

4.3.3 Coil-magnet Actuators

To actuate the test mass, four neodymium (Nd) magnets are attached to it, and four coils are placed in front of these magnets. A picture of the coil is shown in Figure 4.10. The feedback control system applies currents to the coils to generate forces opposite those generating a disturbance so that the test mass maintains its equilibrium position. We selected coil-magnet-type actuators to apply a force to the test mass for the feedback system. This is because this type of actuator is the most robust type and operates unless the current wire or magnet is broken. Another possible contactless actuator is the

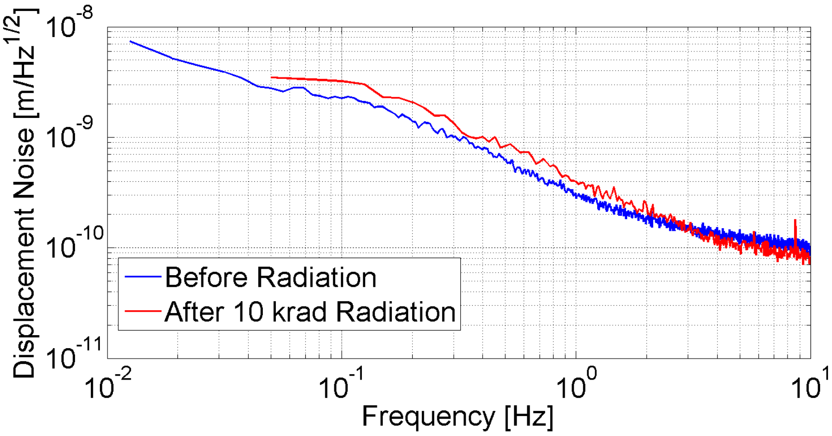

Figure 4.8: Noise level of the photoreflective sensor. Noise spectra of the photoreflective sensor and that of the sensor which is exposed to the radiation of gamma-ray, are plotted.

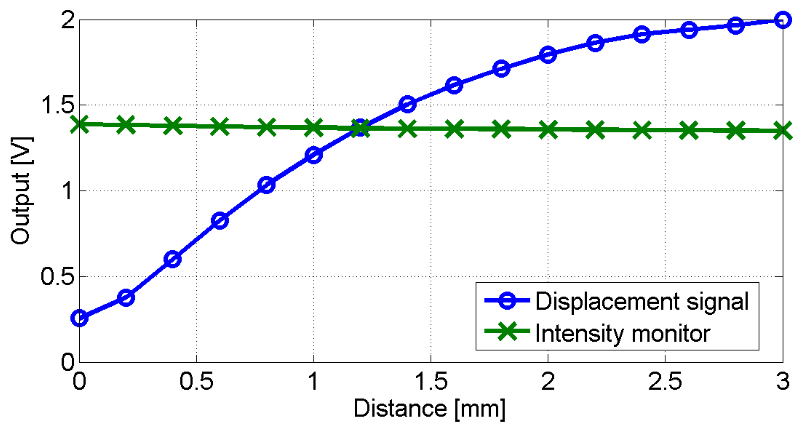

Figure 4.9: Response of the photoreflective displacement sensor. Two signals corresponding the two pairs of PDs, i.e., displacement signal and LED intensity monitor, are shown.

electrostatic actuator. However, it has the disadvantage that it requires a high voltage of several hundred volts to operate. In addition, it may apply a too weak force to move the test mass of 50 g. We wanted a control force that was as strong as possible so that the test mass could be moved to the correct position if any disturbance occurred. Thus, a sufficiently strong force rather than low noise was preferred in this case.

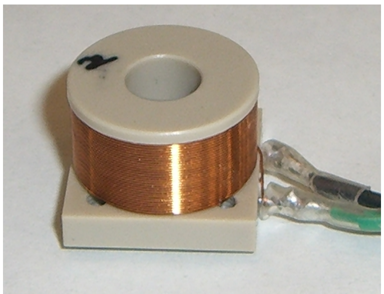

Figure 4.10: Coil for actuator.

The bobbin case for the coil is made of plastic which have low mass-loss in vacuum. The Nd magnet is its counterpart and is used to receive the driving force of the magnetic field induced by the coils. The result of the force measurement to determine the calibration factor of the actuators is shown in Figure 4.11. The calibration factor of the actuator for the z control is -0.882 N/A. The calibration for the actuators for the *yaw* control has been done with the two different magnets, to distinguish the variation in magnetic moment of the Nd-magnets. The results are -0.155 N/A and -0.161 N/A. It has been confirmed that the actuators have adequate linearity and repeatability to be used in the feedback control loop.

4.3.4 Digital Servo System

To keep the test mass at the correct position to operate the sensor in a linear range, a digital servo system was installed. The system has four main functions: analog-to-digital conversion, digital filtering, AD/DA front-end electronics and digital filtering in the FPGA. The digital position control loop operates as follows. Displacement signals from the photoreflective sensors are multiplexed and converted to 16-bit digital values by the ADCs. Then FPGA acquires the data and applies the data to a digital PID filter implemented on the FPGA, while the FPGA converts the data into a packet for the data acquisition (DAQ) system. Filtered signals are sent to the DACs, which convert the signals into the currents in the coils.

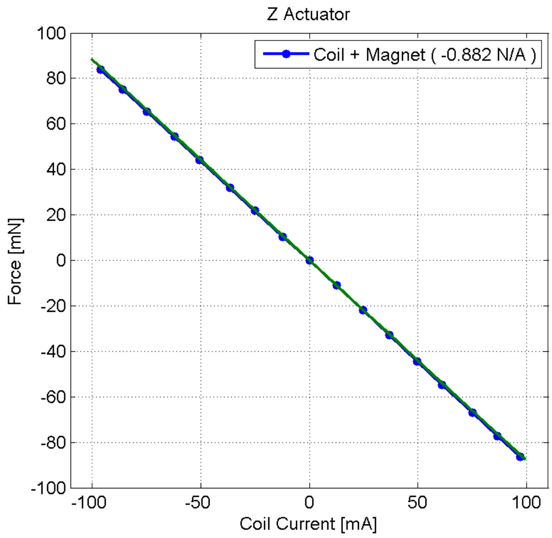

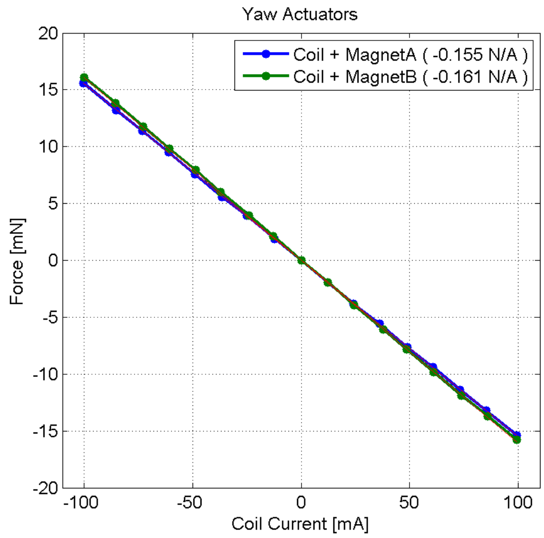

Figure 4.11: Results of the force calibration of the coil-magnet actuator. The left plot shows the force of the actuator used in the z (vertical) control, and the right plot shows the forces of the actuator used in the *yaw* control.

Since the disturbance to the test mass is monitored, the sensor also acts as a sensitive accelerometer, especially in the angular direction. Therefore, SWIM$_{\mu\nu}$ can measure the vibration of the satellite, which is not a well-studied noise source of space GW detectors. The TAM also have on-chip gyros and accelerometers as environmental monitoring sensors, which are utilized to calibrate the main sensor.

Digital PID Filter

Figure 4.12 shows the transfer function of the PID filter used for "z" degree of freedom (DoF) control. Because of the small number of the gate of the FPGA, the three parameters determining P, I and D for the PID filter can be varied in a limited range. The total transfer function of the filter is expressed as

$$\mathrm{H}(f) = G_{\mathrm{P}} + \mathrm{C}\frac{T_{\mathrm{clock}}}{2\pi i f}G_{\mathrm{I}} + \mathrm{C}\frac{2\pi i f}{T_{\mathrm{clock}}}G_{\mathrm{D}} \ . \tag{4.1}$$

where f, G_{P}, G_{I} and G_{D} are the frequency, the gains of P, I and D, respectively. The constant, C, is a parameter for the time delay due to the logic circuits in the FPGA. Its value is 8 in this case. T_{clock} is the timing interval of the filtering. For this PID filter, the original clock frequency of 33 MHz obtained from the crystal oscillator is divided by 61440

($= 32 \times 60 \times 8 \times 4$) using a clock divider inside the FPGA. Thus, filtering frequency is

$$1/T_{\mathrm{clock}} = 537.11 \text{ Hz} . \tag{4.2}$$

Note that the frequency accuracy of the crystal oscillator is certified to be ±15 ppm at 25 °C, and the stability in temperature from -55°C to 125°C is within ±50 ppm.

We chose the default filter parameters in Table 4.4, so that initial control of the test mass succeeded in the laboratory test. Using these parameters, we derived the filter gain for z and *yaw* control as shown in Figure 4.12.

Table 4.4: Parameters for PID Filter.

Parameter	G_{P}	G_{I}	G_{D}
yaw (Horizontal) control	1	0	0.5
z (Vertical) control	32	0	16

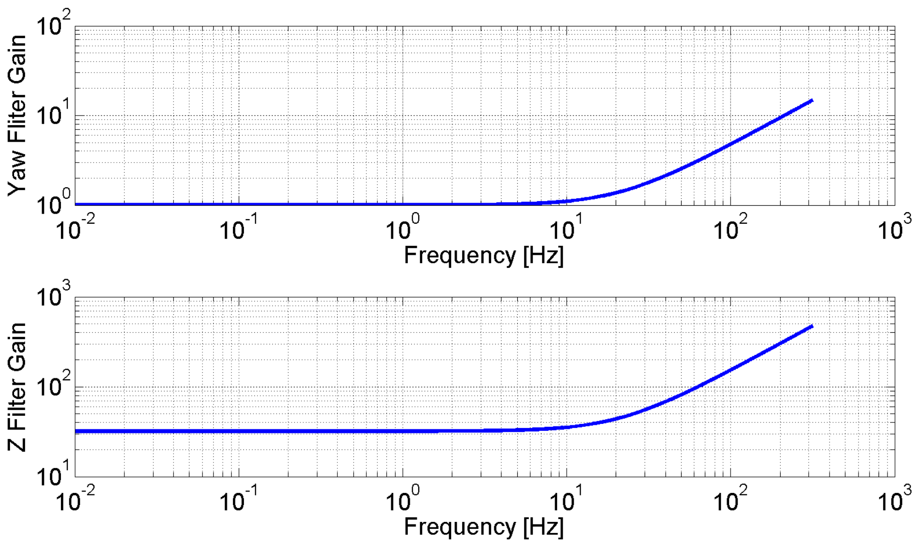

Figure 4.12: PID filter gain. The top graph shows *yaw* control, while the bottom graph shows Z control.

4.3.5 Command and Data Processing Unit

Functional block diagram of the command and data processing unit is shown in Figure 4.13. We collected scientific data as follows. First, data packets generated by the FPGA from sensor signals are stored temporarily in a 256 KByte buffer in SWIM$_{\mu\nu}$. The buffer can store 5.4 s of data since the FPGA creates data at a rate of $\sim$ 380kbps. When the buffer is over half full, SpaceCube2 begins to pull up the data packets from the buffer via SpaceWire. The received data packets are stored in a 512 MByte data recorder within SpaceCube2. Finally, the detector control software sends the data to the ground station via the main computer of the satellite bus system.

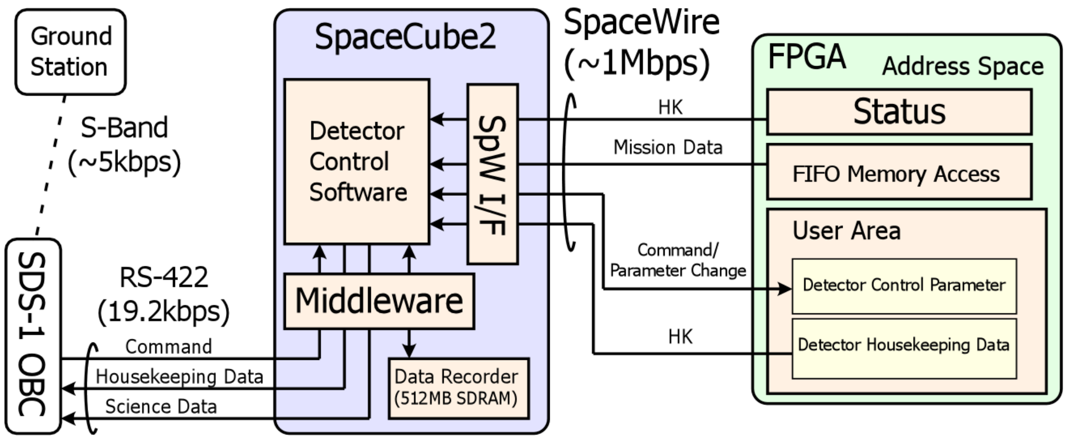

Figure 4.13: Functional diagram of the data handling system.

SpaceWire and SWIM

To collect data from the sensors, we adopted a SpaceWire-based data acquisition framework. SpaceCube2 [47], a space-qualified computer equipped with SpaceWire interface [48], and the FPGA in SWIM$_{\mu\nu}$ are linked by SpaceWire and communicate with each other via SpaceWire/RMAP (Remote Memory Access Protocol) [49] at a speed of 900 kbps. SpaceWire is a new-generation communication standard for onboard equipment, developed cooperatively by ESA, JAXA, NASA, Roscosmos and other space agencies. It is becoming increasingly widely adopted in onboard scientific instruments. SpaceWire will be utilized in next-generation scientific satellites such as ASTRO-H [50] and in the small scientific satellite program [51] of JAXA.

4.3.6 Environmental Monitoring Sensors

In order to monitor the environment in the TAM on the satellite, two accelerometers and two gyroscopes, which are called environmental monitoring (EM) sensors, are assembled as a square-shaped module and are mounted on the TAM. The EM sensors are based on micro electronics and mechanical system (MEMS) technology. They are commercially-produced on-chip sensors, which is widely used in the automobile and electronics industry. In the EM sensor module, two different model of accelerometer and gyroscope are selected to use. This is because the configuration has a redundancy, and because we can test the different model of commercial EM chips in a orbital environment, such as thermal cycle and cosmic radiations. Parameters of the EM sensors are summarized in Table 4.5.

Accelerometer is a sensor of an acceleration. The principle of operation for the accelerometer used as the EM sensor is the measurement of the inertial force applied to the micro-machined mass within the package. Their sensitivity is approximately 1000 mV/G. This sensitivity is ordinary for a MEMS accelerometer.

Gyroscope is a rotation rate sensor. Its principle of operation is the measurement of Coriolis force to the dither frame in the package. The MEMS gyroscopes used in the EM sensors have the sensitivity of approximately 15 mV/(deg/s).

In addition, a temperature sensors are contained in the same package of the gyroscopes, so that we can calibrate the temperature dependence of the gyroscope to obtain better accuracy of measurement of the rotation rate. The temperature outputs from the gyroscope are also read out and are recorded. We are able to obtain information on the temperature change in the TAM through these sensors[1]. The sensitivity is 8.4 mV/K.

Table 4.5: Parameters of the EM sensors.

Parameter	ADXL103	AGS11151	ADXRS401	ADXRS150
Type	Accelerometer	Accelerometer	Gyroscope	Gyroscope
Manufacturer	Analog Devices	Matsushita elec.	Analog Devices	Analog Devices
Dynamic range	± 1.7 G	± 2.0 G	± 75 deg/s	± 150 deg/s
Sensitivity	1000 mV/G	1333 mV/G	15 mV/(deg/s)	12.5 mV/(deg/s)
Supply current	0.7 mA	5 mA	6 mA	6 mA

4.3.7 Control System and Design Sensitivity

To clarify the relation among noise, disturbance and sensitivity, the block diagram of the feedback control loop is shown in Figure 4.14. Here, the transfer function of the test

[1]Principles of operations are not described in the data sheets. The author suppose that the principle is based on a bandgap voltage reference, which generates a proportional to absolute temperature (PTAT) current by using a resistor in the circuit.

mass H_{TM} is determined by equation (3.43). H_{TOBA} denotes the product of the shape factor and square of signal frequency, i.e.,

$$H_{\mathrm{TOBA}} = \frac{q_\times}{2}\omega^2 \ , \tag{4.3}$$

for the static TOBA and

$$H_{\mathrm{TOBA}} = \frac{q_\times}{2\sqrt{2}}\omega_{\mathrm{gw}}^2 \ , \tag{4.4}$$

for the rotating TOBA. And the transfer function of the filter is determined by equation (4.1). The value of the other elements such as sensors and actuators are discussed later in Section 5.3.

Design Sensitivity

The expected design sensitivity of SWIM$_{\mu\nu}$ is shown in Figure 4.15. The spectrum corresponds to the strain of GWs at the point A in Figure 4.14. The sensitivity is approximately $1\times 10^{-7}/\sqrt{\mathrm{Hz}}$ at 0.1 Hz. To achieve this design sensitivity, the following conditions are assumed.

- The disturbances to the detector, shown as point E and F in Figure 4.14, are sufficiently small so that the sensitivity is not dominated by the noise level of these incoming disturbances.
- The noise of the feedback control loop is limited by the noise of the photoreflective sensors, i.e., analog-to-digital conversion, digital filtering and coil-magnet actuators have sufficiently less noise than the displacement sensors. This assumption is confirmed by the measurement of output noise level of the actuators.
- The resonant frequency in the rotational DoF of the magnetic potential, which supports the test mass, is sufficiently lower than the frequency. This means that the resonant frequency is much lower than 10^{-2} Hz (e.g. 10^{-4} Hz).

These premises are summarized in Table 4.6.

Energy-Density Equivalent Sensitivity

When we want to interpret the design sensitivity not as strain h but as the sensitivity to the energy density normalized by closure density of the Universe Ω_{gw}, the strain sensitivity should be converted using the relation

$$\Omega_{\mathrm{gw}}(f) = \frac{10\pi^2}{3H_0^2} f^3 h^2(f) \ , \tag{4.5}$$

Table 4.6: Premises for the estimation of detector design sensitivity.

Item	Description
Sensor noise	measured noise spectrum
Quantization noise	Supposed to be small
Actuator noise	Ignored (confirmed to be sufficiently small)
Rotation rate fluctuation	Supposed to be small
Rotational disturbance	Supposed to be small
Resonant frequency of suspension	$\sim 10^{-4}$ Hz

which is derived in Chapter 7. Thus these sensitivities at two different frequencies, 2×10^{-7} $/\sqrt{\text{Hz}}$ at 20 mHz and 1×10^{-7} $/\sqrt{\text{Hz}}$ at 100 mHz are interpreted as

$$\Omega_{\text{gw}}(20\ \text{mHz}) = 8.2 \times 10^{17} \ , \tag{4.6}$$

and

$$\Omega_{\text{gw}}(100\ \text{mHz}) = 2.6 \times 10^{19} \ , \tag{4.7}$$

respectively.

4.4 Satellite

The satellite carrying SWIM$_{\mu\nu}$ is Small Demonstration Satellite-1 (SDS-1) [52–54], developed by JAXA. SDS-1 is one of the small demonstration satellite (SDS) series developed with the aim of demonstrating spaceborne equipment cheaper, faster and more frequently than in conventional space development. It was launched into sun-synchronous polar orbit on January 23, 2009. SWIM, which consists of SWIM$_{\mu\nu}$ and SpaceCube2, aims to verify SpaceWire-based communication system and onboard scientific experiment framework, taking advantage of the quick and low-cost small satellite program. The major parameters of the satellite are listed in Table 4.7.

4.4.1 Satellite Bus System

Note that detectors onboard a satellite cannot be operated without sufficient knowledge of the bus system. Figure 4.17 shows a functional block diagram of the bus system.

Processing Units

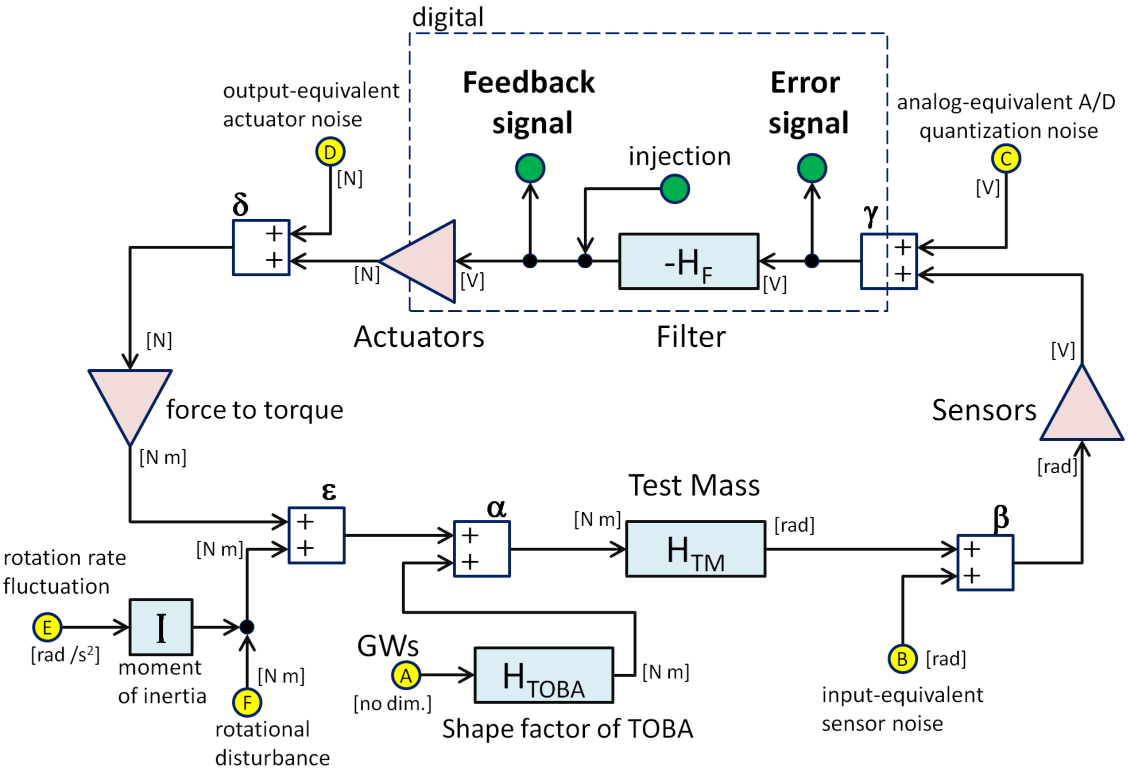

Figure 4.14: Block diagram of test mass control loop. Noises injected to the control loop are shown by yellow circles. Physical dimensions of the signals are also shown within brackets. The point of data acquision and signal injection are shown by green circles. The upper case letters in the circles indicate the noise injected into the control loop and the Greek letters indicate the residuals at the injection points.

The central control unit (CCU) is the heart of the satellite. The extended control unit (ECU) is a processing unit that is connected to the mission equipment and some advanced components of the bus system. It has an extended memory in which the data obtained from various mission components are stored. The communication link between the ECU and the CCU is called the Arcnet.

Attitude Stabilization

Attitude is a very important property in the control of satellites. This is mainly because a satellite can only generate sufficient energy to operate through its solar array when sunlight arrives from an appropriate direction. SDS-1 stabilizes itself using various types of attitude sensors and actuators. Magnetic sensor: magnetic sensors detect the Earth's magnetic field in orbit. Since the direction and intensity of the magnetic field are

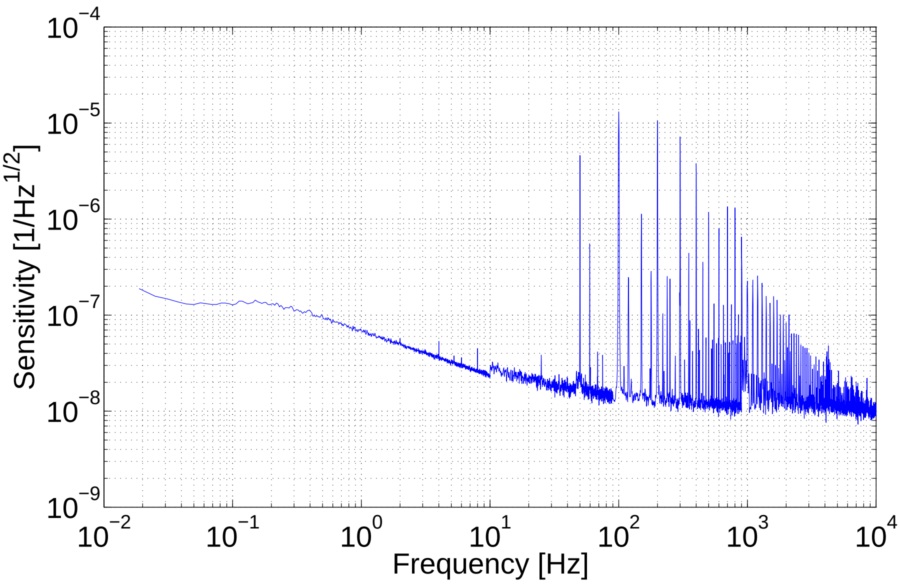

Figure 4.15: Design sensitivity of SWIM$_{\mu\nu}$.

Figure 4.16: Picture of the SDS-1 satellite. This photograph is taken at the time of the measurement of residual magnetic moment of the satellite.

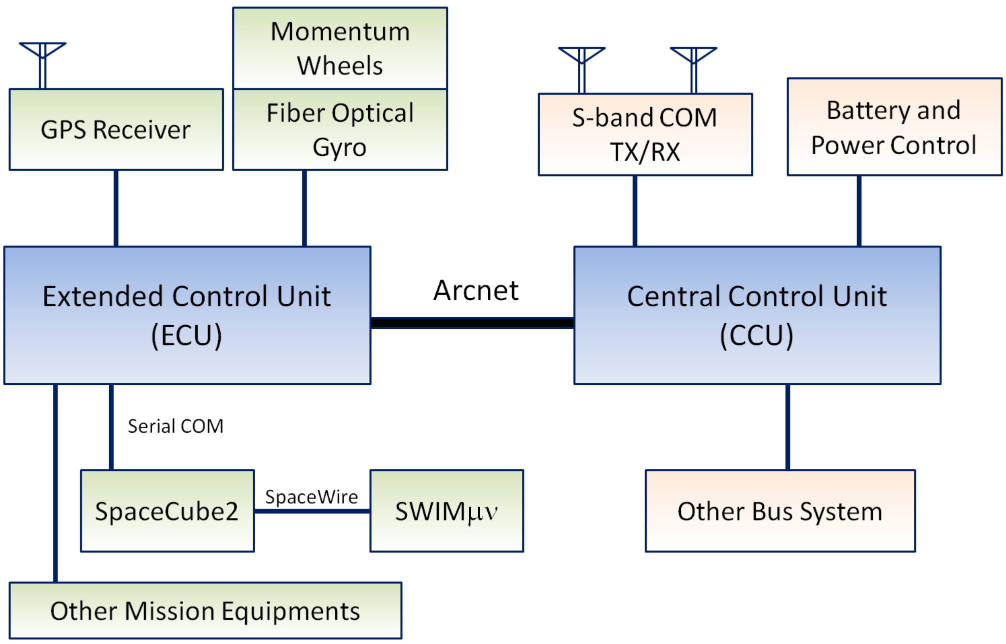

Figure 4.17: Functional block diagram of SDS-1 bus system. The two boxes in the center are the main control units of the satellite, the central control unit (CCU) and the extended control unit (ECU). The author devised this figure on the basis of [52].

known and relatively stable, the orientation of the satellite can be estimated. Coarse and fine sun sensor [55]: Another attitude sensor is a sun sensor. It measures the intensity of incoming light from the Sun. The sensor is fixed to the satellite, and the light intensity is dependent on the angle of the Sun and the satellite axes. Thus we can determine the solar angle of the satellite. It is also equipped with fiber optical gyros assembly (FOGA) which is a kind of inertial sensor. The principles of detection of a fiber optical gyro are based on the Sagnac effect [56].

Mission Equipment

All mission components on the satellite including SWIM$_{\mu\nu}$ are connected to the ECU. The mission time onboard SDS-1 is shared among all missions. On the other hand, vital systems for the satellite, such as the downlink communication system and the batteries, are connected to and controlled by the CCU.

Communication and Time Calibration System

The communication system is vital for a satellite as well as a power supply and thermal

Table 4.7: SDS-1 parameters, some of which are cited from [52].

Item	Description
Mass	$\sim$ 100 kg
Size	70 cm $\times$ 70 cm $\times$ 60 cm
Bus power	$\sim$ 100 W
Attitude control	Spin (nominal), 3-axis (optional)
RF communications	S-band ($\sim$ 2 GHz)
Link speed (Down)	3 kbps
Link speed (Up)	500 bps
Orbit	Sun-synchronous orbit
Inclination	$\sim$ 98 deg
Orbital period	$\sim$ 100 min
Averaged altitude	$\sim$ 670 km

control. The radio frequency used in the communication is S-band (from 2 to 4 GHz), which is widely used in amateur radio and telecommunications. In addition, the satellite has a small receiver of Global Positioning System (GPS). The signals sent to SpaceCube2 are utilized to calibrate its time stamp.

4.4.2 Launch and Orbit

SDS-1 was launched by the H-IIA vehicle on January 29, 2009 from Tanegashima Space Center. It was launched as a piggyback on a satellite for observing greenhouse gas named GOSAT, which has the nickname of "Ibuki". The picture of the launch is shown in Figure 4.18. Since GOSAT is an earth-observing satellite, it was put into sun-synchronous sub-recurrent orbit. This orbit is suitable for spacecrafts that observe the Earth's surface because the angle of sunlight to the Earth's surface is constant in every observation. The altitude and orbiting period of SDS-1 are about 670 km and 100 min, respectively.

4.5 Summary

The cost of spaceborne detectors is very high. However, the results provided by these spaceborne detectors are expected to be meaningful in GW astronomy. As a first step toward observation by spaceborne GW detectors, we developed a tiny spaceborne TOBA called SWIM$_{\mu\nu}$. The TOBA has a bar-shaped test mass made of aluminum with a mass

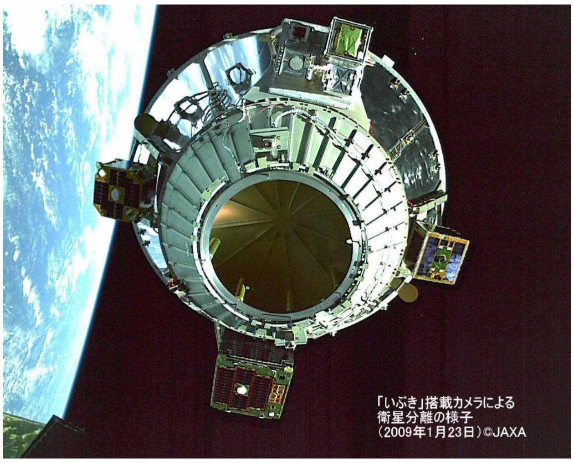

Figure 4.18: Picture of the launch of SDS-1. ©JAXA, under the terms of use of JAXA digital archives [57].

of 50 g. The rotational displacement of the test mass are read out by the photoreflective position sensors. The signal processed by the digital PID filter is fed back to the coil magnet actuators so that the test mass is supported at the correct position. The estimated sensitivity is $10^{-7}/\sqrt{\mathrm{Hz}}$ at 0.1 Hz. The satellite carrying SWIM$_{\mu\nu}$ is SDS-1 developed by JAXA, and it was successfully launched into sun-synchronous polar orbit on January 23, 2009.

Chapter 5

On-Orbit Experiments

SWIM$_{\mu\nu}$ was launched into orbit on January 23th, 2009. Its operation was conducted for about one and a half year. In this chapter, the following on-orbit experiments are described. First, the experimental operation of the SWIM$_{\mu\nu}$ detector is explained in detail. Next, the performance of the detector is analyzed. The noise spectral density and its limiting noise sources are studied. Finally, detector calibration is described.

5.1 Experimental Operations

5.1.1 Satellite Operations

The operation of SWIM$_{\mu\nu}$ started in February 2009. Because of the operational time of SDS-1 was shared with other instruments on the satellite, we were only able to send commands to SWIM$_{\mu\nu}$ on 2 to 5 days per month. We sent commands to SWIM$_{\mu\nu}$ while the SDS-1 satellite could be seen from the ground station, over a duration of 10 min. We refer to this communication session as a pass. By the end of the satellite operation, 43 passes had been conducted and approximately 20 MB of data had been collected. During these limited windows of opportunity, position control of the test mass, sensor calibration, clock synchronization to GPS time, and GW observation were completed. The satellite operation was terminated in September 2010.

Each pass is distinguished with a pass identification number (pass ID), which indicates the starting time of the pass in coordinated universal time (UTC). The pass IDs and the corresponding experiments are described in Table 5.1. Each pass ID contains the year, month, day, hour and minutes of the start time in UTC. The format is YYMMDD_HHmm, where YY, MM, DD, HH and mm denote the year, month, day, hour and minutes, re-

Table 5.1: Operations of the detector during individual passes of the satellite.

Pass ID	Experiment	Satellite Mode	Sampling Rate
091209_1451	Noise measurement	Spin-stabilized	134 Hz
091209_1830	Noise measurement	Spin-stabilized	537 Hz
100120_0236	Noise measurement	Three-axis stabilization	134 Hz
100121_0145	Noise measurement	Three-axis stabilization	2 Hz
100224_0409	Noise measurement	Three-axis stabilization	2 Hz
100225_0443	Noise measurement	Three-axis stabilization	134 Hz
100325_0337	Noise measurement	Spin-stabilized	16 Hz
100326_0408	Noise measurement	Spin-stabilized	2 Hz
100617_0800	GW observation No.1	Spin-stabilized	1 Hz
100715_0730	GW observation No.2	Spin-stabilized	1 Hz

spectively. In particular, the final operation, with the pass ID of 100715_0730, is the main observational run. We used the data obtained in this operation for the analysis.

First On-Orbit Lock Acquisition

In May 2009, we confirmed successful lock acquisition of the test mass position control. Figure 5.1 shows the z and yaw error signals. At the time is approximately 3 sec, vertical (z) control system was turned on. Then the rotational (yaw) control system was activated after the time is near 12 sec. Transient responses of the test mass of the two DoFs were clearly seen. Since the bandwidth of z control is higher than that of the yaw control, dumped oscillation was clearly observed in yaw error signal than that of z. The full success of the SWIM$_{\mu\nu}$ mission was achieved at this time, as we confirmed the successful lock acquisition on orbit.

5.1.2 Observational Runs

Observational runs were conducted twice, once in June and once in July 2010. The total observation time was more than 360 min, equivalent to more than three round trips around the Earth. We selected observation parameters to satisfy the following conditions. (i) The operational time was chosen to avoid the south Atlantic anomaly (SAA) when the detector was on. This is because the onboard computer used for SWIM$_{\mu\nu}$ shuts down when it is exposed to intense cosmic radiation. (ii) To realize the rotation of the TOBA, the length of the observational time was selected to be sufficiently long to record the spin of the satellite.

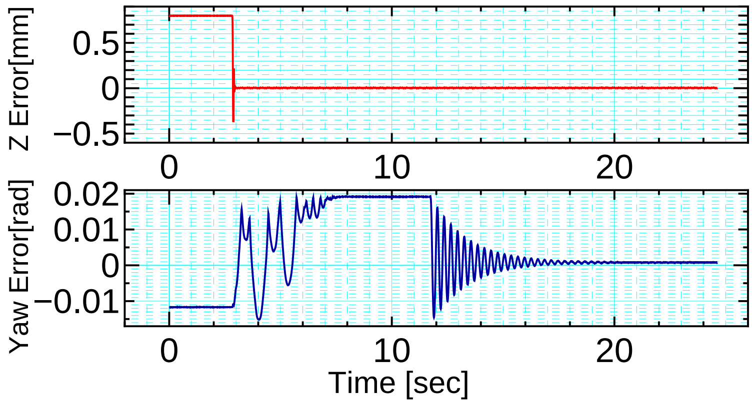

Figure 5.1: First lock acquisition of the test mass.

Table 5.2: Selected detector parameters for the observational run in July 2010.

Parameter	Value
Sampling rate	1.05 Hz
Length of observation time	240 minutes
Satellite mode	Spin stabilized (46.5 mHz rotation)
Detector orientation	To the Galactic center

The selected observational parameters are shown in Table 5.2. The sampling rate was chosen to be about 1 Hz, while the observation length was about 240 min. The orbit of the satellite during the observational run is plotted in Figure 5.2 as a two-dimensional plot and in Figure 5.3 as a three-dimensional plot. These curves were calculated by using the MATLAB library [58] to compute the orbit from the two-line elements (TLEs) provided by JAXA.

Detector Orientation

To conduct astronomical observations, the detector was oriented toward the Galactic center during the observational operation. Note that the natural local frame for the cosmic SGWB is the rest frame of cosmic microwave background (CMB). Figure 5.4 shows the relative direction of the dipole component of the CMB and the direction of the Galactic center. It can be seen that the angle between the two frames is about 93.7°, i.e., the two directions are almost perpendicular to each other. This is a suitable condition of analyzing the data from the detector oriented toward the Galactic center since the system is symmetric along the plane containing the test mass.

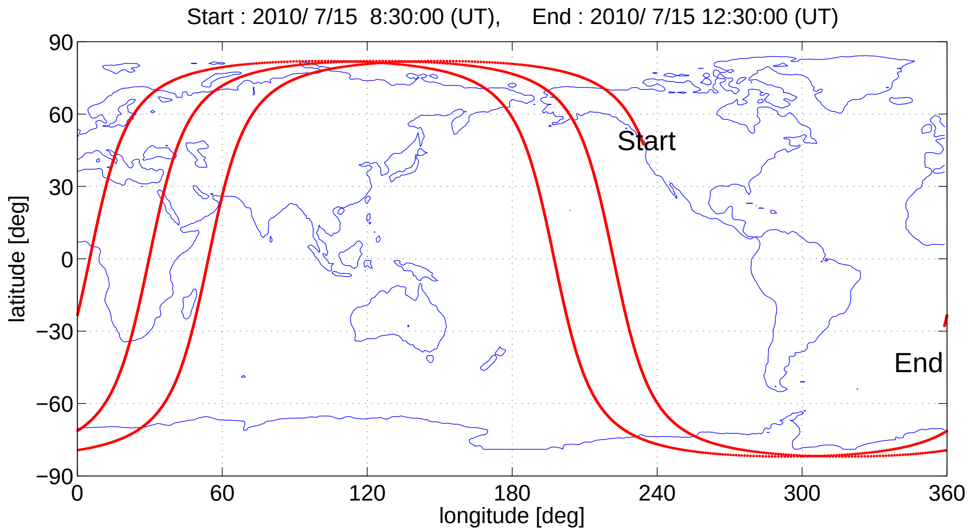

Figure 5.2: Orbit of observational run No.2 (July 2010) on a world map.

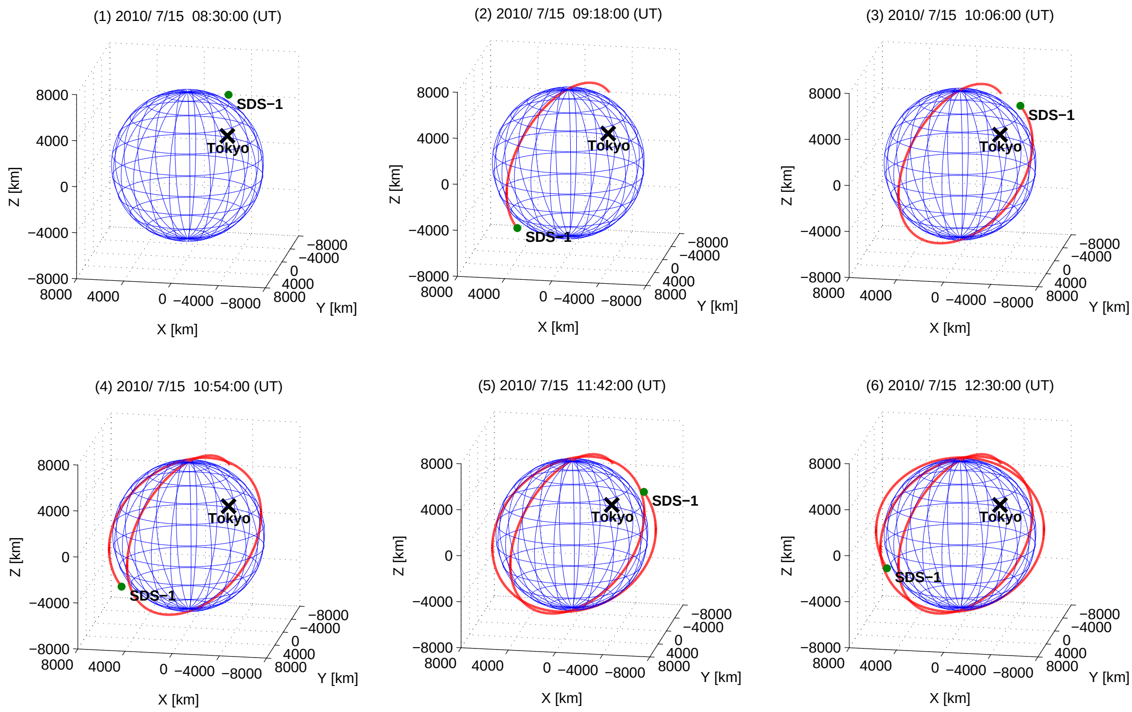

Figure 5.3: Three-dimensional view of the orbit during the observational run No.2 (July 2010) of SWIM$_{\mu\nu}$. The position of Tokyo is also plotted as a black cross.

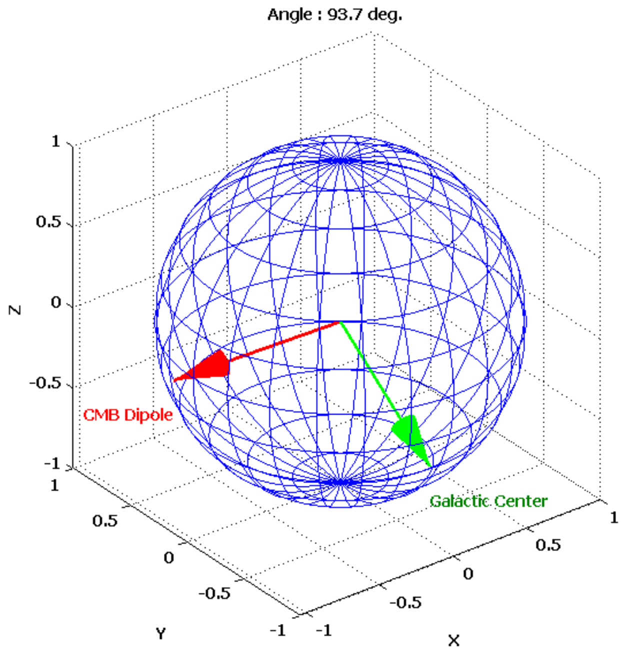

Figure 5.4: Directions of the dipole component of the CMB and the Galactic center. The two directions are shown in a unit sphere.

5.2 Detector Performance

5.2.1 Noise Level

The residual angular noise spectra of the detector are shown in Figure 5.5. These spectra correspond to the residual signal spectra at the point β in Figure 4.14. The plot is a combined graph of showing different measurements of the noise level of the detector in spin-stabilized mode. This is because we were able to obtain only a limited amount of data in each operation. However, the characteristics of the detector were invariant throughout the operation period of the satellite (about 1.5 years) since the consistency of the spectra can be seen in the plot. The only exception is in the frequency range of 10^{-1}—10^{0} Hz. The cause of this disagreement is the different quantization noise level of the digital data, which is the dominant noise level in the observational frequency. Details are discussed in the subsequent sections.

Noise Level in Observation Band

The angular displacement noise level of the detector in the observation frequency band

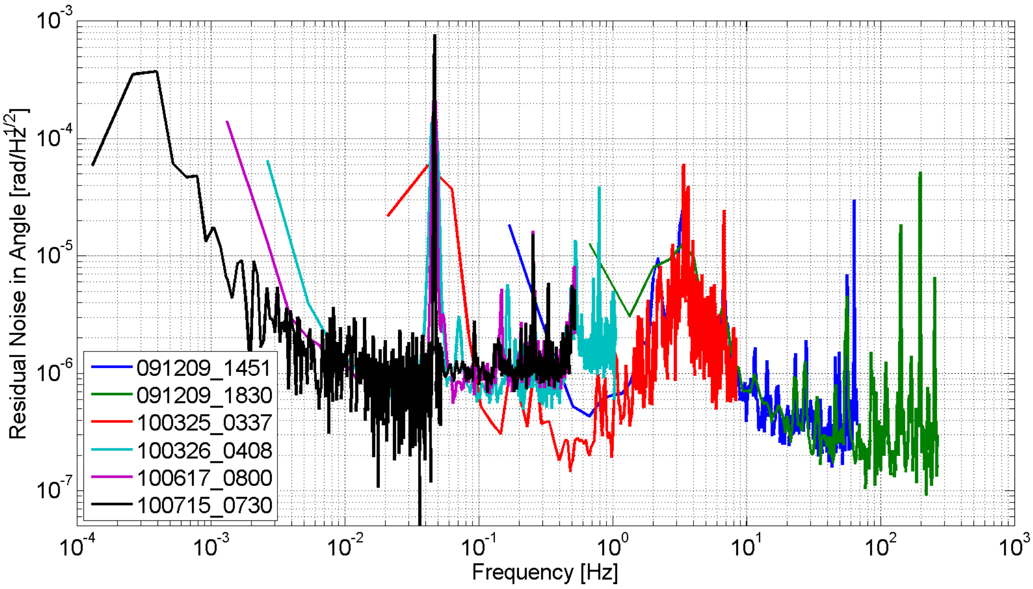

Figure 5.5: Residual angular noise spectra during spin-stabilized mode of the satellite. The residual angular noise spectra of six observational runs are plotted together.

is shown in Figure 5.6. This spectra correspond to the incoming noise spectrum at the point B in Figure 4.14. To distinguish line noises (if exists) in the observation band, the noise level is plotted using four different bandwidth; 0.13 mHz, 0.51 mHz, 2.04 mHz and 4.52 mHz. Note that the bandwidth used in the data analysis is 4.52 mHz. No structures of the level of the angular displacement noise in the observation frequencies is seen, and the spectrum has a flat shape. This is an excellent characteristic to be used for an search for SGWBs. In addition, twice the rotation frequency of the satellite, $2\omega_{\rm rot} = 93$ mHz, is also shown in the plot as a red line. It can be clearly found that there is a peak in the noise level at this frequency. This is because the peak induced by the geomagnetic effect (described later) at the rotation frequency, 46.5 mHz, has some extent of a harmonic distortion. No signal contamination from this peak in the observation frequency is seen.

5.2.2 Stability

Stability of Noise Level

One of the criterion of evaluating the detector performance is to check the stability of the detector. A spectrogram for the observational run is shown in Figure 5.7. The width of the time window and the frequency window are 67.2 sec and 16.4 mHz, respectively. These

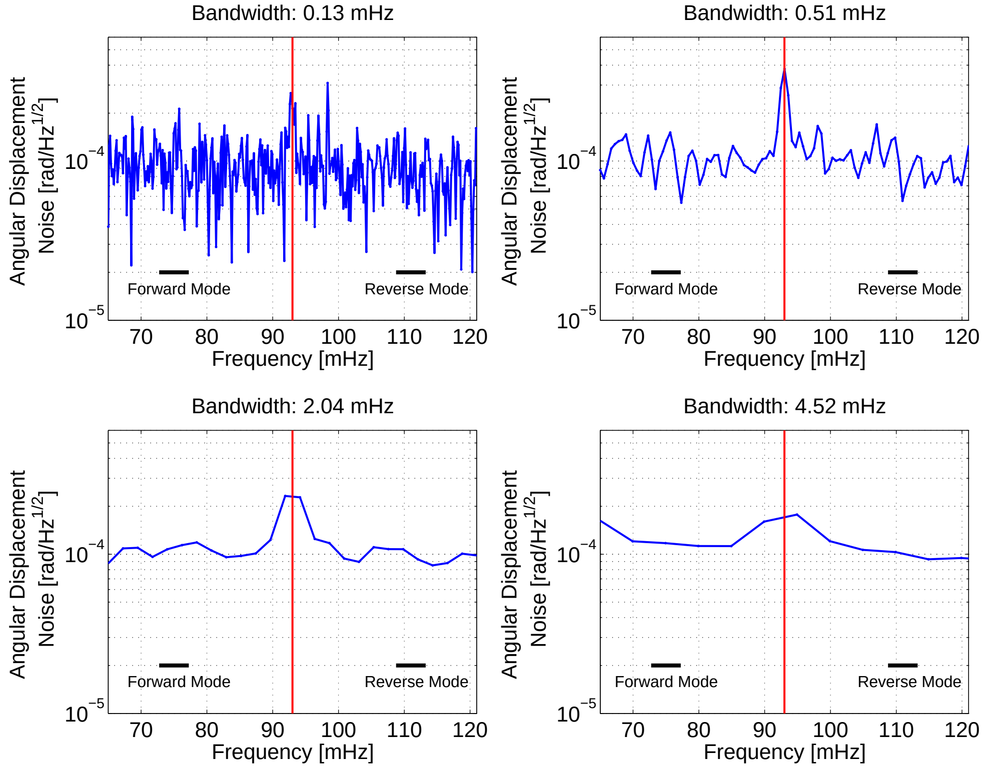

Figure 5.6: Angular displacement noise in the observation band. The observation frequency bands used for the analysis for the forward and reverse modes are shown by the black lines. Twice the rotation frequency, 93 mHz, are indicated by the red line in each plot.

parameters for the spectrogram is selected so that the structure in the figure is clearly seen. It is confirmed that the stability of the noise level is satisfactory in the frequency between 70 mHz and 115 mHz, which is used in the GW search.

Regions of high noise level can be found in frequencies of approximately 50 mHz, 250 mHz, and so on. These corresponds to the peaks of the noise level of 100715_0730, which shown as a black curve in Figure 5.5. Particularly, the red belt at frequency around 50 mHz corresponds to the narrow peak at the rotation frequency of the satellite. The variation in every 50 min, which is seen as a pulsation, can also be found. As described in Section 5.2.3, this is because the origin of this peak is the geomagnetic coupling and the strength of the geomagnetic field at the satellite position varies as the satellite orbits around the Earth.

Fluctuation of Rotation Rate of Satellite

As considered in Section 3.2.1, fluctuation of the rotation rate of the satellite can generate much uncertainty of the frequency-upconversion using the rotating TOBA. Thus, we examine the frequency of the rotation of the satellite. Figure 5.8 shows the level of the residual angular noise of the detector near the rotation frequency 46.5 mHz. There is a narrow and high peak at the rotation frequency induced by the satellite spin. The linewidth is approximately 2 mHz. At the same time, FOGA, which is a sensitive gyros, measured the rotation rate of the satellite during the observation. This range is shown as a band with green borders in Figure 5.8. The result of the measurement is that rotation frequency is between 46.57 and 46.66 mHz. The two results agree with each other. Considering that the measurement of the rotation rate by the FOGA is extremely precise, it is credible that the bandwidth of the fluctuation of the rotation rate is much smaller than the bandwidth of the observation, i.e.,

$$2\pi \times (\delta\omega_{\mathrm{rot}}) \sim 0.1 \text{ mHz} \ll 4.5 \text{ mHz} . \tag{5.1}$$

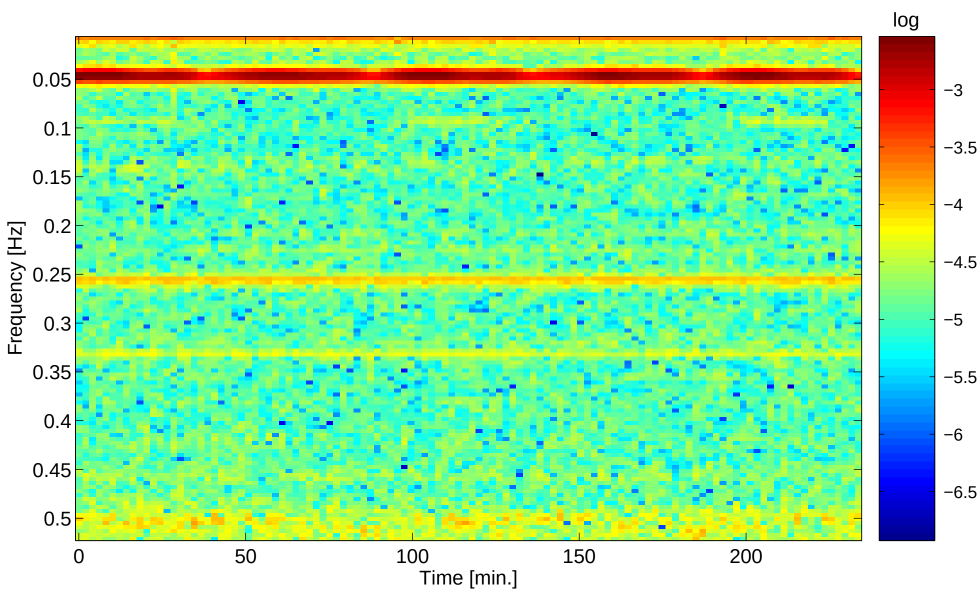

Figure 5.7: Spectrogram showing stability of the detector. The x axis is elapsed time from the start of the observation, and the y axis is frequency. The logarithm of the level of the angular displacement noise is shown and is classified by color.

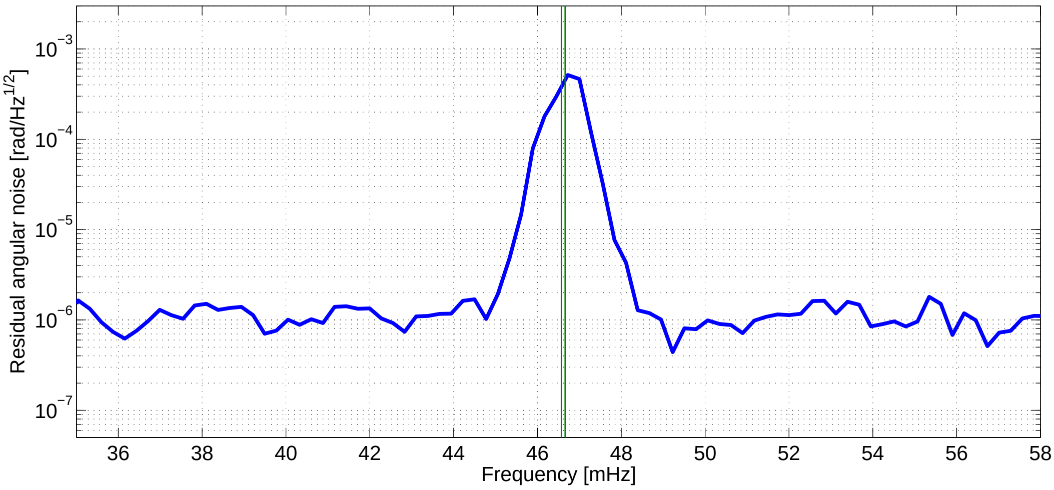

Figure 5.8: Residual angular noise of the detector near the frequency of rotation of the satellite. The measurement by using FOGA is also indicated as a band with borders shown as green lines.

5.2.3 Noise Analysis

Figure 5.9 shows the calibrated angular displacement noise level. This spectra correspond to the angular disturbance of the detector at the point B in Figure 4.14.

5.2.3.1 Geomagnetic Effect

The dominant effect in the lowest frequency range in Figure 5.9 is the geomagnetic effect. Specifically, the magnetic field of the Earth applies a force to the attached magnet used for the position actuator of the test mass. Since the satellite rotates around its center, the direction of the geomagnetic field varies in the satellite-fixed coordinates, and thus this external force oscillates about the frequency of the satellite spin. The narrow peak induced by this effect can be seen in Figure 5.9 at 46.5 mHz.

The direction and amplitude of the geomagnetic field depend on the position of the satellite. Therefore, the amplitude of the magnetic disturbance changes with the magnetic field. The geomagnetic field is calculated using the international geomagnetic reference field (IGRF-11) [59]. To verify that the peak at 46.5 mHz in the noise spectrum of the detector originates from the coupling between the satellite spin and the geomagnetic field, we compare the time variation of the amplitude of the peak with the satellite-spin perpendicular component of the geomagnetic field. The plot is shown in Figure 5.10. The two curves are in good agreement in the Figure 5.10. This means that the magnetic field

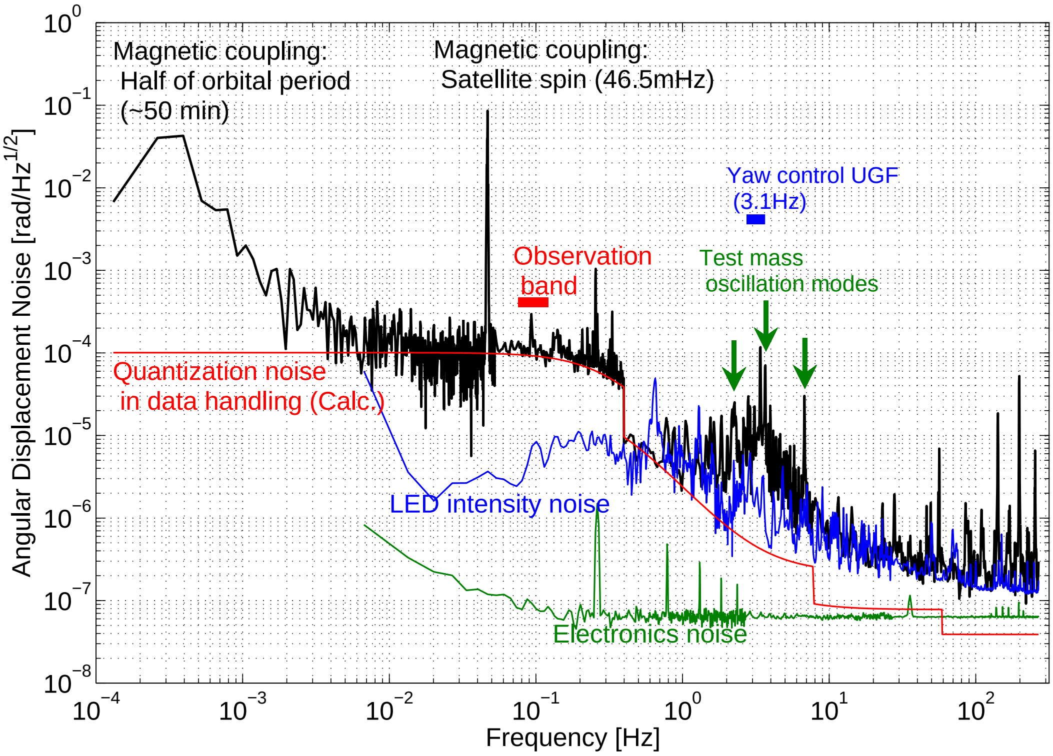

Figure 5.9: Total noise budget of the detector. The total noise level is shown as the black line. The red, blue and green curves show the quantization noise, the LED intensity noise and electronics noise, respectively. The frequencies of the oscillation modes of the test mass are indicated by the arrows. The frequency ranges of the observation band is also shown as the red line.

parallel to the attached magnets applies a force to the test mass. Note that the two zero levels of the curves in Figure 5.10 are aligned, so that the absolute values of the two data are compared.

5.2.3.2 Quantization Noise

The dominant noise in the observation band is the quantization noise. The origin of the quantization noise is based on the quantization errors in the averaging process in SpaceCube2. The principle is as same as that of the analog-to-digital (A/D) quantization noise. The spectral density of the A/D quantization noise, $S_{AD}(f)$, is known to be expressed as

$$[S_{\mathrm{AD}}(f)]^2 = 2\sigma^2 T_0 \left(\frac{\sin(\pi f T_0/2)}{\pi f T_0/2} \right)^2 . \tag{5.2}$$

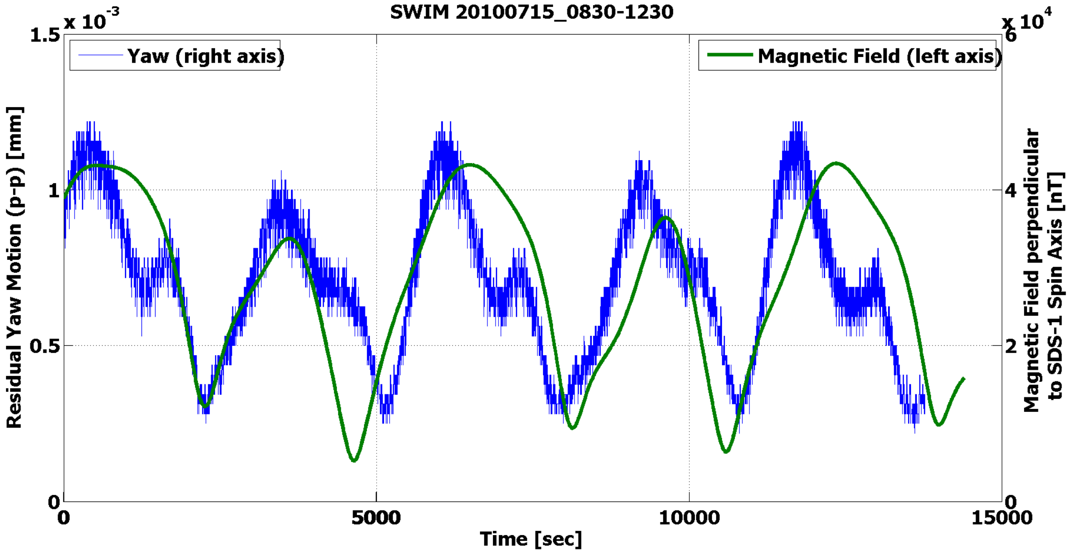

Figure 5.10: Satellite-spin perpendicular component of the geomagnetic field and the peak-to-peak amplitude of the angular motion at 46.5 mHz.

Here $T_0 = 1/f_s$ is the sampling time and σ is the standard deviation of the white A/D quantization error, which satisfies

$$\sigma = \sqrt{\frac{(\mathrm{LSB})^2}{12}} \;, \tag{5.3}$$

where LSB is the value of the least significant bit. In this case, we assumed that the quantization error has a flat distribution and that its absolute mean value is LSB/2. In our data acquisition setup, 16-bit numbers are used. Thus, LSB is calculated as

$$\mathrm{LSB} = 2^{-16} \times (\text{Full range of data acquisition}) = 6.25 \times 10^{-5}\ \mathrm{V}\ . \tag{5.4}$$

Note that this value is expressed in voltage-equivalent value.

The calculated noise spectrum for the data acquisition scheme used in the experiment is also plotted in Figure 5.9. Since the sampling rate was changed to reduce the amount of data according to the measurement frequency band, the noise curve has a discontinuity. In our observation band, i.e., around 90 mHz, the noise floor of the obtained data agrees with the calculated A/D noise level. The flat shape of the noise spectrum also shows that the sensitivity of the detector was limited by the data quantization noise, which has white spectrum.

5.2.3.3 Coupling between Datalink and LED Intensity

The noise spectrum above 0.8 Hz is limited by electric coupling between the datalink access via Spacewire and the intensity of LED in the photoreflective position sensor. The origin of this noise is identified in the following way. The noise peak above 0.8 Hz is seen as pulses of the signal in the time domain. Thus, the dependence of the pulse height on the data channel is examined. The relation between the mean value of the signals and the height of the pulses is shown in Figure 5.11. Although almost of the data channels have the pulses at the same timing, all the six main displacement signals of the photoreflective sensors and the six LED intensity monitor signals have the same linear dependence. In contrast, the signals of the accelerometer are not in the line. This fact implies that the origin of the pulse is in the photoreflective sensors. Then, the two possibilities of the origin are: (i) the fluctuation of preamplifier on the sensors and (ii) the fluctuation of the LED intensity. The case of preamplifier is rejected because the pulses would be eliminated by subtraction process conducted by the FPGA. Thus, the LED intensity is identified as the origin of the pulses.

Figure 5.12 shows the LED intensity noise measured in the ground test. This spectra correspond to the output voltage noise of the sensors, which can be converted the input-equivalent noise shown as the point B in Figure 4.14 by dividing sensor efficiency. Examining the signals in the time domain, the signals from the photoreflective sensors fluctuate at the same timing as data accesses via SpaceWire. The blue curve plotted in Figure 5.12 is the simulated noise spectrum of the electric coupling, which is a rectangular signal synchronizing the datalink access. Another curve shows the estimated LED intensity noise without the coupling. This spectrum was calculated by subtracting this datalink-induced pulses from the measured LED intensity signal in the time domain and converted to the frequency domain. We confirmed that the boundary between the two noise sources is about 50 Hz.

This electric coupling should be avoided in more sophisticated instruments. However, the main mission of SWIM$_{\mu\nu}$ was to demonstrate key technologies for future space missions. The criteria of full success of the mission was defined as the successful operation of the feedback system. Thus, the optimization and noise reduction of the electrical components were not considered to be important. These issues should be considered properly in the future GW detector missions.

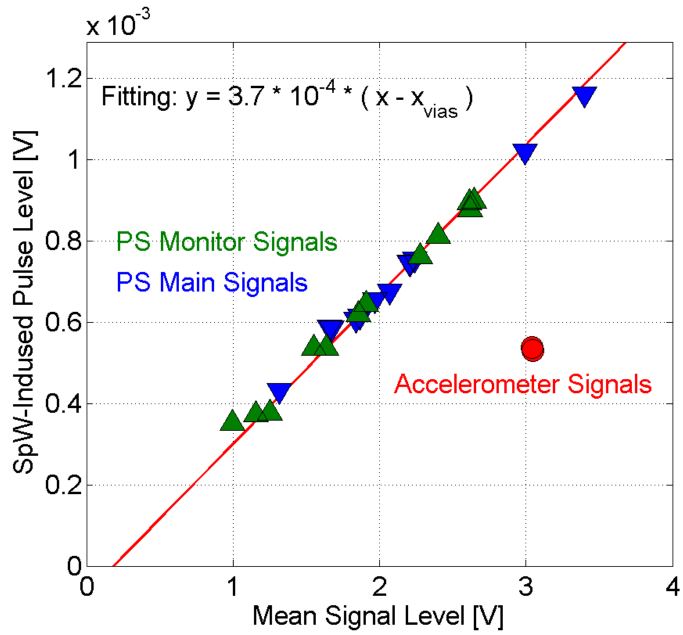

Figure 5.11: Datalink-induced pulse level in each data channel.

5.2.4 Behavior of Test Mass

Some interesting behavior was observed in the magnetic suspension system of the test mass. One example is the Foucault's pendulum formed by the test mass. The test mass is supported by magnetic forces and it oscillates around its center at start of feedback control. Since the satellite spins around its principal axis, the test mass in the local detector coordinates acts as a Foucault's pendulum.

This phenomenon was confirmed using the data obtained at the time of lock acquisition. In particular, when the test mass are detached from the side of the movable scope at the lock acquisition, the test mass starts to oscillate around its equilibrium position. The oscillation is regarded as a swing of a two-dimensional pendulum in the x-y plane. The free oscillation of the test mass has a large Q-value, and damping of the oscillation takes several minutes. During the oscillation, the direction of the oscillation rotates at the frequency of the rotation of the satellite. This is because the test mass acts as a Foucault's pendulum in the satellite.

Another phenomenon called Y drift was also observed in the operation of 100326_0408. This is the effect of the centrifugal force induced by the satellite spin. Figure 5.13 show the data corresponding to this phenomenon. The onboard MEMS gyroscopes as a EM sensor detected the spin-up of the satellite, which was performed by the satellite attitude

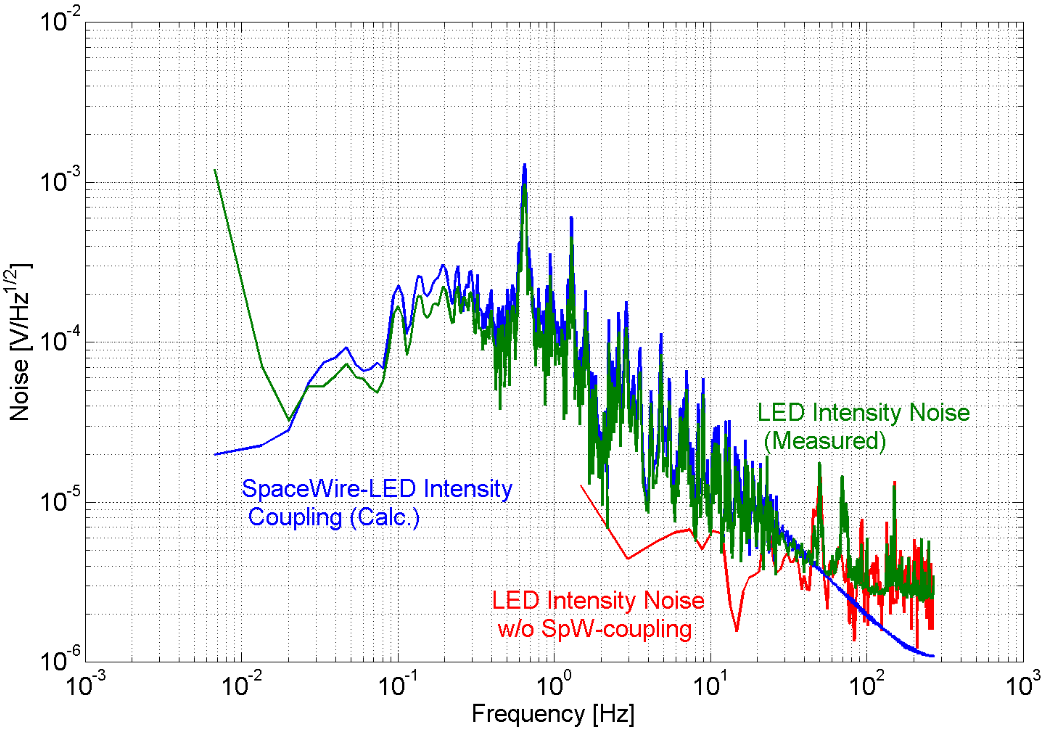

Figure 5.12: Contribution of datalink-induced electric coupling noise to the LED intensity noise. The measured level of the LED intensity noise is shown by green line. The simulated noise level of the coupling between LED intensity and the datalink is shown by the blue line. The red line shows the LED intensity noise from which the coupling is subtracted.

control system as shown in Figure 5.13. At the same time, the equilibrium position of the test mass drifted in the y direction. This behavior can be interpreted as the increase in the centrifugal force induced by the satellite spin corresponding to the spin-up. It is interesting that the attitude of a small satellite was detected by the GW detector. This phenomenon can be used to estimate the spring constant of the suspension system; however, more comprehensive and accurately calibrated data should be used.

5.3 Detector Calibration

5.3.1 Calibration System

The most difficult experimental procedure of SWIM$_{\mu\nu}$ was the calibration of the detector, i.e., the measurement of the open-loop transfer function of the feedback control

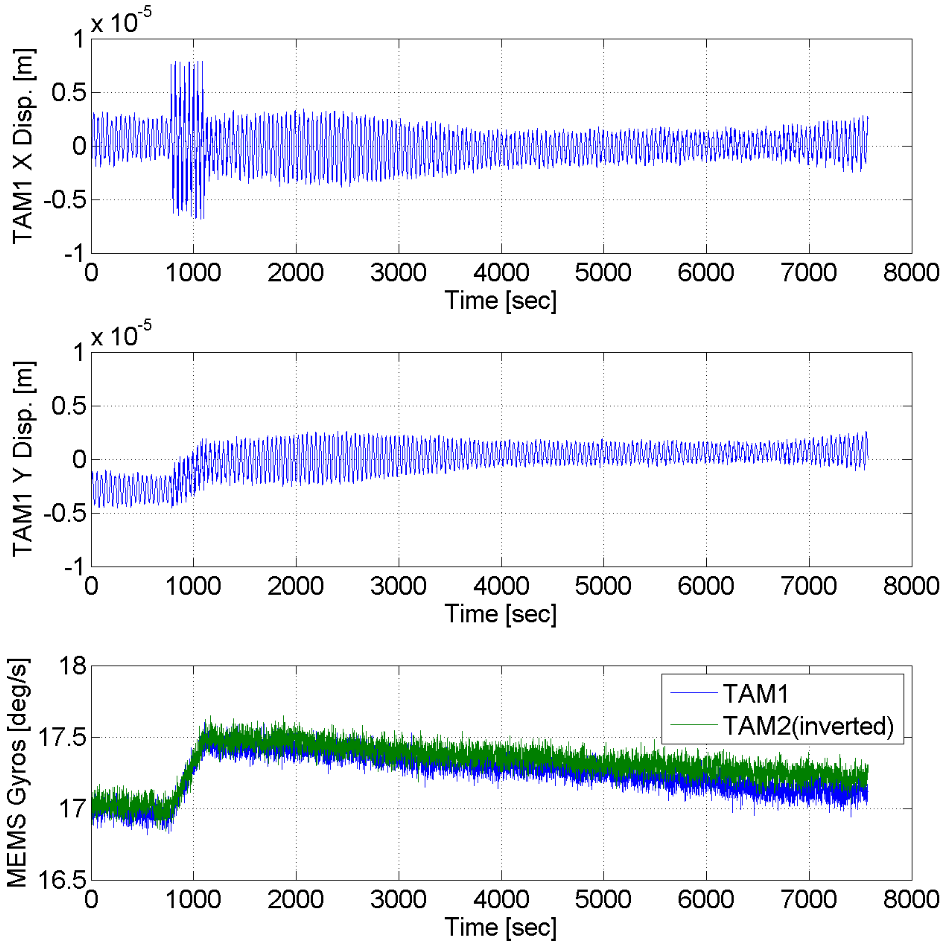

Figure 5.13: Drift of the test mass corresponding spin speed variation of the satellite.

system. This is because we had limited opportunity to operate the detector and were able to access only a small amount of data. As a result, we conducted the calibration process in the following way. (i) The open-loop transfer function of the servo was measured at two different frequencies above the resonant frequency of the suspension system of the test mass. (ii) The DC level of the open-loop transfer function was measured by injecting rectangular pulse into the feedback control loop. (iii) The measured data were fit to a simple mechanical suspension model of the test mass to estimate the open-loop transfer function of the whole feedback system.

The simplified schematic diagram of the feedback control loop is shown in Figure 5.14.

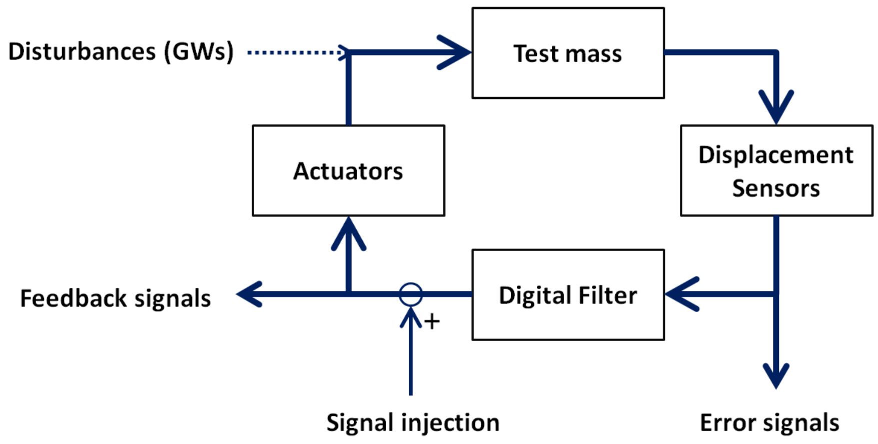

Figure 5.14: Simplified schematic diagram of the feedback control system of the test mass and setup for transfer function measurment. The arrows shows the flow of the signals.

Here, the open-loop transfer function of the feedback system G is expressed as

$$G = H_{\mathrm{TM}} H_{\mathrm{S}} H_{\mathrm{F}} H_{\mathrm{A}} \ , \tag{5.5}$$

where H_{TM}, H_{S}, H_{F} and H_{A} are the transfer function of the test mass, the displacement sensor, the digital filter and the actuators, respectively. Since the detector is operated at the low-frequency, thus, the transfer functions of the systems except that of the test mass can be approximated as flat responses as described in Chapter 4.

Transfer Function of Sensors, Filter and Actuators

The transfer function of the displacement sensors is expressed as

$$H_{\mathrm{S}} = A_{\mathrm{r}} A_{\mathrm{d}} \ , \tag{5.6}$$

where A_{r} is the rotation factor, i.e., the factor of the displacement of the sensing point when the test mass rotates. In this case, $A_{\mathrm{r}} = 0.02$ m/rad. The factor A_{d} is a displacement sensitivity of the photoreflective sensors. As shown in Figure 4.9, $A_{\mathrm{r}} = 10^3$ V/m. Thus, the response of the displacement sensor is calculated as

$$H_{\mathrm{S}} = 20 \ \mathrm{V/rad} \ . \tag{5.7}$$

The transfer function of the actuator is expressed as follows;

$$H_{\mathrm{A}} = A_{\mathrm{cd}} A_{\mathrm{c}} A_{\mathrm{tq}} \ . \tag{5.8}$$

Here A_{cd}, A_{c} and A_{tq} is the efficiency of the coil driver, the coil-magnet actuator and factor from the force to the torque. A_{cd} is designed as 4.9×10^{-2} A/V, and $A_{\mathrm{c}} = 0.16$ N/A as shown in Figure 4.11. A_{tq} is determined by the shape of the test mass as 2×10^{-2} N m/N. Thus, the response of the actuators are calculated as

$$H_{\mathrm{A}} = 1.6 \times 10^{-4} \text{ N m/V} . \tag{5.9}$$

The frequency dependence of the transfer function of the digital filter is shown in Figure 4.12. As seen in the figure, it is apparent that the transfer function of the filter can be regarded as a flat response below the cutoff frequency, 10 Hz. Note that the observation band is approximately 0.1 Hz and this is sufficiently lower than the cutoff frequency. In particular, the filter gain for the *yaw* DoF control is estimated as

$$H_{\mathrm{F}} = 1 \text{ V/V} . \tag{5.10}$$

Transfer Function of Test Mass

The most difficult transfer function to be estimated is that of the test mass. In an ordinary ground-based experiment, the transfer function of the test mass is calculated back by using the measured value of the total open-loop transfer function and all of the other component in the feedback loop. Here we assume that the transfer function of the test mass is a simple, the first-order low-pass function as that of a single pendulum, i.e.,

$$H_{\mathrm{TM}}(\omega) = \left(-I\omega^2 - k\right)^{-1} , \tag{5.11}$$

where I is the moment of inertia of the test mass and k is the rotational spring constant.

5.3.2 Measurement and Result

The measurement operation was conducted from March to November 2009.

5.3.2.1 Transfer Function in High-frequency

The measurement setup is described in Figure 5.14. The signal injection system is installed in the FPGA. This system can generate a rectangular wave at the frequency of 8 Hz, 16 Hz, 32 Hz and 64 Hz. The openloop transfer function can be measured by using the two signal; the error signal and the feedback signal. This is the same way as a measurement by a commercial servo analyzer.

The results are shown in Figure 5.15 and 5.16 for the *yaw* and z DoFs, respectively. The signal injection was conducted using the signal at the frequency of 8 Hz, thus the transfer function at 8 Hz and the odd-order harmonics can be measured. For the reference, the transfer functions which are measured at the ground test are plotted together. In the ground test, a strong Nd-magnets was attached outside the TAM to assist the magnetic force of the actuator, since there was a gravity on the ground. Although the difference in the condition, the two measured transfer functions are in fine agreement, i.e., the measurement of open-loop transfer function of high frequency region was in good agreement with the expected result in the ground. For the *yaw* DoF, the transfer functions are measured at the two frequencies. By fitting the data with a f^{-2} dependence function, the unity gain frequency (UGF) of the *yaw* DoF is estimated as 3.1 Hz, i.e., the openloop transfer function in high frequency can be regarded as

$$G(f) = \left(\frac{f}{3.1\ \mathrm{Hz}}\right)^{-2} . \tag{5.12}$$

This UGF is indicated in Figure 5.9 for reference. In contrast, for the z DoF, the UGF was above the measurement frequency; the UGF was approximately 60 Hz. This results are in good agreement with the transient response observed in the lock acquisition, which is shown in Figure 5.1.

5.3.2.2 Transfer Function in Low-frequency

The low-frequency level, i.e., the DC level of the transfer function of the servo was measured as follows. The DC offset was injected into the feedback system using the FPGA. We estimated the DC gain of the servo using the offset drift of the error signal and the feedback signal of the servo. In particular, the DC level is measured as follows. When the offset signal is injected into the feedback system and sufficient longer time than the response time of the system is passed, the DC gain of the system G_{DC} is expressed as

$$G_{\mathrm{DC}} = \frac{d_{\mathrm{er}} H_{\mathrm{F}}}{d_{\mathrm{FB}}} , \tag{5.13}$$

where d_{er} and d_{FB} are the offset drift of the error signal and the feedback signal, respectively. When the feedback system is operating correctly,

$$d_{\mathrm{FB}} = d_{\mathrm{er}} H_{\mathrm{F}} + a_{\mathrm{sig}} , \tag{5.14}$$

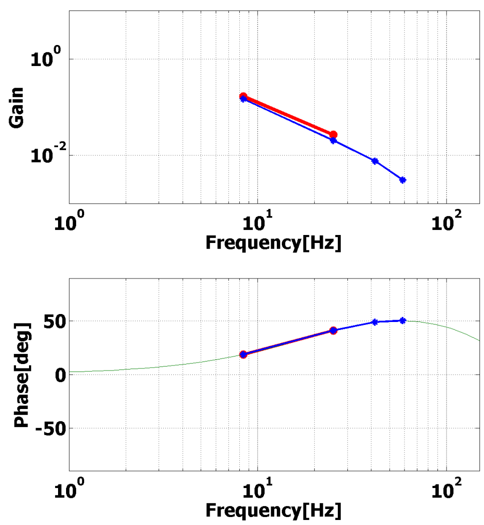

Figure 5.15: Measurement of the open-loop transfer function of *yaw* DoF in high frequency. The results are shown by the red circles. For reference, the results of the ground test are plotted together.

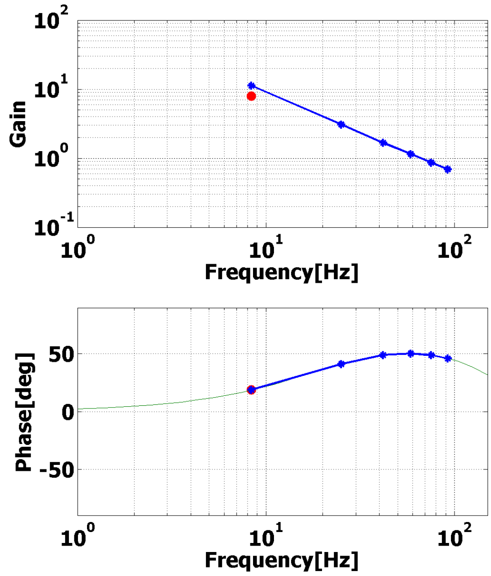

Figure 5.16: Measurement of the open-loop transfer function of z DoF in high frequency. The results are shown by the red circles. For reference, the results of the ground test are plotted together.

where $a_{\rm sig}$ is the amplitude of the injected signal. Thus, we estimate $G_{\rm DC}$ as

$$G_{\rm DC} = \frac{d_{\rm er} H_{\rm F}}{d_{\rm er} H_{\rm F} + a_{\rm sig}} \ . \tag{5.15}$$

The advantage of using this relation is that we do not need to know the value of $d_{\rm FB}$, which is difficult to be measured. Figures 5.17 and 5.18 show the measurement sequence for the z- and *yaw* servos, respectively. As seen in these figures, the S/N ratios in the feedback signals are low.

Fitting the signals in Figure 5.17, $d_{\rm er}$ is estimated to be

$$d_{\rm er} = -0.2583 \text{ V} \ . \tag{5.16}$$

Considering the fitting accuracy, the estimation error of $d_{\rm er}$ is assumed to be within ~ 0.001. Here, the DC gain of the filter $H_{\rm F}$ and the injected signal level $a_{\rm sig}$ are exactly 1 and 0.256, respectively. This is because these two signals are generated in the digital system. Thus, $G_{\rm DC}$ is estimated as

$$G_{\rm DC} = \frac{0.2583}{0.0023} \simeq 113 \ . \tag{5.17}$$

Applying the estimation error of $d_{\rm er}$ to 0.001, $G_{\rm DC}$ can be calculated as

$$G_{\rm DC} = \frac{0.2583}{0.0023 \pm 0.001} \simeq 113^{+86}_{-35} \ . \tag{5.18}$$

Thus, the systematic error of the DC gain of the openloop transfer function is approximately 80%.

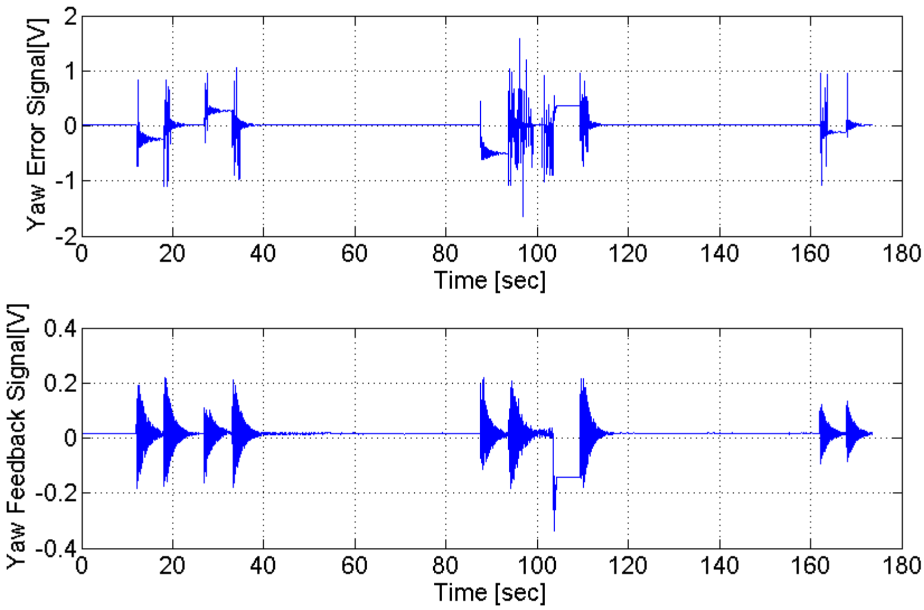

Figure 5.17: Signal injection for calibration of *yaw* control loop.

5.3.2.3 Fitting and Estimation of Openloop Transfer Function

As described in the previous section, the data were fit to a simple mechanical model in which the test mass suspension was modeled as

$$H_{\rm TM}(\omega) \propto \left(I\omega^2 + k\right)^{-1} \tag{5.19}$$

$$\propto \left(\omega^2 + \omega_0^2\right)^{-1} \ , \tag{5.20}$$

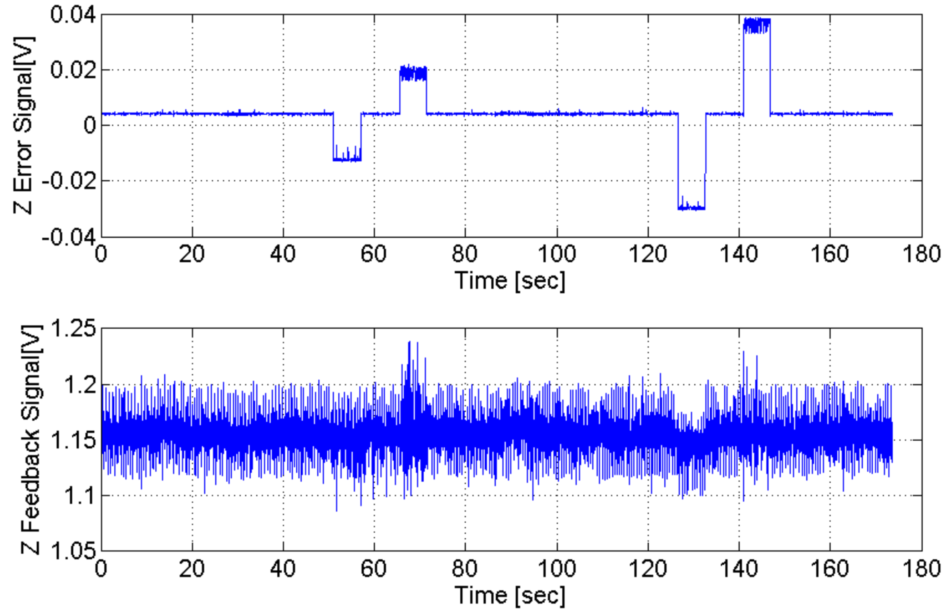

Figure 5.18: Signal injection for calibration of z control loop.

where k is the spring constant of the magnetic potential for the rotational DoF, which supports the test mass. Here we assume an anti-spring and sufficiently low Q-value. Thus, the openloop transfer function G has also low-pass frequency dependence:

$$G(f) = H_{\mathrm{TM}}(f) H_{\mathrm{S}} H_{\mathrm{F}} H_{\mathrm{A}} \tag{5.21}$$

$$\propto \left(f^2 + f_0^2\right)^{-1} \ . \tag{5.22}$$

By using the estimated values (5.12) and (5.17), the cutoff frequency f_0 is calculated as

$$f_0 \simeq 0.3 \text{ Hz} \ . \tag{5.23}$$

Note that the signal frequency used in the analysis is 0.1 Hz, which is lower than this cutoff frequency. In an ordinary GW detector, the signal frequency should be much higher than the resonant frequency, which determines the cutoff frequency of the openloop transfer function. This is because the test mass do not act as a free mass to the incoming GWs below this frequency. In our detector, we have to use 0.1 Hz as the signal frequency since the rotation frequency of the satellite is fixed. Although the detector still have the sensitivity to GWs in such a low frequency, the sensitivity deteriorates significantly.

5.3.3 Sensitivity to GWs

Using the results of the detector calibration, we can calculate the sensitivity of SWIM$_{\mu\nu}$ to GWs. The sensitivity is plotted in Figure 5.19. Sensitivities to the Forward mode and the Reverse mode with the frequency-upconversion are also plotted by applying the relation (3.52). These spectra correspond to the GW-induced disturbances at the point A in Figure 4.14. The sensitivity of the detector around twice the rotation frequency, 93.5 mHz, is approximately 1×10^{-2} $/\sqrt{\text{Hz}}$. Since the sensitivity curve has frequency dependence of nearly f^{-2}, the sensitivities to the upconverted GWs are not better than the sensitivity of the static TOBA. In particular, the sensitivity to the Forward mode and the Reverse mode at 18 mHz are approximately 1×10^{0} $/\sqrt{\text{Hz}}$ and 5×10^{-1} $/\sqrt{\text{Hz}}$, respectively.

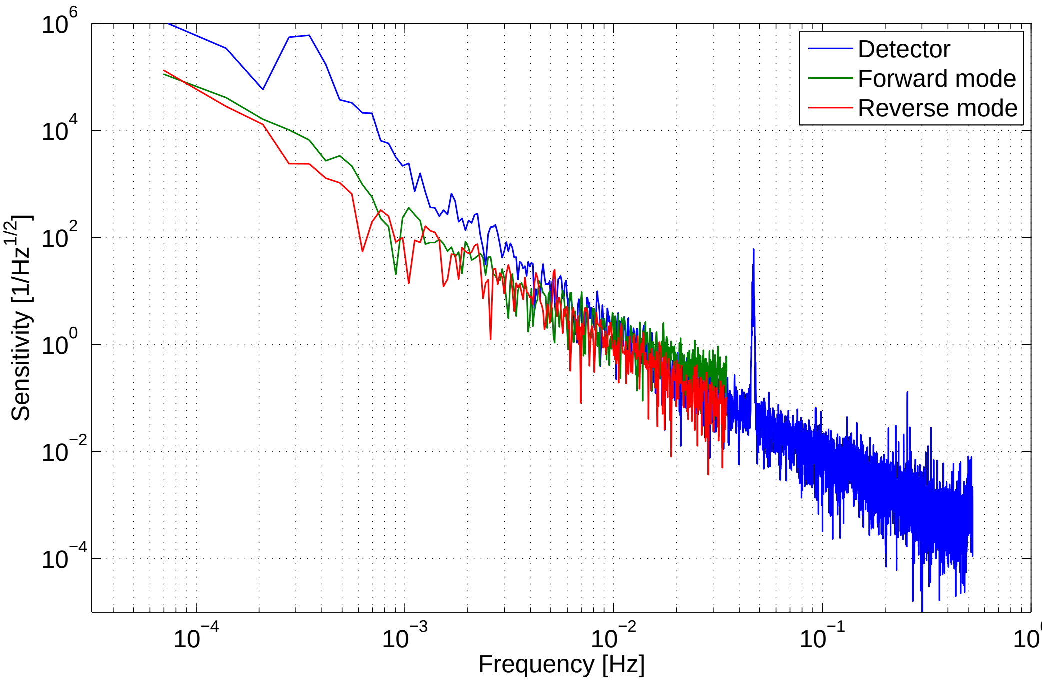

Figure 5.19: Detector sensitivity to GWs. The sensitivities with the frequency-upconversion technique are also shown.

Difference between Design and Obtained Sensitivity Curves

The difference between the design sensitivity of the detector 1×10^{-7} $/\sqrt{\text{Hz}}$, and the obtained sensitivity 1×10^{-2} $/\sqrt{\text{Hz}}$ is approximately 10^{5}. The reason why there is the large discrepancy can be explained with a correspondence to the assumptions in the estimation of the design sensitivity described in Subsection 4.3.7. The following two factors account for the deterioration in the sensitivity by 10^{5}.

- The most significant factor is the rotational resonant frequency f_0. In the calculation of the design sensitivity, f_0 was assumed to be much lower than the signal frequency, i.e., $f_0 \ll 0.1$ Hz. However, f_0 is approximately 0.3 Hz in reality, and thus deterioration factor by this effect is approximately $G_{\mathrm{DC}} H_{\mathrm{TOBA}}^{-1} H_{\mathrm{TM}}^{-1} \sim 10^4$.

- The quantization noise also deteriorates the sensitivity. The sampling rate in the observation run was 1.05 Hz. Thus, the quantization noise level is worsen by $\sqrt{537.11/1.05} \sim 23$. The original quantization noise is less than the that of the displacement sensors by factor of two, thus, deterioration in total is ~ 10.

Systematic Error

It was not possible to estimate the systematic errors of the onboard GW detector properly, owing to the lack of procedures to evaluate the various components of uncertainty. Thus, we consider only the major origins of systematic errors and take the conservative evaluation. The factor that has most large systematic errors in the calibration is the DC gain of the openloop transfer function, G_{DC}. The errors is approximately 80% as shown above. We considered that the second largest factor is the calibration factor of the photoreflective displacement sensors. The errors is presumed to be within 30%. The sum of the two errors are within 120%, and thus, we adopt a conservative estimate of 200% for the total systematic error in the detector sensitivity. This systematic error is used to set the conservative upper limit of the SGWB in our analysis described later.

5.4 Summary

SWIM$_{\mu\nu}$ was successfully launched into orbit, and operations were carried out from February 2009 to September 2010. The check-out operation, the confirmation of test mass position control, measurement of the noise level and calibration were conducted in this operational phase. The noise sources limiting the sensitivity of the detector were studied. The dominant noise source in the observation frequency band, i.e., around 90 mHz was the quantization noise in the data handling system. Besides, the magnetic coupling between the test mass and the magnetic field of the Earth was observed. The intensity fluctuation of the LEDs in the photoreflective sensors were also confirmed.

Observational runs were carried out in June and July 2010. SWIM$_{\mu\nu}$ was used for observation during three orbits of the satellite (about 300 min). The satellite was spinning when SWIM$_{\mu\nu}$ was in operation so that SWIM$_{\mu\nu}$ acted as a rotating TOBA. During the observation, the satellite stabilized its attitude using its spin of 46.5 mHz. The axis of the spin was directed to the center of our galaxy. The sensitivity of the detector around twice the rotation frequency, 93.5 mHz, was approximately 1×10^{-2} $/\sqrt{\mathrm{Hz}}$.

Chapter 6

Data Errors

Three types of data errors occurred in the data handling framework of SWIM$_{\mu\nu}$. The errors were caused by a bug in the control software in SpaceCube2 and the downlink communication from SDS-1 to the ground station. Because of the errors, the data obtained from the detector were too dirty to be used. We cannot use such data in the search for GWs without error correction.

In this chapter, we present the following. First, an overview of the data handling scheme of the detector is given. Next, the processes corresponding to the three types of errors, that is, packet loss, bit flipping and a software bug, are explained. Details of the correction process are described in Appendix A.

6.1 Overview

To deal with the data errors, we applied three restoration processes. The processes were applied sequentially to the raw data from the satellite. We found that several bit errors remained in the processed data. However, we also confirmed that errors did not affect the noise level of the instruments. Therefore, the data after error correction were sufficiently clean to be used to search for GWs.

It is extremely important to explain the validity of the data error correction process in detail. This is because the raw data were modified with specific criteria, not by a calibration process or data analysis, for which there are established methods. In particular, several data packets were checked visually for errors and corrected manually. Although this type of modification of raw data may be unsuitable for scientific research, it is vital for conducting data analysis when there is limited opportunity to access the satellite system.

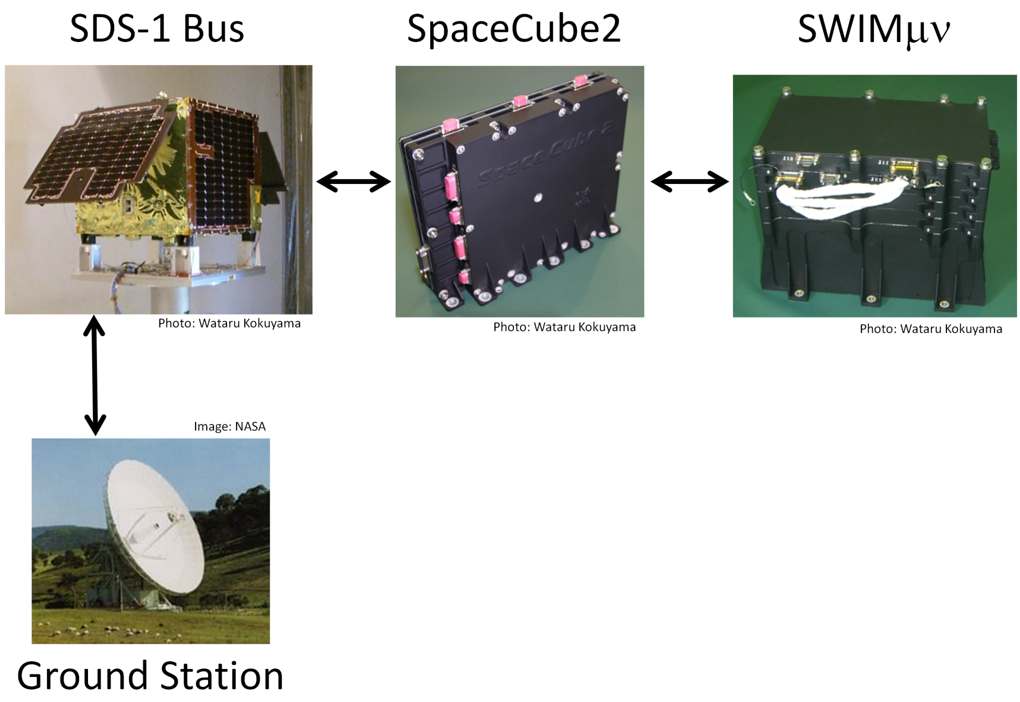

Figure 6.1: Overall view of the data-handling framework of SWIM$_{\mu\nu}$.

6.1.1 Data Handling Framework

Figure 6.1 shows the connections between components involved in data-handling framework. SWIM$_{\mu\nu}$ is connected to SpaceCube2 by SpaceWire and the data generated by the detector is transferred to SpaceCube2. Communication between SpaceCube2 and the SDS-1 bus system, particularly the ECU, is refered to as serial communication. Although serial communication is a general term, in this thesis we call the link *serial COM*. Experimental data and the status information of SDS-1 are downloaded via a radio-frequency communication, referred to as a downlink.

Data Flow

Figure 6.2 shows the data flow of the experiment in more detail. The error signals from the TOBAs are filtered and fed back by the the digital PID filter implemented in the FPGA. Signals extracted from the feedback control loop and EM signals are packeted by the FPGA. The packets are send to a first-in-first-out (FIFO) buffer in the static random access memory (SRAM) on the digital board in SWIM$_{\mu\nu}$. The onboard software on SpaceCube2 accesses the FIFO buffer via SpaceWire. The transferred data packets

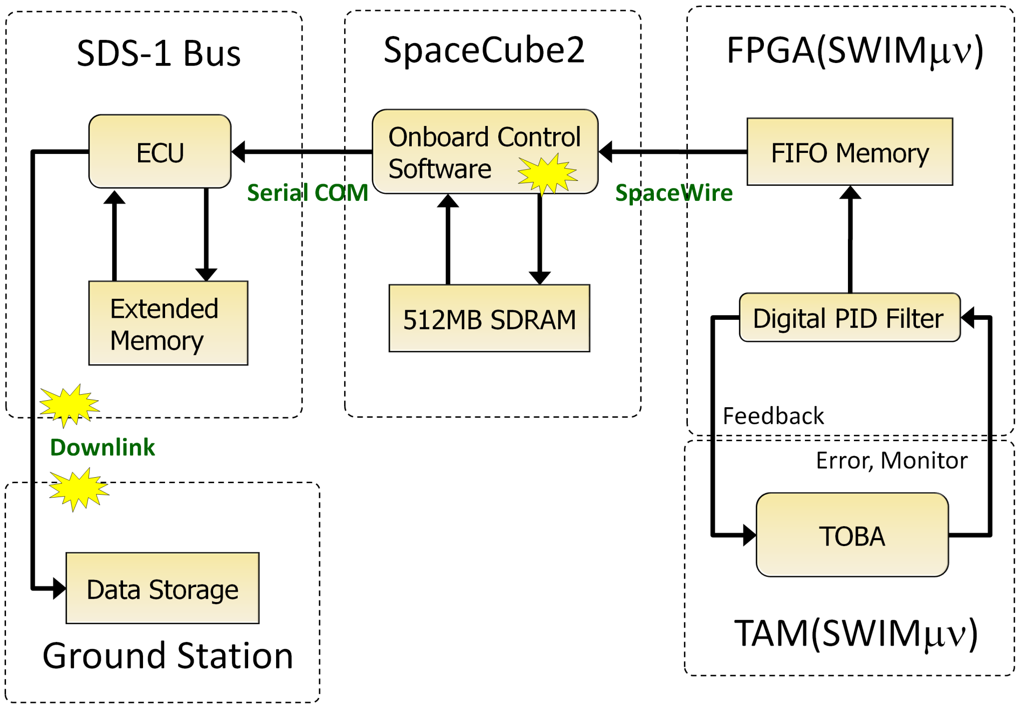

Figure 6.2: Overview of the data handling scheme. Boxes with dotted lines represent components. Although the FPGA and TAM are shown as different components in this figure, they are contained in the same housing. The three problems that occurred in the data handling are indicated as explosion marks.

are recombined and averaged and then saved in the synchronous dynamic random access memory (SDRAM) in SpaceCube2. The above process is carried out while the TOBAs are in operation. After the experimental run of the TOBA has stopped, the data are transferred to the extended memory of SDS-1 via the serial COM. The stored data are divided into ten segments typically. One of the segment is downloaded to the ground station for each pass and is sended to the operator as a binary file.

Three Types of Errors

Three types of data errors occurred at the same time. These are indicated by the explosion marks in Figure 6.2. Two of them are attributed to the downlink from the satellite and the other originated from a bug in the onboard software. These errors are identified as follows:

1. Packet loss: some packets were missing in the downlink.

2. Bit flipping: some bits in the data packets were flipped.

3. Software bug: this was a bug in the averaging process in the onboard software of SpaceCube2.

6.1.2 Error Correction Strategy

Figure 6.3 shows the overall structure of the restoration. Corresponding to the three types of the errors shown above, we apply three processes in a stepwise mannar as follows:

1. First, packet loss is searched for in the level-1 data. The two data sets are aligned with each other. This is shown as *Alignment* in Figure 6.3. The aligned output is called level-2 data.

2. Next, two sets of level-2 data are compared with each other. One way is to compare the data expressed in binary representation. The second way is that the cyclic redundancy check (CRC) code in each packet is checked to see if it has the correct value. The CRC is a error detection code. It is also used in many other systems such as data recording, reading, communications. These comparisons are shown in Figure 6.3 as *Comparison & CRC Check*. The output of this step is called level-3 data.

3. At the end of the error correction, the defects in the level-3 data due to the software bug are amended. This process is shown in Figure 6.3 as *Dirty Channel Recovery*. The processed level-4 data at the bottom of Figure 6.3 are used for the GW searches.

6.1.3 Results of Error Correction

Althogh the three errors occured in the data-handling framework, the origin of the errors were systematically identified. The errors were corrected by using the counters in the packets and the double-download method. Several number of packets still have errors, but we confirmed that the errors do not affect the sensitivity level of the detector.

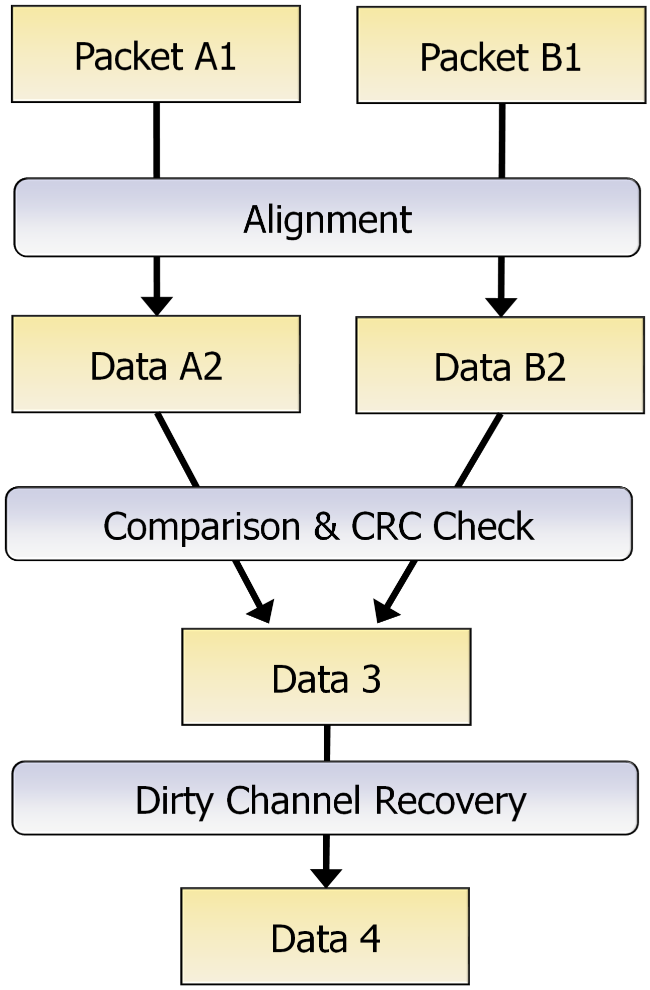

Figure 6.3: Data error correction strategy. Labels A and B denote the two sets of data packets obtained from the double download. The numbers represent the data level. Data A1 and Data B1 denote the data file, which is introduced in Section A.1. Boxes with rounded corners represent the three processes applied to the data. The level-4 data at the bottom are the result of the processes and are used in the GW search in Chapter 7.

Chapter 7

Search for Stochastic Gravitational Wave Background

The SGWB is one of the most important targets in the search for GWs as described in Chapter 2. It is a superposition of random waves and originates from cosmic sources such as inflation or the vacuum phase transition in the very early Universe, as well as a number of indistinguishable astrophysical sources.

Here, using our detector SWIM$_{\mu\nu}$ as a rotating TOBA, we set an upper limit on low-frequency GWs. By applying the frequency-upconversion technique, we could reach a frequency of approximately 10 mHz, which has rarely been used in searches with ground-based GW detectors. In addition, as shown in Chapter 3, the detector can sense forward and reverse polarization modes associated with its rotation.

The contents of this chapter are organized as follows. First, the characteristics of the SGWB, the response of the TOBA and previous progress in the search for the SGWB are reviewed. Next, the results of our search for the SGWB using SWIM$_{\mu\nu}$ are described. Details of the processes of analysis such as frequency conversion, data selection, estimator derivation and the setting of upper limits are also explained.

7.1 Stochastic Gravitational Wave Background

Here we review the characterization of the SGWB and previous observational results.

7.1.1 Characterization

The SGWB is a superposition of statistically random GWs. It is considered to exist as a background of astrophysical GW sources such as binary systems and supernovae. This is why the stochastic waves from cosmological sources are called backgrounds. In contrast, if the sources of stochastic waves are in front of the main target, the stochastic wave may be called a foreground. The relationship between the background and foreground is the same as that between a signal and a noise.

As described in Chapter 2, the various processes by which GWs are generated are considered to be sources of the SGWB. These fall into two general categories:

- Cosmological sources.
- The superposition of indistinguishable point-like sources.

In this analysis, we do not search for any particular sources. In other words, we do not conduct a parameter search based on a theoretical model. Only the upper limit of the energy density Ω_{gw} is set.

Statistical Assumptions

Here we assume the following statistical characteristics of the SGWB. More specifically, the following assumptions are made. The SGWB should be:

1. Stationary. This means that the properties of the SGWB are invariant with time, at least during the observation time. Since the age of the Universe is much larger than the observation time, this assumption is reasonable.

2. Gaussian. The signal induced by the SGWB should act as a Gaussian noise. According to the central limit theorem, the superposition of the same elementary process converges to the normal distribution. Although some theories predict the SGWB to be non-Gaussian, we do not consider this possibility in the analysis.

3. Isotropic. Naively speaking, the isotropy of the SGWB is thought to be the same type as that of the CMB. The CMB is isotropic upon zero-order approximation (the dipole component is on the order of 10^{-3}).

Regularly, unpolarized SGWB are assumed for an analysis. In this experiment, however, we perform an analysis that the polarization of the SGWB is separated. Thus, we do not assume an unpolarized SGWB and do not integrate over the freedom of the two polarization in the following calculations. As mentioned in Chapter 3, the forward and reverse modes are a superposition of circularly polarized GWs propagating in opposite directions.

Energy Density

In the theoretical field, it is common to express the intensity of the SGWB as a normalized energy density $\Omega_{\rm gw}(f)$. Thus, the relation between the energy density and its spectral amplitude should bu used for easy comparison with the detector sensitivity. The dimensionless quantity $\Omega_{\rm gw}$ characterizes the SGWB. It is expressed as

$$\Omega_{\rm gw}(f) = \frac{1}{\rho_{\rm c}} \frac{{\rm d}\rho_{\rm gw}}{{\rm d}\log f}, \tag{7.1}$$

where $\rho_{\rm c}$, $\rho_{\rm gw}$ and f are the critical energy density of the Universe, the energy density of the SGWB and frequency, respectively. The critical density of the Universe is expressed as

$$\rho_{\rm gw} = \frac{3H_0^2}{8\pi {\rm G}}, \tag{7.2}$$

using the present Hubble constant H_0. We use the recent value [60] of H_0 obtained from the combined analysis of seven years of observations from the Wilkinson Microwave Anisotropy Probe (WMAP), the observation of baryon acoustic oscillation and type IA Supernovae of

$$H_0 = 70.2 \pm 1.4 \ [\mathrm{km/s/Mpc}] \ . \tag{7.3}$$

However, for historical reasons, we use the quantity $h_0^2\Omega_{\rm gw}$ to express energy density of GWs. Here h_0 is the Hubble constant divided by 100 km/s/Mpc. This is because H_0 had relatively large (several tens of percent) uncertainties before the WMAP era.

Characteristic Amplitude

To discuss the effect of the SGWB on GW detectors such as the TOBAs and laser interferometers, we need to consider its amplitude. According to an excellent review [61], the relation between the energy density $\Omega_{\rm gw}$ and its characteristic amplitude $h_{\rm c}(f)$ is

$$\Omega_{\rm gw}(f) = \frac{2\pi^2}{3H_0^2} f^2 h_{\rm c}^2(f) \ . \tag{7.4}$$

In other words, replacing the characteristic amplitude $h_{\rm c}$ with the spectral density $S_{\rm h}(f)$ by using the relation

$$h_{\rm c}^2(f) = 2fS_{\rm h}(f) \ , \tag{7.5}$$

we can express the power spectral density in terms of the energy density of the SGWB as

$$\Omega_{\mathrm{gw}}(f) = \frac{4\pi^2}{3H_0^2} f^3 S_{\mathrm{h}}(f) \ . \tag{7.6}$$

Note that the above equations assume the existence of stationary, isotropic and unpolarized stochastic GWs.

Response of a Single Detector

Next we consider the response of a single detector to the SGWB in accordance with [61]. The time-domain signal $s(t)$ from the detector has the form

$$s(t) = h(t) + n(t) \ , \tag{7.7}$$

where $h(t)$ and $n(t)$ is GW signal and noise, respectively. The Fourier transformation $\tilde{h}(f)$ of the GW signal is expressed as

$$\tilde{h}(f) = \sum_{A=+,\times} \int \mathrm{d}\hat{\Omega} \tilde{h}_A(f, \hat{\Omega}) F_A(\hat{\Omega}) \ . \tag{7.8}$$

$F_A(\hat{\Omega})$ is a detector pattern function dependent on the direction $\hat{\Omega}$ (for more detail, see Chapter 3). Here the ensemble average Fourier amplitude of the isotropic, stationary and unpolarized SGWB is expressed as

$$\left\langle \tilde{h}_A^*(f, \hat{\Omega}) \tilde{h}_{A'}(f, \hat{\Omega}') \right\rangle = \frac{\delta^2(\hat{\Omega}, \hat{\Omega}')}{4\pi} \delta_{AA'} \delta(f - f') \frac{S_{\mathrm{h}}(f)}{2} \ , \tag{7.9}$$

using the Dirac delta functions δ and δ^2. Thus, using equations (7.6) and (7.9), we have

$$\left\langle h^2(f) \right\rangle = F S_{\mathrm{h}}(f) \ . \tag{7.10}$$

We used the integrated detector response F, defined by

$$F = \int \frac{\mathrm{d}\hat{\Omega}}{4\pi} \sum_{A=+,\times} F^A(\hat{\Omega}) F_A(\hat{\Omega}) \ . \tag{7.11}$$

Here we use $F = 2/5$, the value for the TOBA; thus we derive the relation between the amplitude at the detector $h(f)$ and the GW energy density Ω_{GW} at the observation frequency f_0 using equations (7.7) and (7.10):

$$\Omega_{\mathrm{gw}}(f_0) = \frac{10\pi^2}{3H_0^2} f_0^3 \left\langle h^2(f_0) \right\rangle \ . \tag{7.12}$$

7.1.2 Previous Observational Limits

Various efforts have been made to detect the SGWB. These can be divided into two types involving the indirect observation (mainly utilizing CMB characteristics) and direct observation of GWs.

Cosmic Microwave Background

From the results of seven years of observations from WMAP [60], an upper limit for the inflationary SGWB has been set using the CMB large-angle correlations and the relation between the CMB and matter spectra.

Big-Bang Nucleosynthesis

If GWs with a large amplitude existed at the time of nucleosynthesis, the predicted abundances of helium would differ from the observed value. A recent observation [62] of the abundance of helium limits the energy density of the SGWB to

$$\Omega_{\mathrm{gw}} h_0^2 < 7.8 \times 10^{-6} \ . \tag{7.13}$$

This is called the Big-Bang Nucleosynthesis (BBN) bound, which is a stringent indirect observational limit for the SGWB from the early Universe.

Pulsar Timing

The pulsar timing limits the energy density of the SGWB in the very low frequency range (10^{-9}—10^{-7} Hz) [63]. For a frequency of $1/(8 \text{ years}) = 4 \times 10^{-9}$ Hz, an upper limit for the inflationary relic SGWB $\Omega_{\mathrm{gw}}^{\mathrm{relic}}$ was set as

$$\Omega_{\mathrm{gw}}^{\mathrm{relic}} h_0^2 < 2.0 \times 10^{-8} \ . \tag{7.14}$$

They used a false alarm rate of 0.1%, whereas the detection rate was set to 95% for this analysis. They also provided a limit of for the SGWB from cosmic string of $\Omega_{\mathrm{gw}}^{\mathrm{cs}} < 1.9 \times 10^{-8}$ and a limit of $\Omega_{\mathrm{gw}}^{\mathrm{SMBH}} < 1.9 \times 10^{-8}$ for supermassive black holes .

Ground-based Laser Interferometers

The science-5 (S5) run of LIGO-Hanford and LIGO-Livingston set the most stringent limit [64] on Ω_{gw} for performing a direct search for GWs. The upper limit with a 95% confidence level is

$$\Omega_{\mathrm{gw}} < 6.9 \times 10^{-6}, \tag{7.15}$$

assuming that $\Omega_{\rm gw}(f)$ is constant over the frequency range of 41.5 Hz $< f <$ 169.25 Hz. Note that a direct observation sets a more stringent limit than an indirect BBN bound. This result is one of the major advances in modern interferometric GW detectors.

Tabletop Interferometers

To search for the SGWB in the very high frequency ($>$ 100 MHz) range, tabletop laser interferometers were developed [65]. In their setup, the signals of two different synchronous recycling (resonant recycling) interferometers with a 75 cm baseline are correlated. They were used to set an upper limit of $h_0^2\Omega_{\rm gw}(100\ {\rm MHz}) < 6\times10^{25}$ with a bandwidth of 2 kHz, assuming a flat SGWB spectrum in the observation frequency band.

Torsion-bar Antennas

The upper limit using a TOBA has also been set. Using a prototype antenna [66] with a superconductor magnet in its suspension system, the 95% confidence level for the upper limit of $\Omega_{\rm gw}$ at 0.1 Hz (bandwidth 100 mHz) was set to $\Omega_{\rm gw}h_0^2 < 4.3\times10^{17}$ [67]. In addition, the correlation analysis with multiple TOBAs at 300-km-distant sites was performed [68]. These results enabled us to set a 95% confidence upper limit of $\Omega_{\rm gw}h_0^2 < 1.2\times10^{19}$ with a false alarm rate of 1%.

7.2 Analysis

Here we analyze the data and set an upper limit for the SGWB using a frequency-upconversion scheme. The analysis was performed by two different approaches; a frequentist approach and a Bayesian approach.

7.2.1 Overview of Analysis

A flowchart of the analysis is shown in Figure 7.1. The first step is frequency conversion. Next, a data quality check and data selection are conducted. As the heart of the analysis, we set an upper limit using two different types of statistical treatment, frequentist and Bayesian. Finally, we use the estimated statistical errors and derive conservative upper limits for each circular polarization mode of the SGWB.

Selecting Observation Parameters

Generally it is a difficult issue to select the best parameters for the observation, since there are various conditions such as limitation of the detector or the computing power.

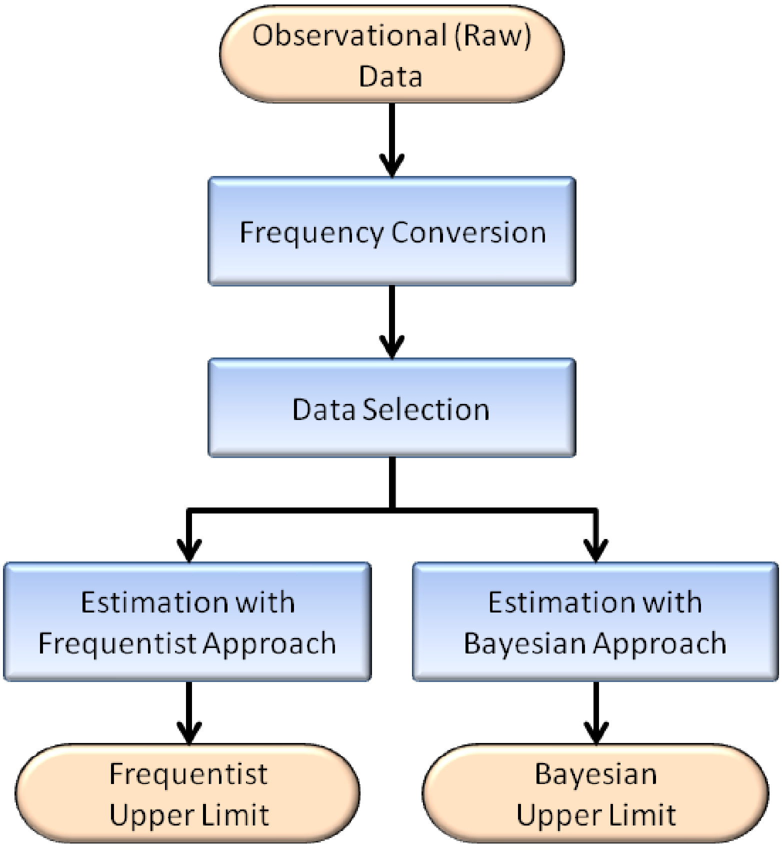

Figure 7.1: Overview of data analysis. Data and Results are shown in ellipses, while processes are in squares.

Here we mention how we determine the observation parameters used in this analysis.

The rotation frequency ω_{rot} is determined by the satellite rotation and we could not select the rotation frequency of the satellite. Nevertheless, the sensitivity of the detector does not have steep noise shape than f^{-2}. Thus, the improvement of the detector sensitivity in low-frequency using the frequency upconversion technique cannot be achieved by SWIM$_{\mu\nu}$.

The observation band is limited by the two factor; the observation time T and the sampling rate f_{s}. The bandwidth of the analysis f_{BW}, is limited by the observation time as

$$f_{\mathrm{BW}} = \frac{i}{T} \tag{7.16}$$
$$> \frac{1}{T}\ \mathrm{Hz}\ . \tag{7.17}$$

where integer i is the averaging factor. This relation limits the lower bound of the observation band. On the other hand, the upper bound of the frequency range is limited by the sampling rate, known as the Nyquist frequency:

$$f_{\mathrm{Nyq}} = \frac{f_{\mathrm{s}}}{2}\ . \tag{7.18}$$

Note that the amount of data U is proportional to the product of the two factor; $U \propto T \times f_{\mathrm{s}}$ at the same time. Thus, under a condition of the amount of data downloadable from the satellite, The two factor are in trade-off relation.

When the rotation frequency and the observation band are fixed, the frequency conversion gain G_{up}, shown in equation (3.53), are automatically determined.

$$G_{\mathrm{up}}(\omega_{\mathrm{gw}}, \omega_{\mathrm{rot}}) = \frac{1}{\sqrt{2}} \left(\frac{\omega_{\mathrm{gw}}}{2\omega_{\mathrm{rot}}} \right)^2 \tag{7.19}$$
$$= 2.65 \times 10^{-2}\ , \tag{7.20}$$

and here $\omega_{\mathrm{gw}} = 18$ mHz and $2\omega_{\mathrm{rot}} = 93$ mHz are applied in this experiment. This means that the amplitude of low-frequency GWs are suppressed by approximately 10^{-2}. This is a severe disadvantage of the frequency-upconversion technique. However, when the noise spectrum of the detector has a lot of narrow-band noises, this suppression can be an advantage. Note that the target of this GW search are not specified. Thus, we can select any frequency as a observation band without loss of generality.

The number of segment is also one of the free parameters for the analysis. Here we vary the number of segment to examine the dependence of the estimator of GWs. Figure 7.2 shows the relation of the averaging number and corresponding estimator for Ω_{gw}, with the observation frequency of 4.5 mHz. As long as the averaging is sufficient, the estimator do not vary significantly. Considering that sufficient number of the independent data is important to reduce the statistical error, we have to keep the balance between the statistical uncertainty and the averaging. Thus, we selected 64 as the number of bins.

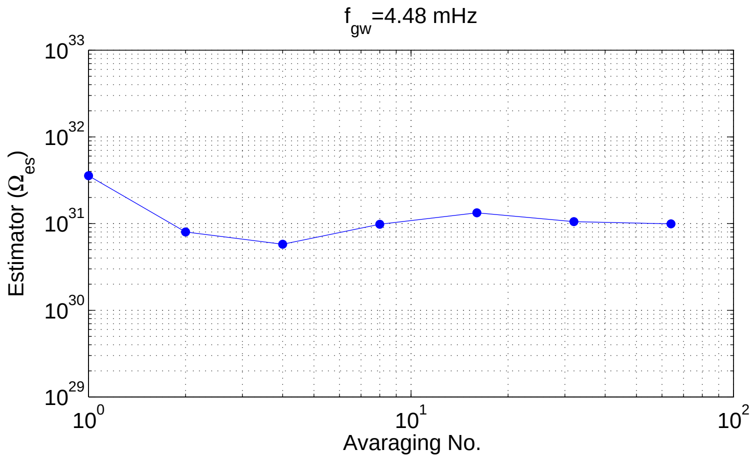

Figure 7.2: The dependence of the estimator $\Omega_{\rm es}$ on the number of data segment.

7.2.2 Preprocessing

Before performing the statistical estimation to set an upper limit, we performed the two process to the data, the data selection and the determination of the estimator, as a preprocess.

Data Selection

To perform a GW search, observational data is divided into 64 segments, and we derive the strain-equivalent noise $h(f_0)$ at the target frequency f_0 for each segment. The energy spectral density and strain are related by the equation

$$\Omega_{\rm gw}(f_0) = \frac{10\pi^2}{3H_0^2} f_0^3 h^2(f_0) \ . \tag{7.21}$$

Then we reject the data which exceeds five times of median. This method of data selection is justified[1] because we assume a stationary and random SGWB. The remained number of the data segments are 56.

Determining an Estimator

The number of data segments obtained in the previous step is N=56. Here we calculate an estimator of the GW energy density, $\Omega_{\rm es}$. If the S/N of the detector was sufficiently large, that is, the obtained signal was from all the SGWB, each data segment would have an exponential distribution with mean $\Omega_{\rm gw}$ and variance $\Omega_{\rm gw}^2$. Thus, distribution function

[1]There are many ways of selecting the dataset. In the case of optimal data selection, the least upper limit will be realized. However, we do not pursue that optimization of data selection.

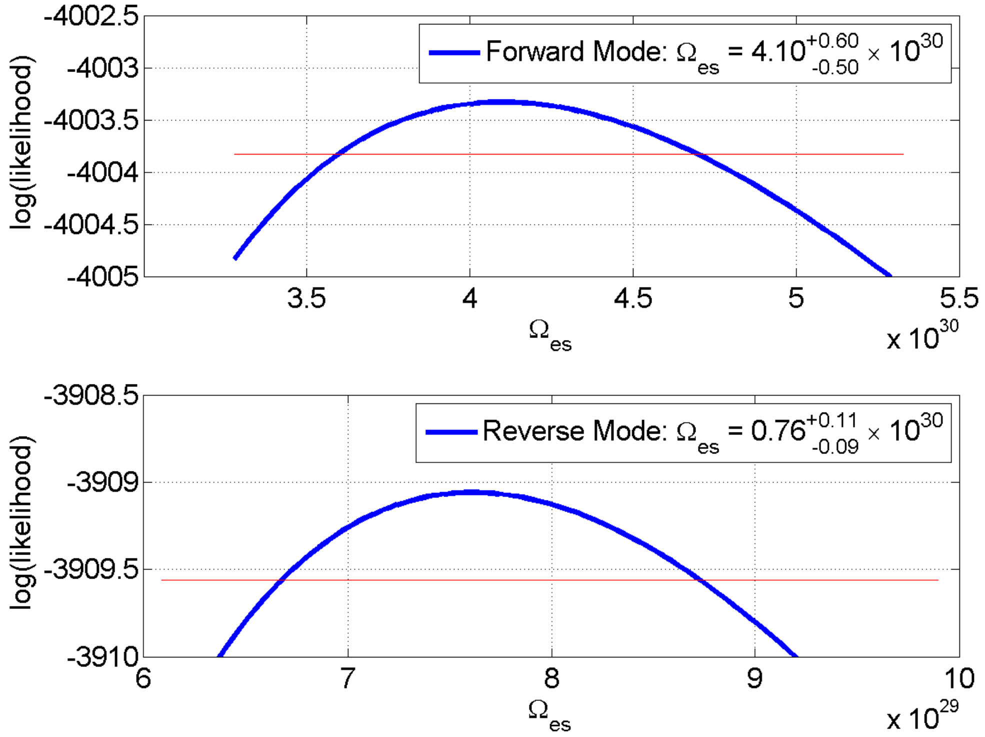

Figure 7.3: Determining an estimator for forward and reverse mode using maximum likelihood. The likelihood function for the forward mode is plotted in the top figure, while the bottom shows that of the reverse mode. The Y-axis is logarithmic. The results of the estimation of the two modes are also shown in the top right of the figures.

of Ω is

$$p(\Omega) = \frac{1}{\Omega_{\rm gw}} \exp(-\frac{\Omega}{\Omega_{\rm gw}}). \tag{7.22}$$

Here we apply the maximum-likelihood method for the estimation.

Thus, we obtain the estimator as

$$\Omega_{\rm es}^{\rm FW} = 4.10^{+0.60}_{-0.50} \times 10^{30} \tag{7.23}$$

for the forward mode and

$$\Omega_{\rm es}^{\rm RE} = 0.76^{+0.11}_{-0.09} \times 10^{30} \tag{7.24}$$

for the reverse mode with one-sigma deviation as shown in Figure 7.3.

Using these estimators, we plot a histogram of the N=56 data segments in Figure 7.4. The exponential curves with the estimated parameters $\Omega_{\rm es}^{\rm FW}$ and $\Omega_{\rm es}^{\rm RE}$ are also plotted.

The number of bins of the histogram was chosen to be that proposed by Sturges [69], which is described as an appropriate selection method in [70]. Sturges proposed that the number of bins $N_{\rm bin}$ should be

$$N_{\rm bin} = 1 + \log_2 n \ , \tag{7.25}$$

where n is the sample size. Here we used 56 samples after data selection; thus we selected the number of bins as 7.

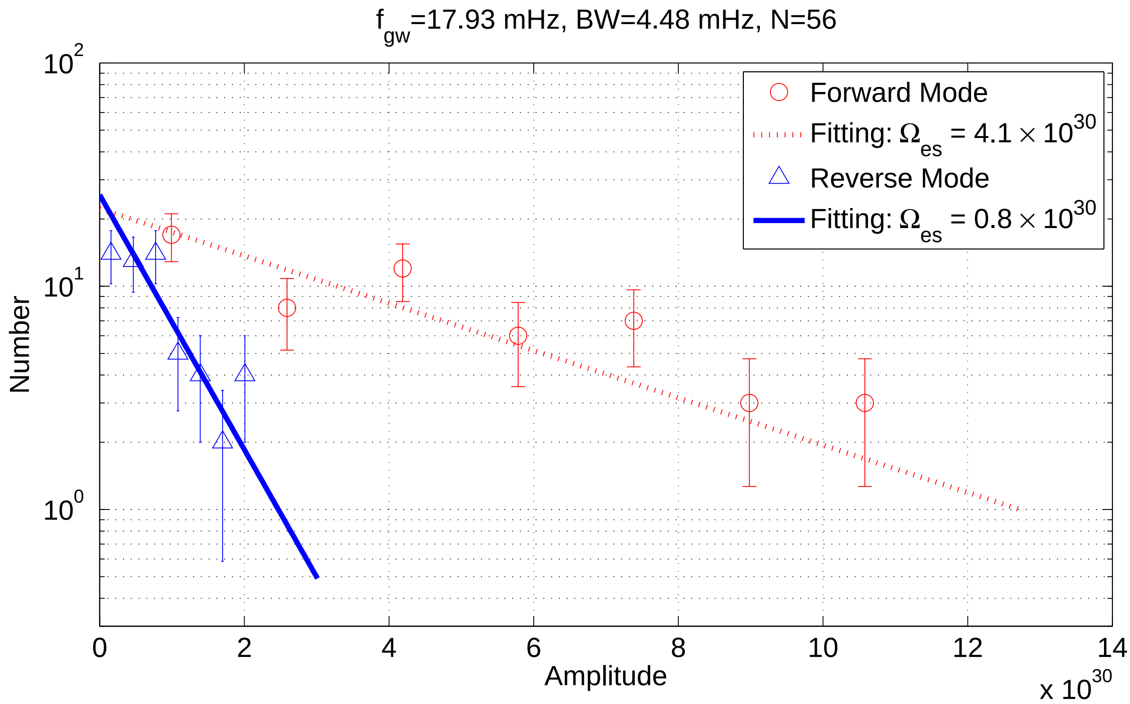

Figure 7.4: Histogram of GW energy for the data segments. The data are fitted with exponential curves. BW and N in the top of the figure are the bandwidth of the observation and the number of data segments, respectively. Circles and triangles represents the forward and reverse mode.

7.2.3 Upper Limit Obtained by Frequentist Approach

One of the statistical methods for determining an upper limit is the so-called frequentist[2] approach. "Frequentist" refers to a conventional approach in statistics. In contrast with the Bayesian approach used later, this approach is widely accepted in many scientific fields.

The statistical upper limit of $\Omega_{\rm GW}$ with confidence level C $(0 < C < 1)$ will satisfy the

[2]This viewpoint in statistics is also called Neyman-Pearson theory or the classical statistics

equation

$$C = \int_{\Omega_{\rm es}^{A}}^{\infty} \mathrm{P}(\Omega'|\Omega_{\rm gw}^{UL})\mathrm{d}\Omega' \ . \tag{7.26}$$

Here A = {FW, RE} and $P(\Omega'|\Omega_{\rm gw})$ is conditional probability distribution function (PDF). This PDF is that the probability of estimator Ω' obtained from the observation data when the SGWB $\Omega_{\rm gw}$ exists. Since $P(\Omega|\Omega_{\rm gw})$ is a PDF, it satisfies the normalization condition:

$$\int_{0}^{\infty} P(\Omega'|\Omega_{\rm gw})\mathrm{d}\Omega' = 1 \ . \tag{7.27}$$

Thus, this PDF is proportional to the normal distribution:

$$P(\Omega'|\Omega_{\rm gw}) \propto \exp\left(-\frac{(\Omega' - \Omega_{\rm gw})^2}{2\Omega_{\rm gw}/N}\right) \ . \tag{7.28}$$

In addition, we set the significance level C to be 0.95. This value has been widely used in other GW searches. The false dismissal rates for the forward and reverse modes are plotted in Figures 7.5 and 7.6, respectively.

Assumptions

Here, the following two assumptions are used with the frequentist approach:

1. The detector does not detect true SGWB signals.
2. The true GW amplitude is much lower than the equivalent noise level of the detector. Thus, we disregard the possibility that the estimated amplitude of GWs is lower than the true GW amplitude. In other words, we consider that the results are not at the lower tail of the detector's noise distribution but at the higher tail.

7.2.4 Upper Limit Obtained by Bayesian Approach

In contrast to the frequentist approach, the Bayesian approach is a modern statistical methods. that has recently become used in the field of GW data analysis. Note that most analyses in particle physics adopt the Bayesian approach.

Discrepancies in setting the upper limit of GWs resulting from the use of the two different approaches have been analyzed in some papers. For example, [71] discusses the differences between the two approaches in a simple GW search (the detection of a single sinusoidal signal in white noise). If S/N is large (the signal is apparent), there is no difference between the two approaches.

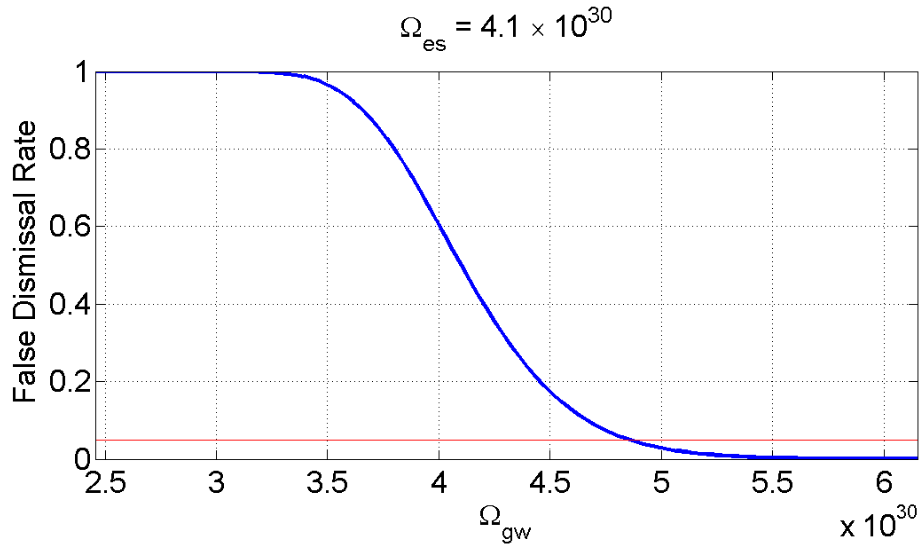

Figure 7.5: GW energy density versus false dismissal rate for forward mode at fixed detector noise level. The X-axis represents the GW energy density of the SGWB, while the Y-axis shows the false dissmisal rate of the detector. The false dismissal rate level of 0.05 is shown as a horizontal line.

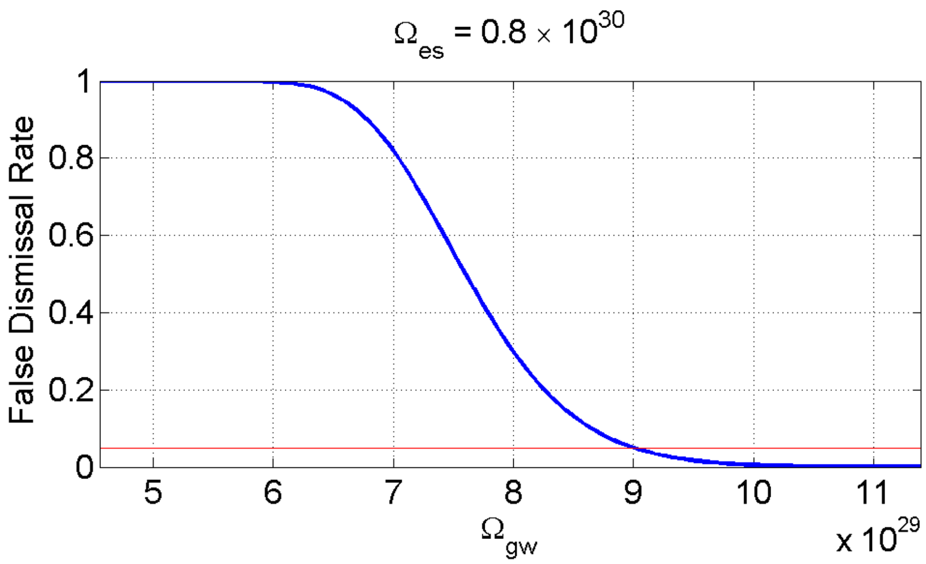

Figure 7.6: GW energy density versus false dismissal rate for reverse mode at fixed detector noise level. The X-axis represents the GW energy density of the SGWB, while the Y-axis shows the false dissmisal rate of the detector. The false dismissal rate level of 0.05 is shown as a horizontal line.

Method

The principal theorem in Bayesian statistics is Bayes's theorem:

$$P(A|B) = \frac{P(B|A) \cdot P(A)}{P(B)} \ , \tag{7.29}$$

where $P(A|B)$ is the posterior probability, i.e., the probability of A when B occurs. $P(A)$ is called the prior probability, $P(B)$ is the probability of B, and $P(B|A)$ is a likelihood function of B when A occurs. Replacing A with the event "there is a stochastic background of energy density Ω_{gw}" and B with the event "Ω_{es} is derived from the obtained data", then Bayes's theorem becomes

$$\begin{aligned} P(\Omega_{\text{gw}}|\Omega_{\text{es}}) &= \frac{P(\Omega_{\text{es}}|\Omega_{\text{gw}}) \cdot P(A)}{P(B)} & (7.30) \\ &\propto P(\Omega_{\text{es}}|\Omega_{\text{gw}}) \ . & (7.31) \end{aligned}$$

Results

Compared with the frequentist approach, it is relatively easy to calculate an upper limit in the Bayesian approach. The upper limit with a 95% degree of belief Ω_{gw}^{UL} satisfies

$$\int_0^{\Omega_{\text{gw}}^{UL}} P(\Omega_{\text{gw}}|\Omega_{\text{es}}) \, \mathrm{d}\Omega_{\text{gw}} = 0.95 \ . \tag{7.32}$$

By integrating equation (7.32), we derive the posterior PDF with a 95% degree of belief. The results are shown in Figure 7.7 for the forward mode and Figure 7.8 for the reverse mode. In this calculation, we used a flat prior which is an uniform distribution. As a summary, the upper limits derived considering only the statistical errors are given in Table 7.2.4.

Table 7.1: Upper limits for two polarization modes of normalized energy density Ω_{gw} of SGWB at 18 mHz.

	Frequentist Upper Limit	Bayesian Upper Limit
Forward Mode	$4.9^{+0.7}_{-0.6} \times 10^{30}$	$5.6^{+0.8}_{-0.7} \times 10^{30}$
Reverse Mode	$0.90^{+0.13}_{-0.11} \times 10^{30}$	$1.0^{+0.15}_{-0.13} \times 10^{30}$

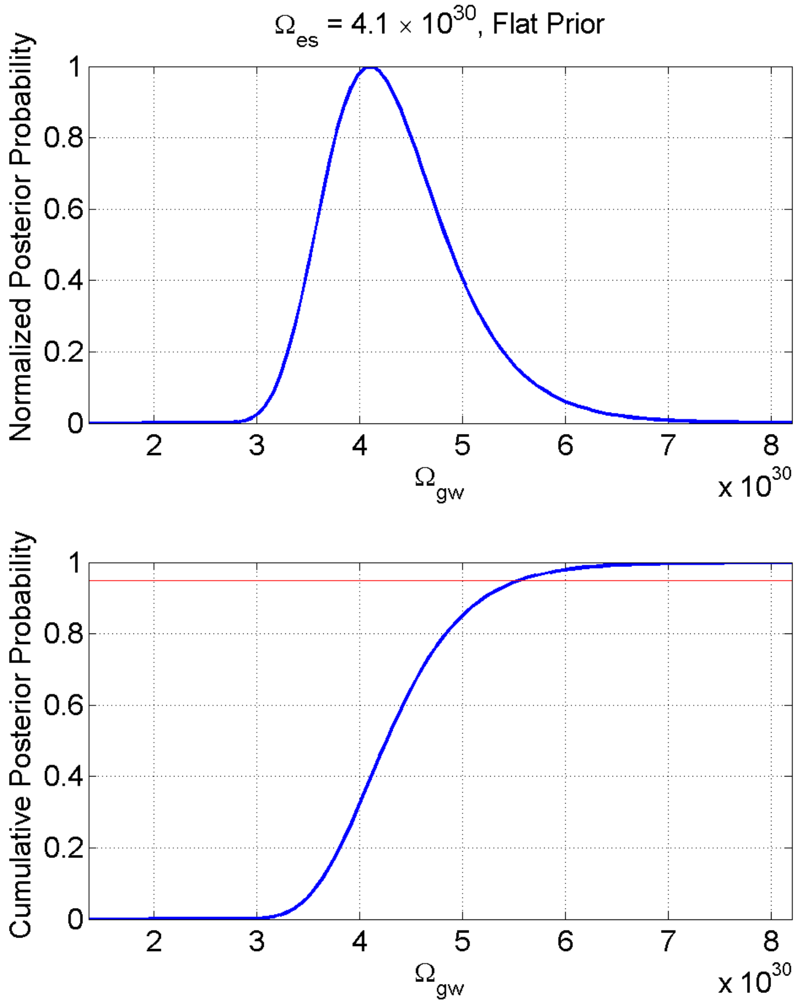

Figure 7.7: Normalized and cumulative posterior probability for forward mode. The top figure shows the normalized posterior probability with a flat prior. The bottom figure shows cumulative probability with the thin line showing y=0.95.

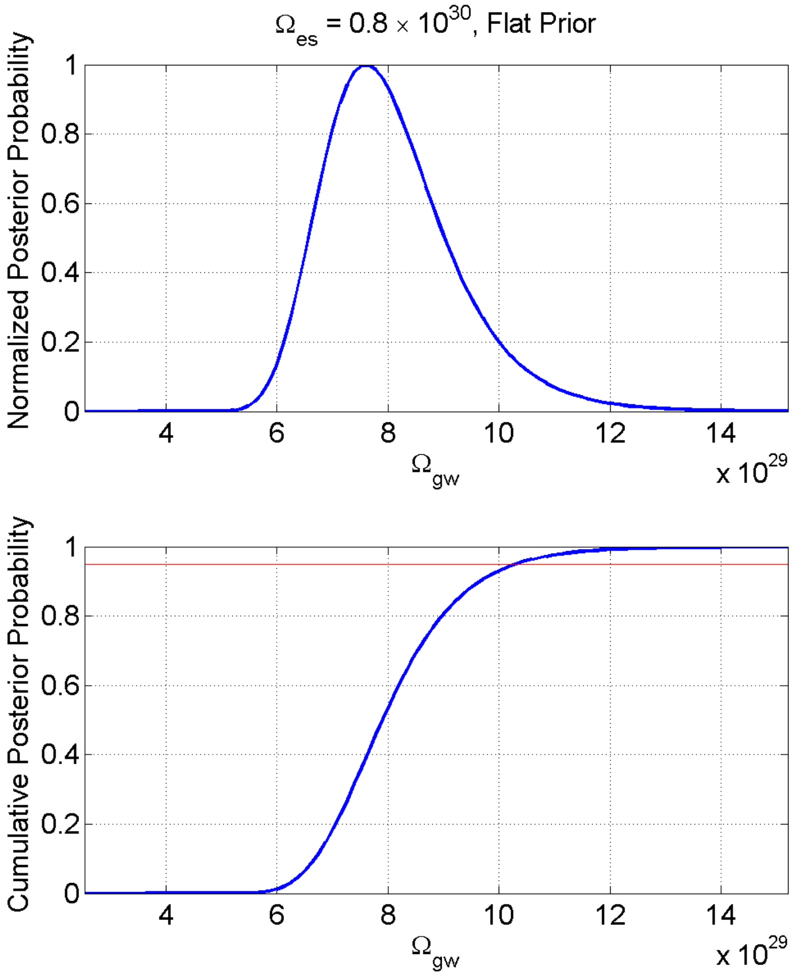

Figure 7.8: Normalized and cumulative posterior probability for reverse mode. The top figure shows the normalized posterior probability with a flat prior. The bottom figure shows cumulative probability with the thin line showing y=0.95.

7.2.5 Note on Upper Limit When Using One Detector

When the SGWB appears in the signals obtained by GW detectors, it cannot be distinguished from a noise owing to its randomness. Namely, the SGWB cannot be detected when we use a single detector. Thus, we can only separate it from noise in the detector by the correlation analysis of the signals from multiple detectors. In other words, the analysis presented in this thesis only gives an upper limit for the SGWB, i.e. our detector cannot be used to determine whether the SGWB is detected or not.

7.2.6 Conservative Upper Limit

Since the systematic error is set to 200% as shown in Section 5.3, we have three times higher upper limits when applying them to the results in Table 7.2.4. Specifically, the the upper limit for the forward mode

$$\Omega_{\rm gw}^{\rm FW} < 1.7 \times 10^{31} \ , \tag{7.33}$$

and for the reverse mode

$$\Omega_{\rm gw}^{\rm RE} < 3.1 \times 10^{30} \ . \tag{7.34}$$

Here we chose the frequentist approach to acquire better results. This is justifed by the freedom of selecting the method of analysis.

7.3 Summary

A search for SGWB is conducted. Ninety-five percent upper limits for the two polarization modes for the SGWB are set. The observation frequency and bandwidth were 18 mHz and 4.5 mHz, respectively. The rotation axis of the satellite was directed to the Galactic center. We have the results as: 1.7×10^{31} for the forward mode and 3.1×10^{30} for the reverse mode.

Chapter 8

Future Prospects

In this chapter, the following issues are discussed. First, the achievement of the SWIM$_{\mu\nu}$ is summarized. The discussion is separated to a scientific viewpoint and a technological viewpoint. Next, future prospects of the rotating TOBA are discussed. A ground-based large-scale rotating TOBA, quantum-noise-limited TOBA called the ultimate TOBA and spaceborne TOBA, are considered.

8.1 Futurizing the SWIM$_{\mu\nu}$ Project

SWIM$_{\mu\nu}$ can be used to demonstrate satellite technologies and instruments for GW physics is space. Here we review our achievements using SWIM$_{\mu\nu}$ and possible future progress.

8.1.1 Scientific Achievement

In terms of the sensitivity to GWs, SWIM$_{\mu\nu}$ does not have high sensitivity compared with ground-based detectors. However, using SWIM$_{\mu\nu}$, we have achieved some technological goals that are expected to pave the way for low-frequency GW observations. Specifically, there are three points to mention regarding the significance of the project: (i) it has expanded the field of GW detectors into space, (ii) low-frequency GW observation using TOBA has been achieved and (iii) a new technique has been realized for observing low-frequency GWs, i.e., frequency-upconversion technique.

Realizing a Spaceborne TOBA

SWIM$_{\mu\nu}$ has been successfully used to observe GW from space, to the best of our knowledge, for the first time. This should be an primary advancement of the GW community.

One of the advantages of space detectors for low-frequency GW observation are their long baseline. In the fixed-frame picture, the displacement induced by GWs is proportional to the baseline; thus, a long baseline greatly improve the sensitivity of GW detectors. In other words, the most sensitive frequency of the laser interferometer, f_{sens}, has the following relation with the size of the interferometer:

$$
\begin{aligned}
f_{\mathrm{sens}} &\sim \frac{c}{4LN} && (8.1)\\
&= (250\ \mathrm{Hz}) \left[\frac{L}{3\ \mathrm{km}}\right]^{-1} \left[\frac{N}{100}\right]^{-1}, && (8.2)
\end{aligned}
$$

where L and N are the baseline length of the interferometer and round trip number, respectively.

A quiet environment is also an important advantage of spaceborne GW detectors. In large-scale ground based laser interferometers, the test masses are suspended with wires. Although the suspension system reduces the seismic noises above the resonant frequency, typically about 1 Hz, the sensitivity at low frequencies is limited by seismic noise.

Another advantage of the space environment is zero gravity. There is no need for the suspension of the test mass in the space. This means that a free mass can be realized at a very low frequency. At the same time, a suspension thermal noise, which is a dominant noise source in a laser interferometer at middle frequencies, can be avoided in the detector without suspensions.

Note that the important result of the project is low-frequency GW observation using a TOBA. Although some demonstrations of the TOBA have been carried out in the laboratory, SWIM$_{\mu\nu}$ is the first detector in the field to be operated in space.

Demonstration of Frequency-Upconversion Technique

The most significant result of this experiment is that the frequency-upconversion technique has been applied to the data obtained from SWIM$_{\mu\nu}$ as a rotating TOBA. Frequency upconversion is a novel technique that we proposed for detecting low-frequency GWs. The advantages of this technique are described in Chapter 3.

We conducted a search for the circular polarization of the SGWB for the first time. Although this observation is not as sensitive as other experiments, the methodology has possible application to GW astronomy in the future. For example, if the circular polarization from a binary pulsar is detected directly, the orbit parameter of the binary system can be determined with less uncertainty. Moreover, in quantum gravity or superstring theory, it has been predicted that the two circular polarization of GWs propagates at the different speeds when the gravitational interaction violates the parity symmetry. As seen above, the rotating TOBA may be a suitable tool for carrying out such astronomical observations or test of fundamental physics.

8.1.2 Technological Advances

Application of SWIM$_{\mu\nu}$ Technology to Future Missions

Some technologies common to future GW detector missions have been used in SWIM$_{\mu\nu}$. One example is the position control system used for the test mass. In future spaceborne GW interferometers, the test mass module will be monitored by local sensors and controlled to the correct position so that the main interferometer can operate. A difference between the position control system of SWIM$_{\mu\nu}$ and that in DECIGO Pathfinder (DPF), which is the satellite mission proposed by Japanese researchers, is that the module in DPF consists of a monolithic mirror and a spacer made of a material with low magnetic susceptibility, while the test mass of SWIM$_{\mu\nu}$ is a aluminum bar. Another difference is the method of measurement of the displacement of the test mass. For DPF, electrostatic sensors and the main laser interferometer will be used to sense the position of the test mass module. On the other hand, photoreflective position sensors are used in SWIM$_{\mu\nu}$. Despite these differences, the control algorithm for DPF will be similar to that of SWIM$_{\mu\nu}$, and thus, technology of SWIM$_{\mu\nu}$ can be applied to the system of DPF.

Another technology that has been demonstrated is the communication system. Specifically, the next-generation communication standard called SpaceWire is used in the datalink between SWIM$_{\mu\nu}$ and the onboard computer SpaceCube2. During the mission, about 2000 MB of data was transferred via SpaceWire without any error in the connection. These results have contributed to improving the technical readiness level (TRL) to the seventh grade, which means that the technology has been demonstrated in orbit as an integrated system. Since SpaceWire will be used not only in DPF but also in next-generation scientific satellite missions, the demonstration of SWIM$_{\mu\nu}$ in space is an important step toward the development of future missions.

Lessons Learned

We have experienced many problems of SWIM$_{\mu\nu}$, and we have learned many lessons in not only the development of spaceborne GW detectors but also the operation of on-orbit instruments as follows.

- The rotation rate of the satellite was sufficiently stable for the rotating TOBA.
- For a mechanical system, space environment which has no gravity and air is a simple and less-disturbance environment. Simulations or analytic predictions will work well in such an system.
- The effect of the geomagnetic field was strong. The magnetic susceptibility of the material used in the spaceborne precise equipment should be considered carefully.
- One of the TAM has failed to be operated. We suspect the cause was a stuck of the test mass in the TAM. This fact implies that the successful operation of the detector was just a lucky and the both TAMs might be failed. Redundancy is the most important design concept.

For more details, a document is being prepared [72].

Experiment Platform onboard a Small Satellite

It is meaningful that the scientific experiment was conducted using compact equipment onboard a small satellite. In general, a small satellite has extremely limited resources such as electricity, available weight and data transfer. In fact, SWIM$_{\mu\nu}$ has a mass of only 3 kg weight including its front-end electronics. The amount of data obtained from SWIM$_{\mu\nu}$ was about 20 MB. Although this lack of resources only applies to small satellites, i.e., larger missions should not be subjected to such constraints, the difficulty of conducting scientific experiments is a common issue. From this viewpoint, our experience obtained from SWIM$_{\mu\nu}$ should be of significant assistance in planning future missions.

8.2 Future Prospects of Rotating TOBA

In this section, possible future plans for the rotating TOBA are discussed. We consider three cases: (i) a ground-based rotating TOBA with realistic noise levels, (ii) an ultimate TOBA that is only limited by quantum (fundamental) noise, and (iii) a spaceborne TOBA with parameters that can be launched by the Japanese launch vehicle H-IIA.

8.2.1 Ground-based Rotating TOBA

As a future improvement, we consider the sensitivity of a large-scale TOBA. Figure 8.1 shows the sensitivity curves for a large-scale TOBA and the rotating TOBA. We assumed the detector parameters in Table 8.1 for the large-scale TOBA. These parameters are selected to be realistic values that are expected to be achievable in the future.

The rotation frequency is set to 0.5 Hz so as to use the most sensitive frequency band in the observation. The sensitivities for the forward mode and reverse mode of the rotating TOBA are shown as red and green lines, respectively. The estimated sensitivity is approximately 10^{-15} at 1 mHz, which is less than that of LISA by factor of two or three. However, it should be noted that this sensitivity level can be realized by ground-based detectors, which have a significantly lower cost.

Table 8.1: Description of parameters and assumed values for large-scale TOBA.

Notation	Description	Assumed Value
λ	Wavelength of laser	1064 nm
P_{in}	Input power of the laser interferometer	10 W
N	Round trip number of Fabry-Perot cavity	70
L	Length of torsion-bar	10 m
M	Mass of torsion-bar	7600 kg
I	Moment of inertia of torsion-bar	6.4×10^4 Nms^2
γ	Loss factor of suspension system	10^{-10} Nms
ϕ_{mass}	Loss angle of vibration mode of torsion-bar	10^{-7}
T	Temperature of the detector	4 K

8.2.2 Ultimate TOBA

Here we consider a TOBA that is limited only by fundamental quantum noise, which we call an ultimate TOBA. We estimate the sensitivity of an ultimate TOBA to evaluate its potential for use in future GW observations. The following parameters are used to calculate the sensitivity: The other detector parameters are same as ground-based large-scale TOBA introduced above.

Observable range for ultimate and rotating TOBAs are shown in Figure 8.3. The curves are plotted for binary black hole inspirals. We used a possible frequency and intensity of such inspirals simulated by numerical relativity [73]. We assume that S/N is 3 and the mass ratio of the binary is 1, i.e., we consider equal-mass binaries. The spin parameter of the black holes is fixed to 0.5. In this calculation, we also assume that a collision of equal-mass black holes are in the optimal direction. These assumptions are widely accepted in the simulation of waveforms of GWs in the field of numerical relativity. Note that

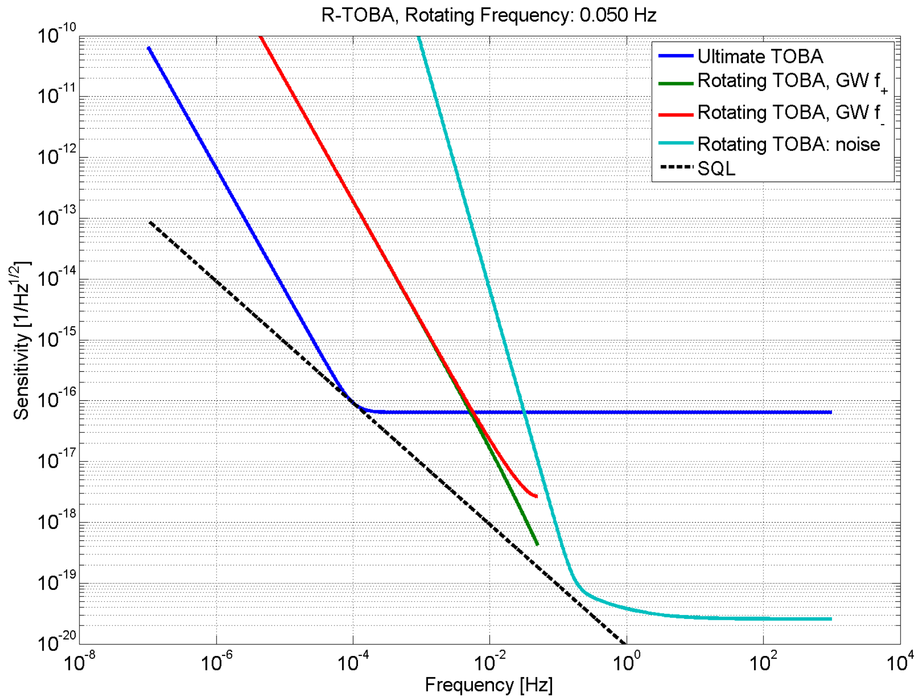

Figure 8.1: Sensitivity curves for rotating TOBA and ultimate TOBA. The black dotted curve shows the SQL for these TOBA.

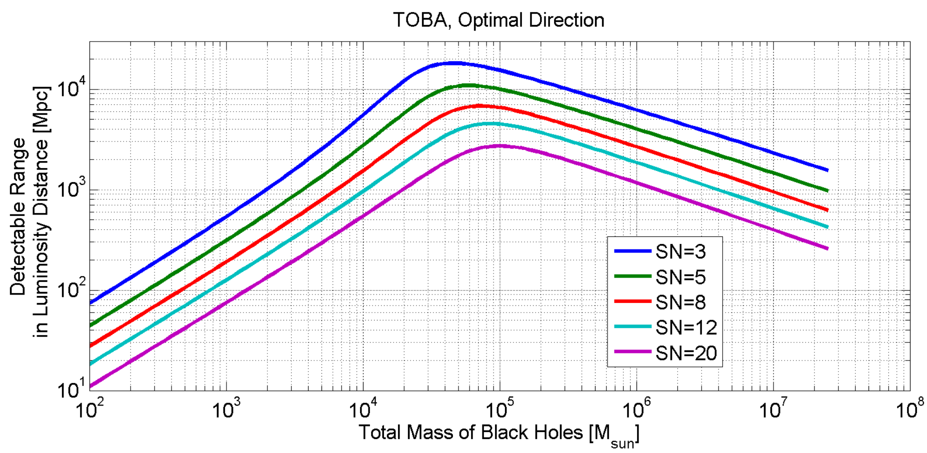

Figure 8.2: Detectable range of large-scale TOBA. Curves are plotted for S/N=3, 5, 8, 10 and 12.

the rotating ground TOBA has better sensitivity in the frequency above $\sim 10^{-2}$ Hz than ultimate TOBA, since the ultimate TOBA is optimized to have the best sensitivity at 10^{-4} Hz with assumed parameters. This is why observable range of the ultimate TOBA in the total mass of BHs below 4×10^4 solar mass is shorter than that of the ground TOBA.

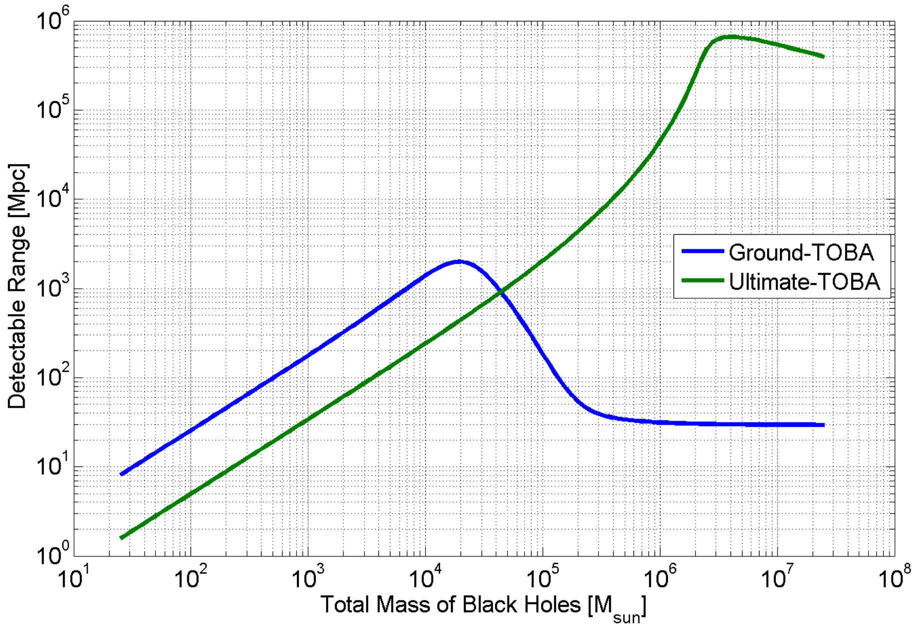

Figure 8.3: Observable ranges of ground-based rotating TOBA and ultimate TOBA. These curves are plotted for S/N = 3.

8.2.3 Spaceborne TOBA

A spaceborne large-scale TOBA, whose length is about 4—5 m, can be considered. Some research institutes have begun to consider spaceborne TOBAs as future GW detectors onboard small satellites, taking advantage of the compactness of TOBAs [74]. We expect that the observable range of such a detector will be about 1 Gpc for black hole binaries of 10^4 $M_\odot$. This should give sufficiently high sensitivity to detect GWs at a detection rate of at least several times a year.

8.3 Summary

As future prospects based on this experiment, the sensitivity of the TOBA and the performance with large-scale experiments using a rotating TOBA are discussed. It is

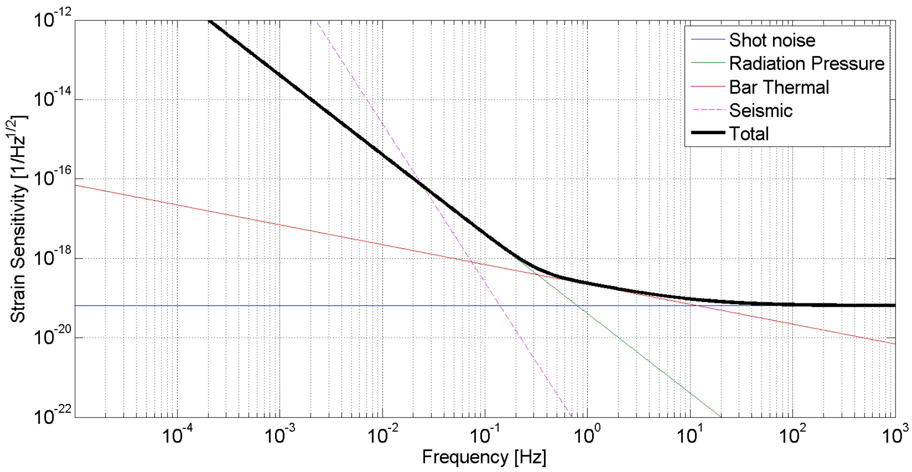

Figure 8.4: Sensitivity curve of spaceborne 4 m TOBA. The spectra of fundamental noise sources are also shown. For reference, the seismic noise level is plotted on the same graph.

expected that GWs from black-hole binaries with a solar mass of $10^4 - 10^7$ can be detected using a spaceborne large-scale TOBA with test masses of length 4 m. The rotating TOBA has the potential to become an effective tool for low-frequency GW astronomy in the future.

Chapter 9

Summary and Conclusion

9.1 Summary

Here we give a summary of this thesis.

Observation of Low-Frequency Gravitational Waves

GWs are ripples of spacetime, which are predicted in the general theory of relativity. They are so faint that their direct detection has not yet been reported. On the basis of low-frequency (about 10^{-4} — 1 Hz) GW observations, it is expected that many unresolved scientific issues can be investigated that cannot studied through conventional observations. Examples of such issues include (i) revealing the evolution of galaxies through observation of the coalescence of supermassive black-hole binaries, (ii) testing the theory of gravity, (iii) measurement of the accelerating cosmic expansion independently of electromagnetic observations and (iv) determining the physical theory of inflation by directly detecting inflationary stochastic GWs. However, it is difficult to detect GWs, particularly in this low-frequency region, owing to the intense noise and the fluctuation of gravity around the detector.

It is considered that such low-frequency GW observations will be realized using future space-based GW detectors. European researchers have proposed the eLISA project, which will target the 10^{-6} – 10^{-3} Hz range. Japanese researchers have also proposed another spaceborne mission named DECIGO to search for decihertz GWs. The development of these space-based detectors involves a high cost, high risk and the need for sophisticated technologies. Pathfinder missions such as DPF and LISA Pathfinder have been proposed or are under preparation.

Torsion-Bar Antenna

A TOBA is a novel type of GW detector for low-frequency GW observations [40]. It is based on a property of GWs that the tidal force induced by GWs causes the rotational motion of a test mass suspended in the TOBA. In contrast to ordinary laser interferometers, a test mass in a TOBA can be suspended by a "soft" system, namely, it has a lower resonant frequency; thus, the TOBA has higher sensitivity to low-frequency GWs. Prototype detectors have been developed [67], and observations of 0.1-Hz-band stochastic GW backgrounds have been conducted [66–68].

Frequency-upconversion Technique using Rotating TOBA

The entire TOBA system can be rotated around its center. We named a TOBA with this type of operation the rotating TOBA. We proposed a frequency-upconversion technique for low-frequency GWs using a rotating TOBA. In detail, low-frequency GWs are upconverted to nearly twice the rotational frequency of the detector. If the rotation frequency of the detector is $\omega_{\rm rot}$, then the observation frequency will be $2\omega_{\rm rot} \pm \omega_{\rm gw}$. Here $\omega_{\rm gw}$ should be much lower than $2\omega_{\rm rot}$. In this case, the signal in the lower sideband, $2\omega_{\rm rot} - \omega_{\rm gw}$, represents the circular polarization of GWs in accordance with the detector's rotation. We call this the forward mode. In the same way, the upper sideband, $2\omega_{\rm rot} - \omega_{\rm gw}$, represents the opposite circular polarization, named the reverse mode.

The rotating TOBA has three advantages over an ordinary detector. First, as mentioned above, frequency-upconversion can be realized. Seismic and Newtonian noise (gravity fluctuation) become large at low frequencies. The frequency-upconversion technique provides a new means of avoiding these large noises. Second, twice as much information is extracted from the detector as from conventional detectors. That is because two frequency regions, $2\omega_{\rm rot} \pm \omega_{\rm gw}$, can be used for the observation. A GW detector can be regarded as a single element, that is, simultaneous observation with multiple detectors is necessary for GW astronomy. Thus, this property of doubling the amount of information may be useful from an astronomical viewpoint. Finally, the rotating TOBA has direct sensitivity to circular polarization (more precisely, its anisotropy). Although an array of laser interferometers can be used to observe circular polarization, the rotating TOBA can be oriented in any chosen direction. This property is also advantageous for astronomy.

Spaceborne Torsion-bar Antenna: SWIM$_{\mu\nu}$

We developed a tiny spaceborne TOBA called SWIM$_{\mu\nu}$, which was installed in a small satellite named SDS-1. This satellite was developed as one of the small demonstration satellite of JAXA. SWIM$_{\mu\nu}$ contains aluminum bar-shaped test masses. Their positions are controlled using a feedback system, which consists of infrared displacement sensors, a digital PID filter implemented on a FPGA, coil-magnet actuators and a data-handling scheme. When its sensitivity is limited by the noise of the position sensors, it should have a sensitivity of about 10^{-7} $/\sqrt{\text{Hz}}$ at around 0.1 Hz.

SWIM$_{\mu\nu}$ and DPF apply common technologies. For example, the rough position control system of the mirror assembly for DPF is similar to that of the test mass in SWIM$_{\mu\nu}$. In addition, an upgraded version of SpaceCube2, which was onboard SDS-1, will be used as an integrated controller of DPF. The demonstration of these technologies is very meaningful in the development of the satellites. That is why reliability is the most important property in spacecraft engineering. SWIM$_{\mu\nu}$ is also contributing to the on-orbit demonstration of the SpaceWire/RMAP, which is being developed as a future communication standard for a network of spacecraft. In other words, the successful operation of SWIM$_{\mu\nu}$ is playing an important role in boosting the TRL of SpaceWire-related equipment, which is to be widely used in future scientific satellites.

Experiments in Orbit

The detector was successfully launched into orbit, and operations were carried out from February 2009 to September 2010. The satellite was spinning when SWIM$_{\mu\nu}$ was in operation so that SWIM$_{\mu\nu}$ acted as a rotating TOBA. The check-out operation, the confirmation of test mass position control, measurement of the noise level and calibration were conducted in this operational phase. The dominant noise source in the observation frequency band, i.e., around 90 mHz was the quantization noise in the data handling system. Observational runs were carried out in June and July 2010. SWIM$_{\mu\nu}$ was used for observation during three orbits of the satellite (about 300 min). The satellite was spinning when SWIM$_{\mu\nu}$ was in operation so that SWIM$_{\mu\nu}$ acted as a rotating TOBA. During the observation, the satellite stabilized its attitude using its spin of 46.5 mHz. The axis of the spin was directed to the center the Galaxy. The sensitivity of the detector around twice the rotation frequency, 93.5 mHz, was approximately 1×10^{-2} $/\sqrt{\text{Hz}}$.

Data Errors and Offline Error Correction

Three types of data error occurred in the data-handling framework of SWIM$_{\mu\nu}$. The errors were caused by a bug in the control software of SpaceCube2 and in the downlink communication from SDS-1 to the ground stations. Because of the errors, the data obtained from the detector were too dirty to be used for statistical analysis. To deal with this problem, we applied restoration processes to the data. The errors were successfully eliminated and the data were confirmed to be clean. Thus, this data error correction was vital to the whole experiment.

Search for Stochastic Gravitational Wave Background

The SGWB is a superposition of random waves that originate from astronomical sources such as superposition of indistinguishable sources, inflation or the vacuum phase transition in the very early Universe. Using our SWIM$_{\mu\nu}$ detector as a rotating TOBA, we set an upper limit for the low-frequency SGWB. Applying the frequency-upconversion technique, we achieved a frequency of about 18 mHz, which has never been used in the search for GWs with ground-based detectors. In addition, as mentioned above, the detector can sense forward and reverse polarization modes associated with its rotation. This is not only the first demonstration of a spaceborne GW detector but also the first attempt to conduct GW observations that are only performable in space.

Ninety-five percent upper limits for the two polarization modes of the SGWB were set. The observation frequency and bandwidth were 18 mHz and 4.5 mHz, respectively. We used two statistical methods (frequentist and Bayesian) to calculate the upper limits while considering only the statistical errors. Taking the systematic error as 200% and choosing the frequentist approach to acquire better upper limits, we obtained upper limits of 1.7×10^{31} for the forward mode and 3.1×10^{30} for the reverse mode. Since SWIM$_{\mu\nu}$ is a small prototype detector, it has low sensitivity compared with large ground-based apparatus. However, these are the first results for the forward and reverse modes of the circular polarization of GWs. The two upper limits for the two modes are not in agreement with each other owing to the different sensitivities at the corresponding observation frequencies.

Future Prospects

SWIM$_{\mu\nu}$ has successfully been used to demonstrate three approaches to carrying out low-frequency GW observations: spaceborne detectors, the TOBA and the frequency-upconversion technique. SWIM$_{\mu\nu}$ is also technically important since it was used to verify spaceborne equipment that will be utilized in future space-based GW missions. Note that a scientific mission was conducted using SWIM$_{\mu\nu}$ onboard a small-scale satellite which generally have extremely limited resources.

As future prospects based on this experiment, the sensitivity of the TOBA and the performance of large-scale scientific experiments using a rotating TOBA were discussed in Chapter 8. It is expected that GWs from black-hole binaries with a solar mass of 10^4—10^7 can be detected using a spaceborne large-scale TOBA with test masses of length 4 m. The rotating TOBA has the potential to become an effective tool for low-frequency GW astronomy in the future. We expect that the technical and operational experience obtained from $\mathrm{SWIM}_{\mu\nu}$ will be utilized as a driver for future space-based GW telescopes.

9.2 Conclusion

A novel methodology for observing low-frequency GWs called the frequency-upconversion technique was proposed. To realize this technique, a spaceborne rotating torsion-bar antenna, $\mathrm{SWIM}_{\mu\nu}$, was developed and successfully operated in orbit. By analyzing data obtained from the detector, upper limits for the two polarization (forward and reverse) modes of the stochastic GW background were set. This type of SGWB search was conducted for the first time using our detector. In addition, $\mathrm{SWIM}_{\mu\nu}$ is the first GW detector to be operated in orbit. Moreover, it was used to demonstrate devices for future satellite missions. We believe that these advances will pave the way for space-based low-frequency GW observations in the future.

Appendix A

Offline Data Correction

In this appendix, the data errors mentioned in Chapter 6 and the offline data correction processes are described in detail. The origins and processes, which corresponds to the three types of errors, i.e., packet loss, bit flipping and a software bug, are explained.

A.1 Preprocess

We reconstructed the level-1 data from the received files as a preprocess. As described in Figure 6.2, the experimental data obtained in each operation are stored temporarily in the extended memory in the ECU. After the experimental operation, the data were downloaded in a fragmentary fashion via individual satellite passes, which took from two weeks to a month. About five to ten paths were needed to download all the experimental data. The data files sent to us from JAXA's satellite operation division were distinct from each other. We have the information on memory address in the extended memory for each file. Then we obtained a complete data file by lining up the fragmented files. We defined the fragmented data as level-0 data, and the pieced together data as level-1. Since we performed a double download, we acquired two files, which are indicated as Data A1 and Data B1 in Figure 6.3.

A.2 Packet Loss

As the first restoration process, we dealt with the loss of packets. In the downlink, which involved radio communication from the satellite to the ground station distant from several hundred km away, some packets were lost owing to the instability of the link. We

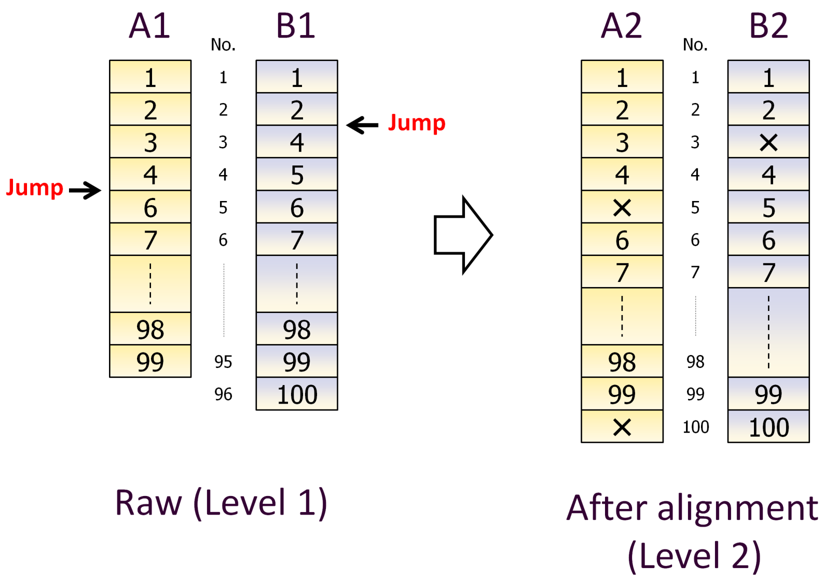

Figure A.1: Conceptual figure of the alignment process. The left and right sides show the sequence of level-1 and level-2 data, respectively. The sequence of numbers in the center are the indices from the heads of the packets. The "X" marks on the right represent the dummy data.

obtained two datasets since we conducted a double download of the experimental data. Using these datasets, we examined which packets are lost or not by (i) comparing the contents of the two datasets and (ii) checking the counters in the packets. The aligned data are referred to level-2 data, and were used for the next process of data recovery .

A.2.1 Alignment

How we aligned the data is shown in Figure A.1. When a jump of the counter is found in a level-1 dataset, the analysis program searches for the matching packet in the other dataset. As the lost packets are filled with dummy data, the correct order of the dataset is recovered, as shown on the right side of Figure A.1. For example, in Figure A.1 the correct length of the data is 100. However, we have shorter datasets with lengths of 95 for the Dataset A and 96 for the Dataset B. Note that we cannot identify the position of each packet by only checking the counter because in some cases it is contaminated by a bit flip and it may not have the correct value. This is why we needed to compare the two datasets to find the lost packets.

Figure A.2 shows an example of searching for lost packets. It was found that 11 packets

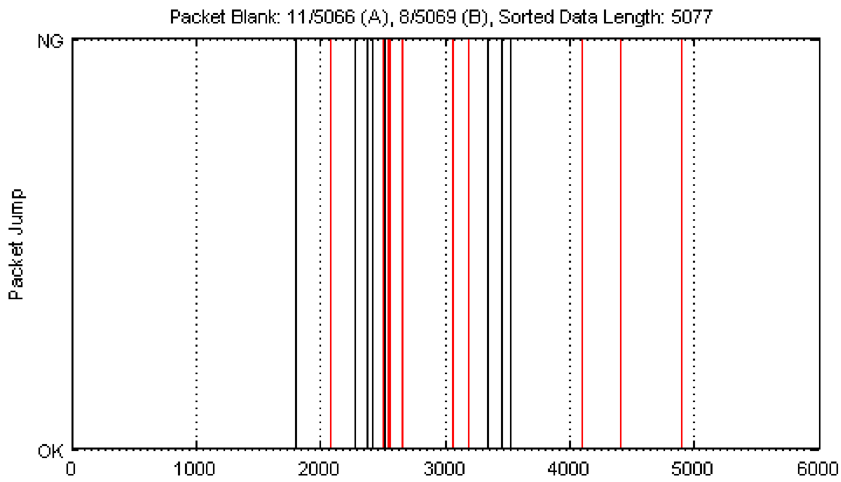

Figure A.2: Example of search for lose packets. The horizontal axis represents the number of packets, while the vertical axis indecates whether a packet is lost (NG) or not (OK). The black line represents Dataset A and the red line represents Dataset B.

in Dataset A and 8 packets in Dataset B were lost. The total number of the packets was found to be 5077. In addition, no packets were lost in both datasets. This means that we could recover all the data using these two datasets. The numbers of lost packets in individual operations are shown in Table A.1.

A.3 Bit Flip

In the second stage of error correction, bit flipping due to the radio communication link between the satellite and ground stations is treated. The data in the extended memory are downloaded to the ground twice. Thus, we have two datasets containing data errors. However, the bit flips of the two datasets are not correlated with each other. The frequency of bit flips is low (approximately 0.03% of the total number of bits). Thus, we can detect bit flips by comparing the two datasets. Also, the data packets have a CRC code so that the errors can be detected during the serial COM. We utilize the CRC code to detect and correct bit flips. We call our method the “double download” method.

A.3.1 Characteristics of Bit Flip

The characteristics of the bit flips are as follows:

Table A.1: Results of packet loss detection. The numbers of lost packets in the two datasets are shown for individual operations. Operation ID represents the date of the experiment as YYMMDD. The total length is the length after reconstruction. The numbers of lost packets in Datasets A and B are counted.

Operation ID	Total Length	Lost in Dataset A	Lost in Dataset B
100120_0236	1837	3	4
100121_0145	808	1	43
100224_0409	1159	0	0
100225_0443	1437	12	8
100325_0337	1973	11	5
100326_0408	2689	12	17
100617_0800	2596	4	5
100715_0730	5077	11	8

- A bit flip occurs as a burst. The length of the bit flips is in the range of 1 to about 30 bits.
- The frequency of the bit flip is related to the ground station where the data transfer operation is conducted. Indeed, we confirmed that fewer errors were detected when the data was downloaded via the KSAT station located in north Norway. In contrast, more errors were found in data downloaded via a station in Japan (for example, Okinawa).
- The greater the number of bit flips occurring in the data, the greater the packet loss in the data. This implies that the instability of the radio communication causes both types of problems.

A.3.2 Recovery

We used the double download method, in which two data are compared and checked for recovery. The simplest and the most efficient way to deal with bit flip errors is to perform a "triple download", i.e., to read the data three times and settle the correct value on a majority vote. In particular, when the frequency of the error is low as in our case, the triple download is very powerful to recover the correct data. SWIM$_{\mu\nu}$ is only one of the four main missions of SDS-1, and SDS-1 is also a piggyback satellite, which has limited operation resources. Since we wished to send as much experimental data to the ground

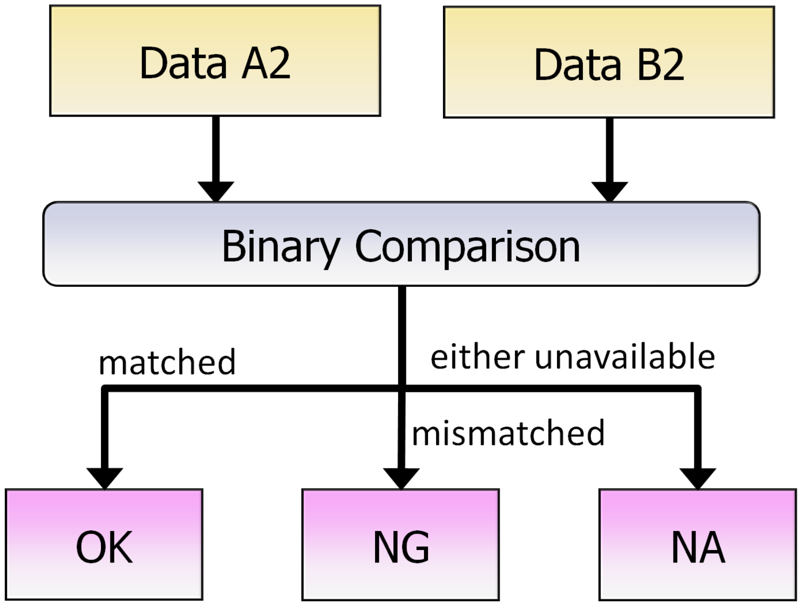

Figure A.3: Schematic of binary comparison. The boxes labeled “OK”, “NG” and “NA” represent that the datasets are classified and labeled with these labels.

as possible, we decided to do perform the double download method and reconstruct the correct data by a more complicated process.

The recovery process used to recover the correct data consists of the following two steps:

1. Compare the two datasets expressed as binary data.

2. Check the CRC codes.

Hereafter we explain the step by step process in detail .

Binary Comparison

The two datasets expressed as binary data are compared. Figure A.3 is a schematic of this comparison. When a packet of Dataset A matches that in Dataset B, the combination is labeled “OK”. In contrast, it is labeled “NG” when a mismatch is detected. In the case of packet loss in either dataset, the label “NA” is given.

CRC Check

In this step, the CRC code added to each mission packet is used to detect burst errors. The relation between the downlink telemetry and mission data packets is shown in

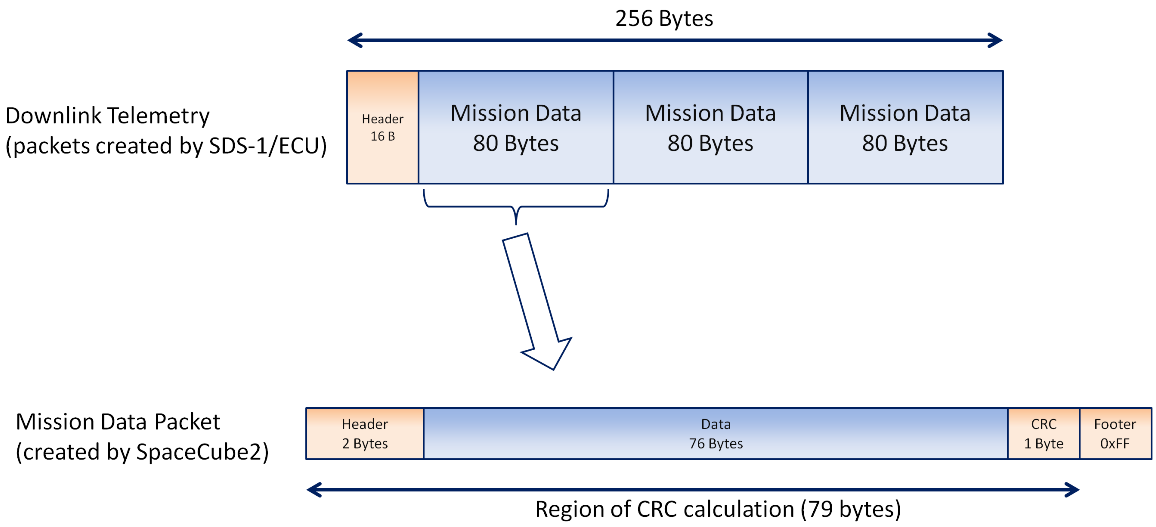

Figure A.4: Downlink telemetry and mission data packet. In the top, composition of the downlink telemetry from the satellite to the ground is shown. Organization of the mission data packet, which is contained in the downlink telemetry, is shown in the bottom.

Figure A.4. Communication protocol of serial COM between the ECU and SpaceCube2 is specified with a protocol definition document [75]. Figure A.4 describes this communication format. Each mission data packet should be 80 bytes long. It should contain a header (2 bytes), 76 bytes of data, the CRC code and a footer (fixed to 0xFF) in order, as shown at the bottom of Figure A.4. SpaceCube2 calculates and adds the CRC code with a calculation range of 79 bytes from the beginning of the packet.

We use 7-bit CRC codes, for which the generating polynomial is

$$X^7 + X^6 + X^1 + 1. \tag{A.1}$$

This contains a factor of $X^1 + 1$, meaning that this CRC can detect a burst error with an odd length in all cases.

When the ECU receives a mission packet, it checks that the CRC code is correct. If it is not correct, the ECU rejects the packet and requests SpaceCube2 to send the packet again. Thus, all mission packets stored in the ECU have correct CRC codes. We make use of this code to detect errors in the downlink telemetry. If a bit flip occurs in the downlink, the CRC code of the mission data packet and the calculated value will differ. This mismatch means that there is an error in the downlink (more precisely, somewhere after the serial COM).

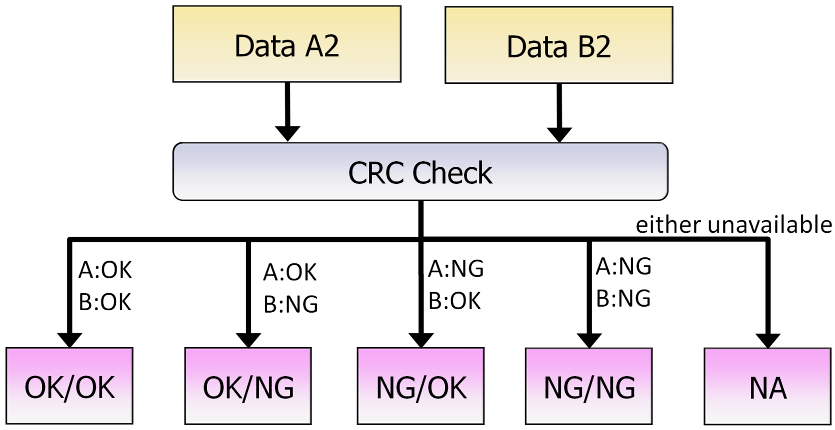

Figure A.5: Schematic of CRC check. CRC check is applied to level-2 data. Top box shows mission data of set A OR set B. According to the results, "OK", "NG" or "NA" flag is labeled for each mission packet.

We show the CRC checking process in Figure A.5. For each mission data packet, the consistency between the CRC code in the data packet and the value calculated from the packet is checked. When the values match, the data packet is labeled with an "OK" flag, when they do not match, it is labeled with an "NG" flag. and, similarly to before, when either packet is lost, the data packet is labeled with an "NA" flag.

Since this process is carried out for both datasets, we obtain the direct product of the two results, i.e. the mission packet is divided into 8 cases: (OK, OK), (OK, NG), (NG, OK), (OK, NA), (NA, OK), (NG, NA), (NA, NG) and (NA, NA). Note that there was no instance of both packets being lost, meaning that the (NA, NA) case did not arise.

Recovery

Using the information from the comparison and CRC check above, we next attempt to select clean data or recover the correct values. Figure A.6 is a flowchart of this recovery operation. For a single data packet, the following sequence is carried out:

1. Packet comparison: The process depend on the result of the packet comparison, i.e., "OK", "NG" or "NA".

2. (Result of packet comparison is "NA"): This label means that one of the two data is lost. Thus, the results of the CRC check of the other dataset determines the process. If it is "OK", we accept the data. On the other hand, if it is "NG", we correct the packet manually. That case corresponds to (1) in Figure A.6.

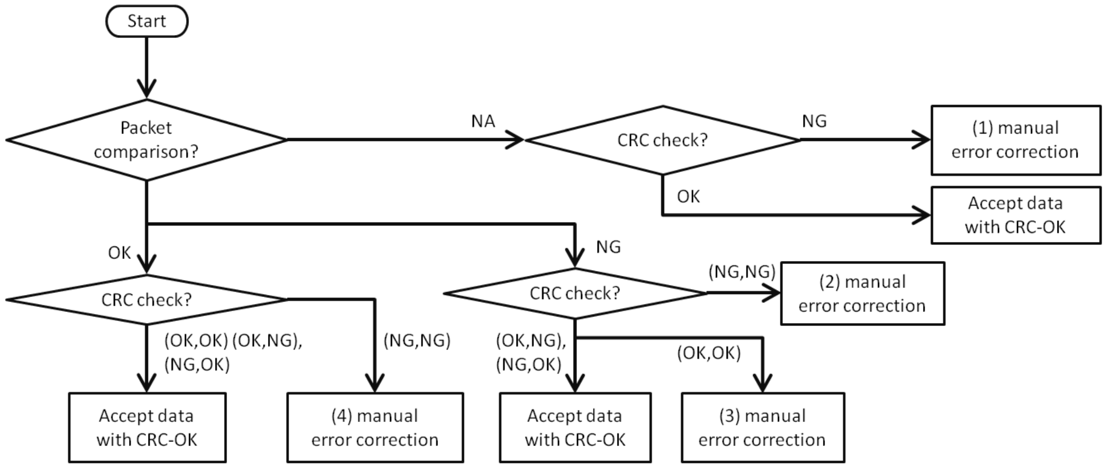

Figure A.6: Flowchart of the recovery process of the bit flips. Rectangles show the treatment for each pair of data packets.

3. (Result of packet comparison is "NG"): Here the two packets in Dataset A and B are different. There are three possible results of the CRC check: i) (OK, NG) or (NG, OK). This is the case that only one of the packets has a bit flip. Thus, we accept the packet that the label of the CRC check is "OK". ii) (NG, NG). This is the case that both packets contain a bit flip, thus the both packets was labeled by "NG". We identify and correct the bit flips manually. This case corresponds to (2) in Figure A.6. iii) (OK, OK). This is a strange case because the two packets have different binary expressions but the CRC checks are both OK. We assume that this occurs when the CRC code cannot detect a bit flip. This error is manually fixed. This corresponds to (3) in Figure A.6.

4. (Result of packet comparison is "OK"): This label means that the two packets are exactly the same. Therefore, the result of CRC check should be (OK, OK) or (NG, NG). In the case of (OK, OK), there is no problem in the packets and we take it as a correct data. Otherwise, if it is (NG, NG), manual error correction is needed. This can happen when bit flips occur at exactly the same bits in the two data packets. This corresponds to (4) in Figure A.6.

A.3.3 Manual Error Correction

In the above process, some packets require manual error correction. Table A.3.3 summarizes these errors among the data obtained in the experiments. Here we explain how we found a bit flip in the packets and fixed it.

(1) Packet Comparison: "NA" and CRC check: (NG, NA)

In this case, one packet containing a bit flip exists and the other packet is lost. Therefore, we have to search for the bit flip manually by performing the following steps:

- Data are dealt with byte by byte. The data contained in the packets are 16-bits data; thus, the higher 8 bits and lower 8 bits are treated separately.
- Find an abnormal behavior in the data. Since the bit flip occurs in consecutive bits, the error can be distinguished by checking if there is a value distant from the expected range of the data.
- For each error candidate, the CRC code for the packet is recalculated and checked to determine whether it is the same as that in the packet. If there are several possible patterns of errors, we take the pattern that the recalculated CRC code matches the correct CRC code in the packet.

An example of a manual search for a bit flip is presented in Figure A.7. If we cannot find a bit flip in the first step, we abandon the search for it. This is because failing to find a bit flip does not deteriorate the detector sensitivity.

(2) Packet Comparison: "NG" and CRC check: (NG, NG)

Here the two packets do not match in their binary representations and the results of the two CRC checks are both NG. This occurs when both packet A and packet B have a bit flip. Thus, we find binary mismatches at two locations. We can recover the correct data by determining which packets are correct in each bit flip. In addition, the CRC code is rechecked to ensure that this method is appropriate.

(3) Packet Comparison: "NG" and CRC check: (OK, OK)

In this case, the two packets do not match in their binary representations; however, the two labels for the CRC checks are both "OK". Then we have two possibilities; (i) One of the packets contains a bit flip that does not change the value of the CRC code, (ii) The footer of the packet has a bit flip. Because the footer is out of the range of the CRC check,

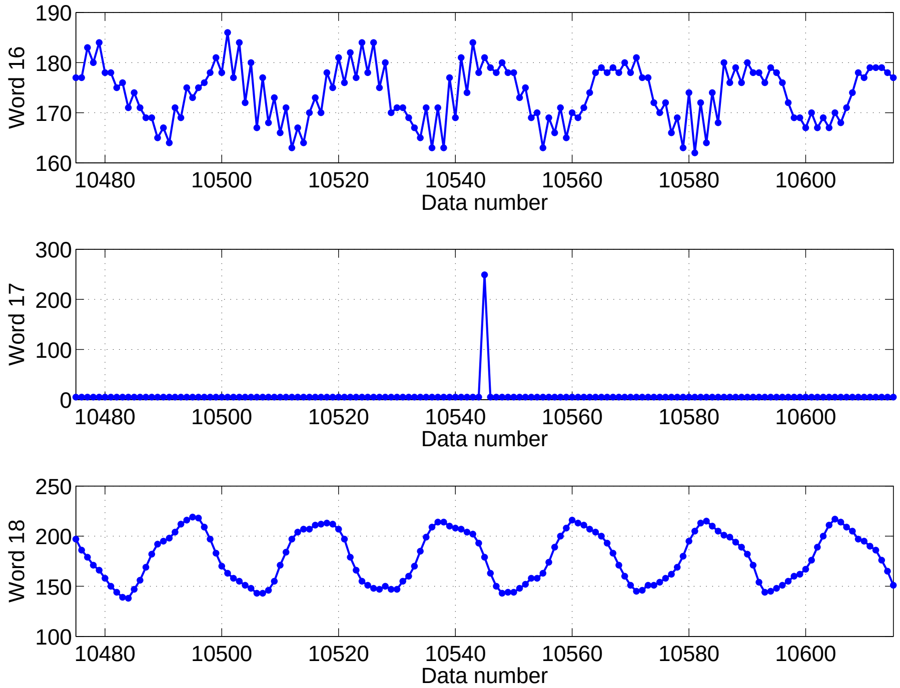

Figure A.7: Example of manual error search for a bit flip. The horizontal axis represents the relative number of data. The vertical axes show values of data. Here we want to search for an error with index (position) 10545. In this plot, 70 previous and 70 following packets are plotted. From the top, the three plots show the values of the 16th, 17th and 18th bytes from the beginning of the packet.

the result may be "OK". For case (ii), the bit flip is trivial to correct because of the fixed footer (0xFF).

Thus, we consider the case (i). Here a bit mismatch is found in the pair of the packets at one point; thus, we investigate which packet is correct. Similar process to find and fix the bit flip in the previous manual correction is performed; The CRC code for the packet are recalculated for each two cases, i.e, the case that Dataset A is correct and that the Dataset B is correct. The calculated CRC codes are checked to determine whether it is the same as that in the packet.

(4) Packet Comparison: "OK" and CRC check: (NG, NG)

Although the two packets are exactly the same, both packets is labeled "NG" for the check of the CRC code in this case. Here it is possible that exactly the same bit flip has occurred coincidently. Among the data obtained in experimental operations, only one pair fitted this case. Checking the packet manually as the case (3), we could not find any

Table A.2: Summary of manually corrected errors. For the eight operations, the total length and the number of packets requiring manual corrections of types (1)—(4) are shown.

	CMP: CRC:	NA NG	NG (OK, OK)	NG (OK, OK)	OK (NG, NG)
Operation ID	Total	(1)	(2)	(3)	(4)
100120_0236	1837	5	1	6	0
100121_0145	808	3	0	1	0
100224_0409	1159	0	0	0	0
100225_0443	1437	3	2	7	0
100325_0337	1973	2	1	5	0
100326_0408	2689	6	1	6	0
100617_0800	2596	1	2	4	0
100715_0730	5077	1	15	11	1

significant deviation in the data. Thus, we regard this case as not having an adverse effect on the detector and take the data as it is.

A.3.4 Remaining Errors

Errors remained in the reconstructed datasets. A summary of these errors is shown in Table A.3. In total, three packets were overlooked in the correction. It was confirmed that none of these packets had significant variation from nearby data or deteriorated the sensitivity of the detector.

A.4 Software Bug

Finally, errors originating from a bug in the onboard software in SpaceCube2 were dealt with. The data were averaged by the onboard software in SpaceCube2. In this averaging process, a bug contaminated the data; each value stored in the data recorder in SpaceCube2 after averaging was incorrect. Since the effect of this error is not random, we estimated the correct value of the data from the contaminated data.

Table A.3: Summary of remaining errors. The total number of overlooked packets in individual operations and their types are shown.

Operation ID	Overlooked Packets	Type
100120_0236	0	
100121_0145	1	(1)
100224_0409	0	
100225_0443	0	
100325_0337	0	
100326_0408	0	
100617_0800	0	
100715_0730	2	(1), (4)

A.4.1 Origin and Effect of Software Bug

Here we explain how this bug affected the data. In SpaceCube2 the data were averaged as

$$V_{\mathrm{out}} = \sum_{i=1}^{\mathrm{N}} V(i)/\mathrm{N}, \tag{A.2}$$

where V_{out} is the output of this averaging process, $V(i)$ is the input dataset and N is the downsampling rate, which is selected to be from 1 (no averaging) to 512 (strong averaging) to meet the requirement of the observation and limitations on the amount of the downloadable data. For most of the experimental observations N was 4 or 32.

To express a value of experimental data, we used the "signed 16-bit integer with bias" representation. This is shown on the left of Figure A.8. In a signed integer, the most significant bit (MSB) of the binary data represents its sign; when MSB is 1, the data has a negative value. As shown in Figure A.8, The bit order is changed in the signed integer, i.e., as the binary representation of the data increases, corresponding value of the data also increases. Here a bias of 2^{15} is added to the normal signed integer so that the least value ("1000 0000 0000 0000") should represent 0. For examples, the binary value "0111 1111 1111 1111" is the largest value, which is equivalent to $2^{15} - 1$, and "1000 0000 0000 0000" correspond to zero. On the other hand, an "unsigned integer" has a simpler expression. There is no sign bit; therefore, the binary "0000 0000 0000 0000" correspond to a value of zero and "1111 1111 1111 1111" represents the largest value of $2^{15} - 1$.

For correct averaging, data should be converted to a decimal or equivalent linear representation (for example, binary) before the processing. The origin of the bug was the use of an incorrect expression, i.e., a signed integer with bias was mistaken for an unsigned

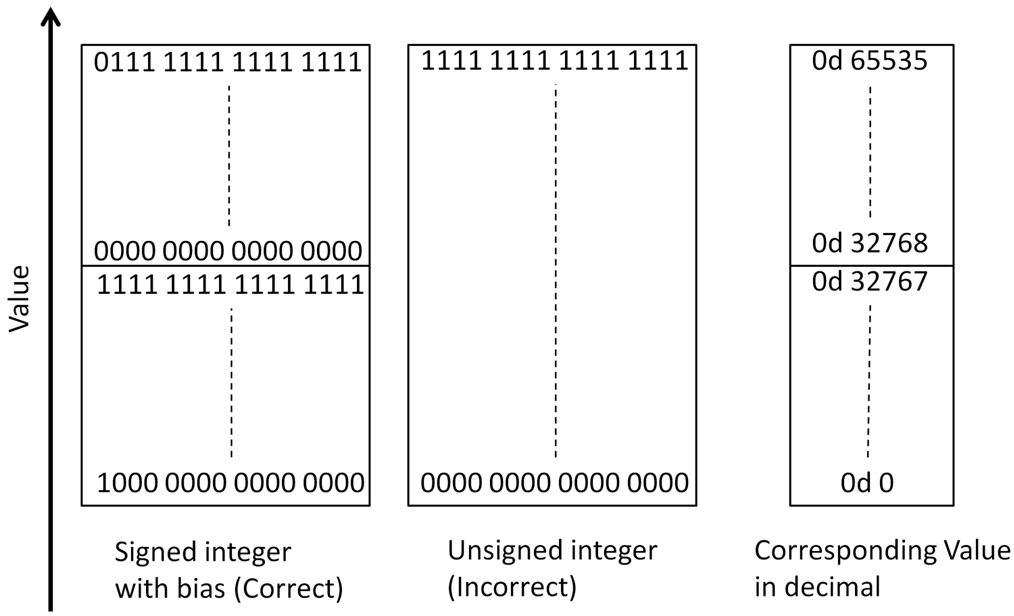

Figure A.8: Numerical representation used in SpaceCube2. The correct representation (signed integer with bias) is shown on the left. In the center, the unsigned integer used in the bug is shown. Numbers on the right are the corresponding values in decimal.

integer. This result in the interpreted value differing by a fixed value. For example, the value 32767 in decimal is “1111 1111 1111 1111” as a signed integer with bias. However, it is expressed as “0111 1111 1111 1111” as an unsigned integer. The signed integer “0111 1111 1111 1111” is interpreted as 65535, a difference of 2^{15} (= 32768) from the correct value.

Here we consider the effect of the error in the numerical expression more quantitatively. Let X be a 16-bit binary and $V(X)$ is the corresponding value in decimal. $V_1(X)$ and $V_2(X)$ are values expressed as a signed integer and unsigned integer, respectively. Then the relation between $V_1(X)$ and $V_2(X)$ should be

$$V_2(X) = \begin{cases} V_1(X) + \frac{\mathrm{FS}}{2} & (X \in A) \\ V_1(X) - \frac{\mathrm{FS}}{2} & (X \in B) \ , \end{cases} \tag{A.3}$$

where FS denotes the full scale of the value (here FS $= 2^{16}$). Regions A and B are defined as

$$A = [32768 \leq V(X) \leq 65535] \ , \tag{A.4}$$

and

$$B = [0 \leq V(X) \leq 32767] \ . \tag{A.5}$$

In other words, the most significant bit of X in region A is 1 and that of X in region B is 0. Considering an averaging of N data, we obtain the relation:

$$\frac{\sum_i V_2(X_i)}{\mathrm{N}} = \frac{\sum_i V_1(X_i)}{\mathrm{N}} + \frac{\mathrm{FS}}{2} - \frac{\mathrm{FS}}{\mathrm{N}} k \ . \tag{A.6}$$

Here k is the number of the data in region B and the other $N - k$ data are in region A. Thus, the incorrect average A_F is expressed in terms of the correct average A_T as

$$A_\mathrm{F} = A_\mathrm{T} - \frac{\mathrm{FS}}{\mathrm{N}} k, \tag{A.7}$$

because $A_\mathrm{F} = \sum_i V_2 - \mathrm{FS}/2$. In other words, the incorrect average differs from the correct average by an integral multiple of FS/N. This characteristic is utilized in the recovery process.

A.4.2 Recovery

As described in the previous section, the difference between the correct average and the incorrect average is not random but expressed as $\mathrm{FS/N} \times k$ with an integer k. Therefore, we can estimate the correct value from the incorrect average using this property. To restore the correct value, the following two assumptions are needed:

- The variance of the data is sufficiently small for the correct data to be within a range of FS/N, i.e., the signal from the detector has sufficiently low noise.
- The correct data is nearby the boundary between regions A and B. Otherwise, the error does not occur (k becomes zero).

Under these assumptions, we have the following criteria in the recovery process: (i) data near the boundary should not be corrected, (ii) data far from the boundary should be corrected as follows:

$$V_\mathrm{after} = V_\mathrm{before} + C \times \frac{\mathrm{FS}}{\mathrm{N}}. \tag{A.8}$$

Here V_after and V_before denote the value after the correction and before the correction, respectively. C is the estimated number of the data in the region B in the averaged N data. C is derived from this expression:

$$C = \left[\frac{V_\mathrm{before} - m}{\mathrm{N}} \right] \ , \tag{A.9}$$

Table A.4: Summary of downsampling rate for each experiment.

Operation ID	Downsampling rate
100120_0236	4
100121_0145	256
100224_0409	256
100225_0443	4
100325_0337	32
100326_0408	256
100617_0800	512
100715_0730	512

where $[\cdots]$ is the Gauss symbol. The value of m is chosen as the boundary between region A and region B.

Figure A.9 shows the "TAM1PS6" signal from pass "100224" as an example of this data recovery process. In this graph the full scale of the data is converted to a voltage, i.e., FS = 4.096 V, and the boundary between regions A and B is 2.048 V. The downsampling rate N in this case is 256; thus, FS/N = 0.016 V. This is sufficiently large because the signal typically fluctuates in a range of several mV. As shown in Figure A.9, the raw data fluctuate widely owing to the errors, but the correct data do not. The properness of this correction is confirmed by checking that this behavior of the corrected data agrees with that of other channels without the error. Table A.4 is a summary of the downsampling rate for each on-orbit experiment. After the same correction process was performed to the whole data obtained from the detector, we obtained the level-4 data, which were used in the observational analysis described in Chapter 7.

Limitation

This recovery method has a limitation. The average number, in other words, the downsampling rate, should be sufficiently small. Quantitatively, a signal should behave as

$$X_{\mathrm{RMS}}\left(f < \frac{f_s}{\mathrm{N}}\right) < \frac{\mathrm{FS}}{\mathrm{N}}, \tag{A.10}$$

where $X_{\mathrm{RMS}}(f < f_0)$ is the RMS amplitude of a signal with bandwidth f_0, and f_s is the sampling rate before averaging (here $f_s = 537.11$ Hz). We could recover the observational signals from SWIM$_{\mu\nu}$ since they have sufficiently low noise to meet this requirement. If the downsampling rate was much larger, we would not have been able to recover the correct data.

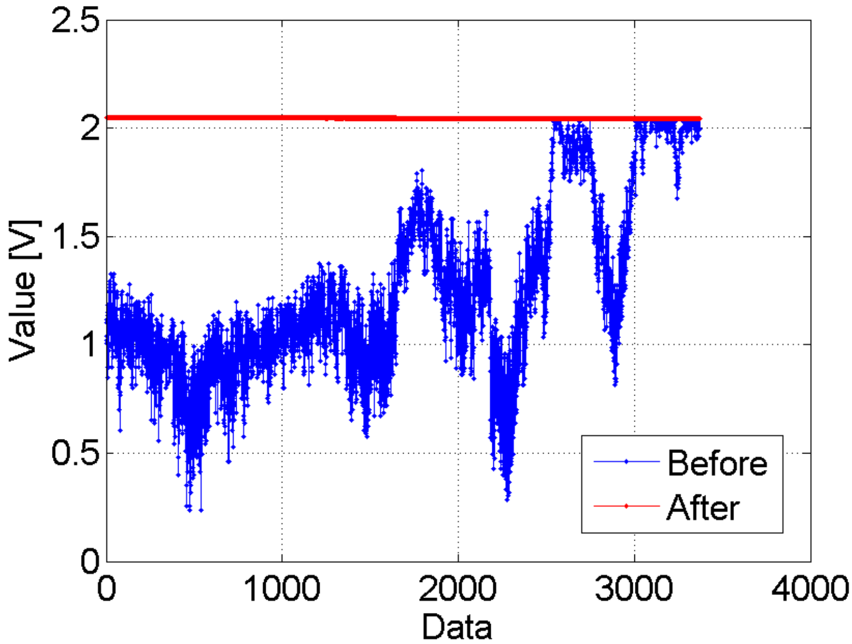

Figure A.9: Example of correction of software bug. The horizontal axis represents the number of data, while the vertical axis represents the value. Here the values are calibrated to the input voltage of ADCs; thus, full scale is 4.096 V. The blue dots with lines show the raw data before cleaning. The red curve shows the correct data after cleaning.

A.5 Justification of Correction Process

To justify the correction process presented in this appendix, we performed a simulation using the data. The simulation was as follows. We prepared the true data, i.e., corrected data without errors. Next, we randomly selected N data and replaced them with the mean value of the next and the previous data. This process simulated the errors and a correction process that replaces the mean value of the next data as an estimated value of the lost data.

We used 50 as N, out of 14976 packets of data and took the same simulation 100 times and averaged them. Figure A.10 shows the true data and the difference between the true and simulated data. Typically the difference is less than the absolute value of the true data by one order of magnitude. Figure A.11 shows the power spectrum of the true data and the simulated data. The differences of the power is approximately a tenth of that of the true data, thus, we confirm the arbitrariness in the correction process is not a problem in the data analysis.

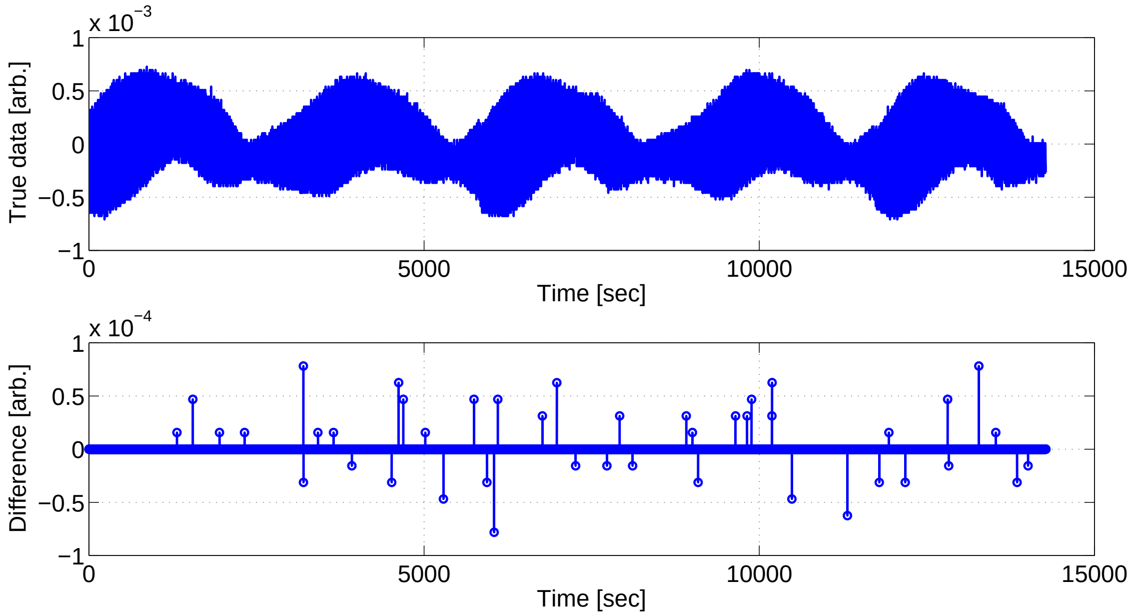

Figure A.10: Differences between the true data from the detector and the data recovered by the simulation.

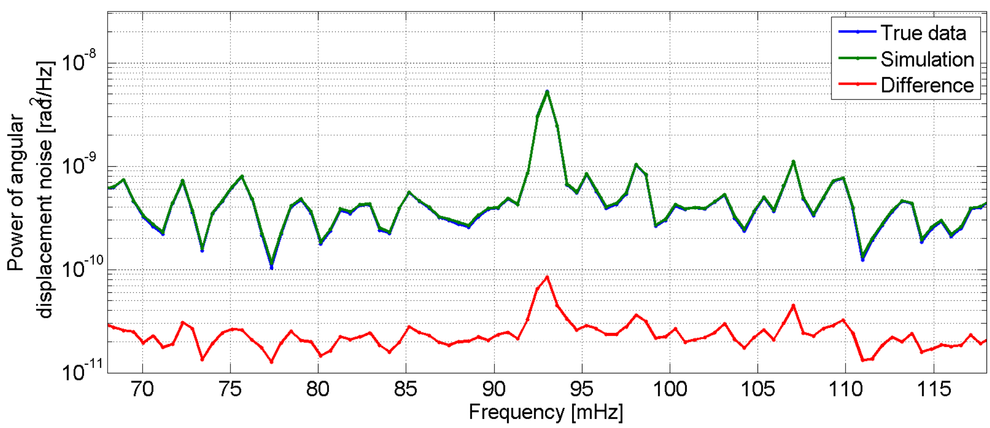

Figure A.11: Power spectra of the true data, simulated data and thier difference.

Bibliography

[1] A. Einstein, R.W. Lawson, R. Geroch, and D.C. Cassidy, *Relativity: The special and general theory* (Methuen & Co. Ltd. 36 Essex Street W.C. London, 1920).

[2] C.W. Misner, K.S. Thorne, and J.A. Wheeler, *Gravitation* (WH Freeman & co, 1973).

[3] S.A. Hughes, "Listening to the universe with gravitational-wave astronomy," Annals of Physics **303**, 142–178 (2003).

[4] S. Fairhurst, G.M. Guidi, P. Hello, J.T. Whelan, and G. Woan, "Current status of gravitational wave observations," General Relativity and Gravitation **43**, 387–407 (2011).

[5] J. Weber, "Evidence for discovery of gravitational radiation," Physical Review Letters **22**, 1320–1324 (1969).

[6] J. Abadie, BP Abbott, R. Abbott, M. Abernathy, T. Accadia, F. Acernese, C. Adams, R. Adhikari, P. Ajith, B. Allen, *et al.*, "Predictions for the rates of compact binary coalescences observable by ground-based gravitational-wave detectors," Classical and Quantum Gravity **27**, 173001 (2010).

[7] B.F. Schutz, "Fundamental physics with LISA," Classical and Quantum Gravity **26**, 094020 (2009).

[8] P. Amaro-Seoane, S. Aoudia, S. Babak, P. Binétruy, E. Berti, A. Bohé, C. Caprini, M. Colpi, N.J. Cornish, K. Danzmann, *et al.*, "eLISA: Astrophysics and cosmology in the millihertz regime," Arxiv preprint arXiv:1201.3621(2012).

[9] N. Seto, S. Kawamura, and T. Nakamura, "Possibility of direct measurement of the acceleration of the universe using 0.1 Hz band laser interferometer gravitational wave antenna in space," Physical Review Letters **87**, 221103 (2001).

[10] W.T. Ni, S. Shiomi, and A.C. Liao, "ASTROD, ASTROD I and their gravitational-wave sensitivities," Classical and Quantum Gravity **21**, S641 (2004).

[11] J.M. Hogan, D.M.S. Johnson, S. Dickerson, T. Kovachy, A. Sugarbaker, S. Chiow, P.W. Graham, M.A. Kasevich, B. Saif, S. Rajendran, *et al.*, "An atomic gravitational wave interferometric sensor in low earth orbit (AGIS-LEO)," General Relativity and Gravitation, 1–57(2011).

[12] Norikatsu Mio, **相対性理論** *(Theory of Relativity)*, 1st ed., SGC Library, Vol. 56 (Saiensu-sya, 2007) [in Japanese].

[13] A. Abramovici, W.E. Althouse, R.W.P. Drever, Y. Gürsel, S. Kawamura, F.J. Raab, D. Shoemaker, L. Sievers, R.E. Spero, K.S. Thorne, *et al.*, "LIGO: The laser interferometer gravitational-wave observatory," Science **256**, 325 (1992).

[14] BP Abbott, R. Abbott, R. Adhikari, P. Ajith, B. Allen, G. Allen, RS Amin, SB Anderson, WG Anderson, MA Arain, *et al.* (LIGO Scientific Collaboration), "LIGO: The laser interferometer gravitational-wave observatory," Reports on Progress in Physics **72**, 076901 (2009).

[15] BP Abbott, R. Abbott, TD Abbott, M. Abernathy, T. Accadia, F. Acernese, C. Adams, R. Adhikari, C. Affeldt, P. Ajith, *et al.* (LIGO Scientific Collaboration), "Implementation and testing of the first prompt search for electromagnetic counterparts to gravitational wave transients," Arxiv preprint arXiv:1109.3498(2011).

[16] M. Punturo, M. Abernathy, F. Acernese, B. Allen, N. Andersson, K. Arun, F. Barone, B. Barr, M. Barsuglia, M. Beker, *et al.*, "The Einstein Telescope: a third-generation gravitational wave observatory," Classical and Quantum Gravity **27**, 194002 (2010).

[17] B. Sathyaprakash, M. Abernathy, F. Acernese, P. Andersson, K. Arun, F. Barone, B. Barr, M. Barsuglia, M.B.N. Beveridge, S. Birindelli, *et al.*, "Scientific Potential of Einstein Telescope," Arxiv preprint arXiv:1108.1423(2011).

[18] J. Weber, "Gravitational radiation experiments," Physical Review Letters **24**, 276–279 (1970).

[19] H. Hirakawa, K. Narihara, and M.K. Fujimoto, "Theory of antennas for gravitational radiation," Journal of the Physical Society of Japan **41**, 1093–1101 (1976).

[20] K. Narihara and H. Hirakawa, "Gravitational radiation detectors at 145 Hz," Japanese Journal of Applied Physics **15**, 833–842 (1976).

[21] K. Oide, H. Hirakawa, and M.K. Fujimoto, "Search for gravitational radiation from the Crab pulsar," Physical Review D **20**, 2480 (1979).

[22] D.R. Lorimer and M. Kramer, *Handbook of pulsar astronomy*, Vol. 4 (Cambridge University Press, 2005).

[23] RT Edwards, GB Hobbs, and RN Manchester, “TEMPO2, a new pulsar timing package–II. The timing model and precision estimates,” Monthly Notices of the Royal Astronomical Society **372**, 1549–1574 (2006).

[24] G.B. Hobbs, M. Bailes, NDR Bhat, S. Burke-Spolaor, D.J. Champion, W. Coles, A. Hotan, F. Jenet, L. Kedziora-Chudczer, J. Khoo, *et al.*, “Gravitational-wave detection using pulsars: status of the Parkes Pulsar Timing Array project,” Publications of the Astronomical Society of Australia **26**, 103–109 (2009).

[25] F. Jenet, LS Finn, J. Lazio, A. Lommen, M. McLaughlin, I. Stairs, D. Stinebring, J. Verbiest, A. Archibald, Z. Arzoumanian, *et al.*, “The North American Nanohertz Observatory for Gravitational Waves,” Arxiv preprint arXiv:0909.1058(2009).

[26] R.D. Ferdman, R. Van Haasteren, C.G. Bassa, M. Burgay, I. Cognard, A. Corongiu, N. D’Amico, G. Desvignes, J.W.T. Hessels, G.H. Janssen, *et al.*, “The European Pulsar Timing Array: current efforts and a LEAP toward the future,” Classical and Quantum Gravity **27**, 084014 (2010).

[27] G. Hobbs, A. Archibald, Z. Arzoumanian, D. Backer, M. Bailes, NDR Bhat, M. Burgay, S. Burke-Spolaor, D. Champion, I. Cognard, *et al.*, “The International Pulsar Timing Array project: using pulsars as a gravitational wave detector,” Classical and Quantum Gravity **27**, 084013 (2010).

[28] RN Manchester, “Pulsar Timing Arrays and their Applications,” Arxiv preprint arXiv:1101.5202(2011).

[29] A.J. Farmer and E.S. Phinney, “The gravitational wave background from cosmological compact binaries,” Monthly Notices of the Royal Astronomical Society **346**, 1197–1214 (2003).

[30] C. Cutler and J. Harms, “Big Bang Observer and the neutron-star-binary subtraction problem,” Physical Review D **73**, 042001 (2006).

[31] N. Seto, “Demagnified gravitational waves from cosmological double neutron stars and gravitational wave foreground cleaning around 1 Hz,” Physical Review D **80**, 103001 (2009).

[32] E. Howell, T. Regimbau, A. Corsi, D. Coward, and R. Burman, "Gravitational wave background from sub-luminous GRBs: prospects for second-and third-generation detectors," Monthly Notices of the Royal Astronomical Society(2011).

[33] T. Hiramatsu, K. Kotake, H. Kudoh, and A. Taruya, "Gravitational wave background from neutrino-driven gamma-ray bursts," Monthly Notices of the Royal Astronomical Society **364**, 1063–1068 (2005).

[34] Y. Suwa, T. Takiwaki, K. Kotake, and K. Sato, "Gravitational wave background from population III stars," The Astrophysical Journal Letters **665**, L43 (2007).

[35] R. Saito and J. Yokoyama, "Gravitational-wave background as a probe of the primordial black-hole abundance," Physical Review Letters **102**, 161101 (2009).

[36] R. Saito and J. Yokoyama, "Gravitational-Wave Constraints on the Abundance of Primordial Black Holes," Progress of Theoretical Physics **123**, 867–886 (2010).

[37] S. Kuroyanagi, T. Chiba, and N. Sugiyama, "Prospects for direct detection of inflationary gravitational waves by next generation interferometric detectors," Physical Review D **83**, 043514 (2011).

[38] C. Caprini, R. Durrer, T. Konstandin, and G. Servant, "General properties of the gravitational wave spectrum from phase transitions," Physical Review D **79**, 083519 (2009).

[39] R. Easther, J.T. Giblin Jr, and E.A. Lim, "Gravitational wave production at the end of inflation," Physical Review Letters **99**, 221301 (2007).

[40] M. Ando, K. Ishidoshiro, K. Yamamoto, K. Yagi, W. Kokuyama, K. Tsubono, and A. Takamori, "Torsion-Bar Antenna for Low-Frequency Gravitational-Wave Observations," Physical Review Letters **105**, 161101 (2010).

[41] Hiromasa Hirakawa, **相対論** *(Relativity)*, 2nd ed. (Kyoritsu Shuppan, 1986) [in Japanese].

[42] A. Araya, W. Morii, H. Hayakawa, A. Takamori, T. Uchiyama, M. Ohashi, I. Yamada, S. Telada, and S. Takemoto, "Broadband observation with laser strainmeters and a strategy for high resolution long-term strain observation based on quantum standard," J. Geod. Soc. Japan **53**, 81–97 (2007).

[43] VB Braginsky and VS Nazarenko, "On the heterodyne method of detecting gravitational waves (Mathematical model of heterodyne method of detecting gravitational waves)," in *JPL Proc. of the Conf. on Exptl. Tests of Gravitation Theories p 45-46* (1971).

[44] Wataru Kokuyama, **衛星搭載用ねじれ型重力波検出器の開発** *(Development of space-borne torsion-bar gravitational wave detector)*, Master's thesis, The University of Tokyo (2009), [in Japanese].

[45] Hamamatsu Photonics K.K., *Infrared LED L2204/L2402/L3458 series*, data sheet, `http://jp.hamamatsu.com/resources/products/ssd/pdf/l2204_etc_kled1031e03.pdf`.

[46] Hamamatsu Photonics K.K., *Si photodiodes*, data sheet, `http://jp.hamamatsu.com/resources/products/ssd/pdf/s5627-01_etc_kspd1025e04.pdf`.

[47] T. Takahashi, T. Takashima, S. Kuboyama, M. Nomachi, Y. Kasaba, T. Tohma, H. Hihara, S. Moriyama, and T. Tamura, "SpaceCube 2–An Onboard Computer Based on SpaceCube Architecture," in *International SpaceWire Conference 2007* (2007) pp. 17–19.

[48] SM Parkes and P. Armbruster, "SpaceWire: a spacecraft onboard network for real-time communications," in *Real Time Conference, 2005. 14th IEEE-NPSS* (IEEE, 2005) pp. 6–10.

[49] T. Yuasa, W. Kokuyama, K. Makishima, K. Nakazawa, M. Nomachi, H. Odaka, M. Kokubun, T. Takashima, T. Takahashi, I. Fujishiro, *et al.*, "SpaceWire/RMAP-based Data Acquisition Framework for Scientific Instruments: Overview, Application, and Recent Updates," in *International SpaceWire Conference 2010* (2010).

[50] T. Takahashi, K. Mitsuda, R. Kelley, F. Aharonian, F. Akimoto, S. Allen, N. Anabuki, L. Angelini, K. Arnaud, H. Awaki, *et al.*, "The Astro-H mission," Arxiv preprint arXiv:1010.4972(2010).

[51] H. Saito, S. Sawai, S. Sakai, S. Fukuda, and K. Kitade, "A series of small scientific satellite with flexible standard bus," Acta Astronautica **65**, 1345–1359 (2009).

[52] Japan Aerospace Exploration Agency, "SDS-1 (Small Demonstration Satellite-1)," (2008), european Space Agency eoPortal directory, `http://www.eoportal.org/directory/pres_SDS1SmallDemonstrationSatellite1.html`.

[53] Y. Nakamura, K. Shinoda, H. Kawara, K. Hirako, and E. Hashimoto, "JAXA's Small Demonstration Satellite Program and Development and Operation of SDS-1," IEICE Technical Report: SANE **109**, 41–46 (2009).

[54] Y. Nakamura, K. Kawashima, K. Yamamoto, K. Shinoda, H. Kawara, K. Hirako, and H. Hashimoto, "Flight result of SDS-1," (Proceedings of the 4S Symposium Small Satellites, Systems and Services, Madeira, 2010) 2010.

[55] S.I. Takayama, K. Yoshihara, and H. Hashimoto, "Development of Attitude Sensors of Small Satellite," Uchu Kagaku Gijutsu Rengo Koenkai Koenshu (CD-ROM) **50**, 2E01 (2006).

[56] EJ Post, "Sagnac effect," Reviews of Modern Physics **39**, 475 (1967).

[57] Japan Aerospace Exploration Agency, "JAXA Digital Archives," `http://jda.jaxa.jp/`.

[58] Charles Rino, "Satellite Orbit Computation," (2010), m-files: Matlab Central file exchange service, `http://www.mathworks.com/matlabcentral/fileexchange/28888-satellite-orbit-computation&watching=28888`.

[59] International Association of Geomagnetism and Division-V Aeronomy, "International Geomagnetic Reference Field, 11th Generation," (2010), provided by coefficients, `http://www.ngdc.noaa.gov/IAGA/vmod/igrf.html`.

[60] E. Komatsu, KM Smith, J. Dunkley, CL Bennett, B. Gold, G. Hinshaw, N. Jarosik, D. Larson, MR Nolta, L. Page, *et al.*, "Seven-Year Wilkinson Microwave Anisotropy Probe (WMAP) Observations: Cosmological Interpretation," The Astrophysical Journal Supplement Series **192**, 18 (2011).

[61] M. Maggiore, "Gravitational wave experiments and early universe cosmology," Physics Reports **331**, 283–367 (2000).

[62] R.H. Cyburt, B.D. Fields, K.A. Olive, and E. Skillman, "New BBN limits on physics beyond the standard model from 4He," Astroparticle Physics **23**, 313–323 (2005).

[63] F.A. Jenet, G.B. Hobbs, W. Van Straten, R.N. Manchester, M. Bailes, JPW Verbiest, R.T. Edwards, A.W. Hotan, J.M. Sarkissian, and S.M. Ord, "Upper bounds on the low-frequency stochastic gravitational wave background from pulsar timing observations: current limits and future prospects," The Astrophysical Journal **653**, 1571 (2006).

[64] BP Abbott, R. Abbott, F. Acernese, R. Adhikari, P. Ajith, B. Allen, G. Allen, M. Alshourbagy, RS Amin, SB Anderson, *et al.*, "An upper limit on the stochastic gravitational-wave background of cosmological origin," Nature **460**, 990–994 (2009).

[65] T. Akutsu, S. Kawamura, A. Nishizawa, K. Arai, K. Yamamoto, D. Tatsumi, S. Nagano, E. Nishida, T. Chiba, R. Takahashi, *et al.*, "Search for a stochastic background of 100-MHz gravitational waves with laser interferometers," Physical Review Letters **101**, 101101 (2008).

[66] Koji Ishidoshiro, *Search for low-frequency gravitational waves using a superconducting magnetically-levitated torsion antenna*, Ph.D. thesis, The University of Tokyo (2010).

[67] K. Ishidoshiro, M. Ando, A. Takamori, H. Takahashi, K. Okada, N. Matsumoto, W. Kokuyama, N. Kanda, Y. Aso, and K. Tsubono, "Upper Limit on Gravitational Wave Backgrounds at 0.2 Hz with a Torsion-Bar Antenna," Physical Review Letters **106**, 161101 (2011).

[68] A. Shoda, M. Ando, K. Okada, K. Ishidoshiro, W. Kokuyama, Y. Aso, and K. Tsubono, "Search for a Stochastic Gravitational-wave Background with Torsion-bar Antennas," Journal of Physics: Conference Series(to be published).

[69] H.A. Sturges, "The choice of a class interval," Journal of the American Statistical Association **21**, 65–66 (1926).

[70] MP Wand, "Data-based choice of histogram bin width," American Statistician, 59–64(1997).

[71] C. Röver, C. Messenger, and R. Prix, "Bayesian versus frequentist upper limits," Arxiv preprint arXiv:1103.2987(2011).

[72] Wataru Kokuyama, "Lessons learned from SWIM_munu," (2012), preparing, [in Japanese].

[73] P. Ajith, M. Hannam, S. Husa, Y. Chen, B. Brügmann, N. Dorband, D. Müller, F. Ohme, D. Pollney, C. Reisswig, *et al.*, "Inspiral-Merger-Ringdown Waveforms for Black-Hole Binaries with Nonprecessing Spins," Physical Review Letters **106**, 241101 (2011).

[74] Masaki Ando, private communication.

[75] Japan Aerospace Exploration Agency, *SDS-1 Serial Communication Protocal Definition Document*, the second ed. (January 2008), [in Japanese].

Acknowledgment

This work could not be done without a lot of kind supports and advices from many people. I have had the biggest fortune to work in the field of gravitational wave physics at the University of Tokyo with my adviser, Prof. Kimio Tsubono. He supported me about everything at any time in the lab. Prof. Yoichi Aso, an assistant professor in our lab, has been my cooperator at any time. Prof. Masaki Ando, a former assistant professor in our lab, is a proposer of the project. He has given me a lot of kind support and insightful advices. Prof. Takeshi Takashima has given me a lot of support. I could not do my research without his advises.

A number of co-researchers has supported me in this research. Prof. Tadayuki Takahashi, Prof. Kazuhiro Nakazawa, Prof. Motohide Kokubun, Prof. Akito Araya, Prof. Akiteru Takamori, Prof. Sigenori Moriwaki, Prof. Tatsuaki Hashimoto, Prof. Takehiko Ishikawa, Prof. Shujiro Sawai, Prof. Shin-ichiro Sakai, Prof. Tetsuo Yoshimitsu, Prof. Nobutaka Bando, Prof. Hiromitsu Inatomi, Prof. Hiroaki Kobayashi and Mr. Shigehito Shimuzu kindly supported me. Dr. Takayuki Yuasa and Dr. Hirokazu Odaka have given me useful advices. The software module written by them has worked well. I also thank my collaborators, Prof. Shuichi Sato, Dr. Teruaki Enoto, Dr. Keiko Kokeyama and Prof. Tomoaki Toda. I address and thank encouragements from Prof. Shigenori Hiramatsu and Dr. Noriaki Ohmae.

A lot of companies have been involved in the project. YS design Inc., Japan Space Forum, Diamond Air Service, Shimafuji Electric, Mitsubishi Heavy Industry, NEC, NEC Toshiba Space System, Clearpulse, Idea Systems, Meisei Electric, SEC (Systems Engineering Consultants Co., LTD.) and Myu Research Inc. has been my collaborators in enterprise. Dr. Keiichi Hirako, Dr. Yosuke Nakamura, Mr. Kazutaka Kawashima, and other SDS-1 operation members at JAXA has been cooperative at any time. I would like to thank them all.

I thank Prof. Koji Ishidoshiro and Mr. Kakeru Takahashi, who are former lab-mate for me. I also thank my colleagues in our lab, Kenshi Okada, Nobuyuki Matsumoto, Yuta Michimura, Ayaka Shoda, Takafumi Ushiba and Kazunori Shibata, thank you for all. Also, Ms. Michiko Kudoh, Ms. Miki Ueda, Ms. Ami Ito and Ms. Yoko Sasaki has kindly supported my office work.

Finally, I would like to express my gratitude to my parents, who gave me everything and demanded nothing.

謝辞 (Acknowledgment in Japanese)

この論文で述べられている研究を実施できたのは、さまざまな方々のご指導・ご支援があってこそのものです。関わって下さったすべての皆様へ感謝いたします。皆様への謝辞をすべて述べますと、あまりに長くなりすぎて書ききれなくなると思われますので、私がこの研究を通じて個人的にお世話になった皆様への謝辞のみ、ここに記すことにいたします。

東京大学理学系研究科・坪野公夫教授には、指導教員として私が学部生の時から 6 年間以上指導してくださいました。博士論文の提出が遅れる中、先生の励ましと助言なしには進むことができなかったと思います。出張費や研究費などの、実験的研究に必要となる財源についても全面的にバックアップして下さいました。また、研究方法や方向性について暖かく見守りながらも、自分の好きなようにさせていただいた 6 年間でした。

同・麻生洋一助教には、わからないことなどがあった場合にはいつも質問させて頂きました。英語の書き方やプレゼン練習に付き合ってくださるなど、基本的なことまで丁寧に教えていただきました。

国立天文台・安東正樹准教授（元坪野研究室助教）は、SWIM$_{\mu\nu}$計画の発案者であり、すべての点についてお世話になりました。氏のもつ能力のみならず、研究に対する構想力や発展力など、その下にいるだけで大変に学ぶところが多かったと思います。

JAXA 宇宙科学研究所・高島健准教授には、製作・環境試験から運用に至るまですべてのことについて相談し、その都度丁寧に教えてくださいました。トラブルの原因をどこまでも追求し、何としても装置の完成に導く、という執念と体力の重要性についても学ばせていただきました。

同・高橋忠幸教授は、SpaceWire や SWIM 計画のリーダーとして、全体を強力に推進してくださいました。実験全体についてばかりではなく、私のことも気にかけてくださり、励ましていただきました。

東京大学理学系研究科・中澤知洋講師、JAXA 宇宙科学研究所・国分紀秀准教授には、放射線試験や振動試験といった環境試験で協力してくださるなど、様々な面でお世話になりました。運用時にもいろいろなノウハウや経験を教えて下さり、とてもためになりました。

東京大学地震研究所・新谷昌人准教授、同・高森昭光助教、東京大学工学系研究科・森脇成典主任研究員は、実験装置製作の初期段階で変位センサや環境モニタセンサなどの設計を担当されていました。その部分を中心に、電気回路とそのノイズなどのさまざまなことを教

えてくださいました。

JAXA 宇宙科学研究所・橋本樹明教授、同・澤井秀次郎准教授、同・坂井真一郎准教授、同・吉光徹雄准教授、同・稲富裕光准教授、同・坂東信尚助教、同・小林弘明助教、同・清水成人氏をはじめとする無重力落下実験装置 (BOV) グループには、気球からの無重力実験という大変貴重な機会をいただきました。この実験装置製作や三陸での運用のなかで、ものづくりや衛星搭載装置開発の上での考えかたなど多くのことを学び、非常に楽しかったです。

同・石川毅彦教授、(株) ダイアモンドエアサービス・福島玄三氏、同・伊藤正光氏をはじめとする皆様には、相乗りによって航空機による無重力実験をさせていただくという機会をいただきました。この実験で試験マス制御に成功したことが、後の FM 製作・衛星運用に向けての自信と励みになりました。また、横浜国立大学・奥谷猛教授は機上での実験の写真を撮影してくださいました。

JAXA 宇宙科学研究所・湯浅孝行研究員と同・小高裕和研究員には、SpaceCube2 搭載ソフトウェア開発においてさまざまな形でお世話になりました。衛星搭載ソフトウェアを曲がりなりにも完成できたのは、お二人からの適切な助言を頂いたからです。搭載ソフトには、両氏の制作した機能モジュールも組み込まれており、正常に動作しました。

また、論文共著者として、法政大学・佐藤修一准教授、スタンフォード大学・榎戸輝揚研究員、ルイジアナ州立大学・苔山圭以子研究員、JAXA 宇宙科学研究所・戸田知朗准教授にもご支援をいただきました。

坪野研究室特任研究員/KEK・平松成範名誉教授は、重力波の周波数変換について親身に相談に乗ってくださいました。

坪野研究室特任研究員/理化学研究所/東京大学工学系研究科・大前宣昭研究員には、博士論文執筆を励ましていただくとともに、実験についてや研究の方法論についてなど、さまざまな楽しいお話を一緒にさせて頂きました。

装置の衛星搭載後の運用に関しては、JAXA 宇宙実証研究共同センター・平子敬一センター長、中村揚介氏、川島一能氏をはじめとする SDS-1 開発・運用チームの皆様に、あらゆる面でお世話になりました。衛星側へいろいろな無茶な要求を出したときでも、「検出器側がデータを使い尽くしてくれるのは嬉しいことだ」と言って下さったことが、データ解析をすすめる上での励みになりました。

実験装置の設計・製作・試験などを進める上や論文執筆において、多くの企業の方々にもご協力いただきました。(有) ワイエスデザイン、(財) 日本宇宙フォーラム、(株) ダイアモンドエアサービス、(株) シマフジ電機、(株) 三菱重工業、(株)NEC、(株)NTSpace、(株) クリアパルス、(株) イデアシステム、(株) 明星電気、(株) セック、(有) ミューリサーチ、ほか関わって下さったすべての皆様に感謝いたします。特に、NTSpace・檜原弘樹氏、三菱重工業・松田健司氏、セック・松久孝志氏は装置の開発から運用に至るまで、さまざまなご協力をいただきました。トラブル時は深夜でも泊まりでも対応してくださり、また FPGA や組

み込みソフトといった技術面のいろいろなことを親切に教えてくださいました。ありがとうございました。

東北大学助教・石徹白晃治氏（元坪野研究室）には、実験開始時からともに実験や運用で多大なご協力をいただきました。特に、実験装置のデジタルフィルタは氏の製作したFPGAロジックによるものです。検出器のコントロールシステムを氏と議論・実験しながらつくりあげていったことは、とても良い思い出として残っています。

(株) 住友重機械工業・高橋走氏（元坪野研究室）には、5年間同じ研究室でお世話になりました。いつも様々なことを話しながら、研究活動に楽しく取り組めました。SWIM$_{\mu\nu}$においても、気球実験や環境試験に協力してくださいました。研究室だけでなく、夏の学校などでもいろいろと一緒に楽しませていただきました。

坪野研究室D3・岡田健志氏からも、様々な面で刺激を受けました。実験についてを中心に、いろいろなことをよく議論させていただきました。

同D2・松本伸之氏は、研究内容が私とかなり異なる分野ですが、よく楽しい議論をさせて頂きました。研究に対して妥協せず努力を惜しまない姿勢に刺激を受けました。

同D1・正田亜八香氏は、4年生実験から3年間同じ研究室でいろいろとお世話になりました。公私ともにアクティブな姿勢をぜひ見習いたいと思っています。

同D1・道村唯太氏とは実験のネタ探しや議論などで楽しく過ごさせていただきました。優秀な氏に対して、私のほうからも刺激を与えられたならばうれしく思っています。

同M2・牛場崇文氏とは、昼食を食べながらの雑談や実験の話などで楽しく過ごせました。、博士論文執筆のペースを作れたように思います。

同M2・柴田和憲氏とは、研究についてなど様々な議論をさせていただきました。よく深夜まで研究室に残って一緒に作業をしていたのも良い思い出です。

また、坪野研究室秘書・工藤伯子氏、元物理第一事務分室・上田美樹氏、物理第一事務分室・伊藤彩美氏、元物理教務・佐々木陽子氏をはじめとする事務担当の皆様のおかげで、研究に集中することができました。

SWIM$_{\mu\nu}$プロジェクトは、科学研究費補助金・基盤研究 (A) 「新しい宇宙物理実験のための超小型衛星プラットホームの開発研究とその実証」、若手研究 (A) 「超伝導を用いた低周波重力波検出器の開発」、その他東京大学経費、JAXA経費等の支援を受けました。また、著者は2009年度〜2011年度にわたり、日本学術振興会・特別研究員事業による支援を受けました。

最後に、すべての面において私を支えてくれた両親に感謝したいと思います。

平成24年6月

穀山 渉